The Dijet Cross Section at Large Rapidity Intervals at $\sqrt{s} = 1800$ and 630 GeV in $p\bar{p}$ Collisions

Anna Goussiou
SUNY, Stony Brook

DØ Note # 3680

December 8, 1999

Abstract

The inclusive dijet production at large rapidity intervals, $\Delta\eta$, between the two jets in $p\bar{p}$ collisions has been suggested as a place to observe BFKL dynamics, due to the appearance of large logarithms $\ln(\hat{s}/Q^2) \approx \Delta\eta$. We measure the inclusive dijet cross section at $\sqrt{s} = 1800$ and 630 GeV. The ratio of the cross sections at fixed momentum transfers, Q, and longitudinal momentum fractions, x, is compared to theoretical predictions. The data exhibit a strong rise of the dijet cross section with $\Delta\eta$, qualitatively consistent with BFKL evolution. An effective value of the BFKL intercept is extracted from the data.

Contents

1 Motivation

The advent of new DIS data at a previously unexplored kinematic region from the HERA *ep* collider has generated a renewed interest in the Balitsky-Fadin-Kuraev-Lipatov (BFKL) equation [1].

In high energy scattering (at large center-of-mass energy $\sqrt{s}$) and for one-scale processes (e.g., for fixed momentum transfer Q), the radiative corrections to the parton-parton scattering contain large logarithms $\ln(s/Q^2)$. In this case, the $\alpha_s \ln(s/Q^2)$ contributions need to be summed to all orders in α_s. This summation is accomplished by the BFKL equation using a space-like chain of an infinite number of gluon emissions. The gluons are strongly ordered in their longitudinal momentum fractions x_i, $x_n \ll x_{n-1} \ll ... \ll x_1$. However, there is no ordering in the gluon transverse momenta k_{Ti} along the chain, but rather a random walk in k_T. That is, the transverse momentum of a gluon in the chain is close to that of the previous gluon but can be either smaller or larger.

The growth of the gluon momentum distribution in the proton due to the BFKL evolution is predicted to be, roughly:

$$xg(x, Q^2) \sim x^{1-\alpha_{\mathrm{BFKL}}} \tag{1}$$

where the BFKL *intercept* α_{BFKL} in the leading logarithmic approximation (LLA) is given by:

$$\alpha_{\mathrm{BFKL}} - 1 = \frac{\alpha_s(\overline{Q^2}) C_A 4 \ln 2}{\pi}. \tag{2}$$

The calculation of the next-to-leading log (NLL) corrections to the kernel of the BFKL equation was completed recently [2]. These corrections are large and negative, and considerably reduce the size of the growth of the gluon at low x. Several theoretical problems regarding the NLL corrections, however, are still unsolved, e.g., they lead to oscillations of the total cross section; their value depends strongly on the renormalization scheme; they contain only the one-loop runnning of the coupling constant. In addition, next-to-next-to-leading log corrections may also be large. Therefore, it is not really possible to make quantitive theoretical predictions at this point; experimental results, however, can guide the BFKL phenomenology.

In the context of deep inelastic scattering, the large logarithms of s/Q^2 take the form of logarithms of $1/x$, corresponding to the region of small Bjorken x. In this region, the BFKL equation predicts the strong rise of the proton structure function F_2 with decreasing x. However, the conventional DGLAP evolution [3] also gives a satisfactory description of the current HERA F_2 measurements [4]. In addition, it is difficult to extract information about the BFKL equation from F_2 data, due to the intermixing of perturbative and non-perturbative effects in the very low x, low Q^2 region, and to the loss of the BFKL-characteristic diffused k_T dependence. Thus, structure function measurements alone are not sufficient for observing BFKL dynamics. For this reason, alternative quantities have been investigated, where DGLAP evolution is suppressed while BFKL evolution is enhanced, and where the characteristic x and k_T dependences of the BFKL gluon ladder can both be exposed. Hadronic final states provide such observables. In DIS events, forward jet production with jet transverse momentum $k_{Tj} \simeq Q$ and jet longitudinal momentum fraction $x_j \gg x$ has been studied [5]. BFKL predicts a rise in the forward jet cross section with $\log(x_j/x)$ [6]. The HERA results seem to support such a behaviour; a direct comparison of the theory to the data, however, is not yet possible, because the analytic BFKL calculations exist only at the parton level. Alternatively, in high energy hadron-hadron collisions the inclusive dijet production can be studied. For large values of x_j, the large logarithms $\ln(s/Q^2)$ reduce to $\ln(\hat{s}/Q^2)$ (where $\sqrt{\hat{s}}$ is the partonic center-of-mass energy) which are of the order of the (pseudo)rapidity[1] interval $\Delta\eta$ between the two jets. In this case, the BFKL equation predicts a rise in the dijet cross section with $\Delta\eta$, as first discussed by Mueller and Navelet [7].

The experimental observation of the rise of the inclusive dijet cross section with $\Delta\eta$ in $p\bar{p}$ collisions is hampered by the dependence of the cross section on the parton distributions. At large $\Delta\eta$, the behaviour of the cross section is dominated by the $x \to 1$ suppression of the parton distributions. The problem can be overcome by measuring the dijet cross section at two different center-of-mass energies and taking the ratio at the same values of x and Q^2 so as to eliminate the dependence on the parton distributions [8]. Such a measurement will also make feasible an experimental extraction of the BFKL intercept, α_{BFKL}.

[1]Henceforth, the term *rapidity* will be used to refer to pseudorapidity $\eta = -\ln\tan(\theta/2)$.

2 Theoretical Introduction

We consider the dijet production in $p\bar{p}$ collisions:

$$p(\mathrm{p}_1) + \bar{p}(\mathrm{p}_2) \to j_1(k_1) + j_2(k_2) + X \tag{3}$$

where p_1 and p_2 are the 4-momenta of the proton and the antiproton respectively, and k_1 and k_2 are the 4-momenta of the two jets.

The longitudinal momenta of the two jets carry fractions x_1 and x_2 of the proton and antiproton momenta, respectively:

$$k_{1_{//}} = x_1\, \mathrm{p}_{1_{//}} \tag{4}$$
$$k_{2_{//}} = x_2\, \mathrm{p}_{2_{//}} \tag{5}$$

The transverse momenta of the jets are greater than or equal to the momentum transfer, Q, mediated at the hard scattering. We assume:

$$Q^2 = k_{1_\perp} k_{2_\perp} \tag{6}$$

The hadron-hadron center-of-mass energy $\sqrt{s}$ is given by:

$$s = (\mathrm{p}_1 + \mathrm{p}_2)^2, \tag{7}$$

while the parton-parton center-of-mass energy $\sqrt{\hat{s}}$ is given by:

$$\hat{s} = x_1 x_2 s. \tag{8}$$

The total dijet cross section can be factorized as:

$$\sigma(x_1, x_2, Q^2, s) = x_1 P(x_1, Q^2)\, x_2 P(x_2, Q^2)\, \hat{\sigma}(Q^2, s), \tag{9}$$

where $xP(x, Q^2)$ is the sum of the gluon and quark Parton Distribution Functions (PDF's) in the proton and antiproton:

$$xP(x, Q^2) = xg(x, Q^2) + \frac{4}{9} x \sum_f \left(q_f(x, Q^2) + \bar{q}_f(x, Q^2) \right), \tag{10}$$

and $\hat{\sigma}(Q^2, s)$ is the total partonic cross section.

In the *semihard* region, defined as

$$\Lambda_{QCD} \ll Q \ll \sqrt{s}, \tag{11}$$

large logarithms of the form $\ln(s/Q^2)$ appear in the cross section.

If we keep x_1 and x_2 large, the large logarithms factorize into the partonic cross section, with the form $\ln(\hat{s}/Q^2)$. The latter are of the order of the rapidity interval $\Delta\eta = \eta_1 - \eta_2$ between the two jets:

$$\ln(\hat{s}/Q^2) \equiv \ln(x_1 x_2 s/Q^2) \sim \Delta\eta. \tag{12}$$

In Leading Order (LO) perturbation theory, the partonic cross section is given by the Born approximation:

$$\hat{\sigma}_{Born} = \left(\frac{\alpha_s C_A}{\pi}\right)^2 \frac{\pi^3}{2Q^2}. \tag{13}$$

In Higher Order (HO) pertubation theory, the corrections to the partonic cross section can be classified into terms of order $[\alpha_s(Q)\Delta\eta]^p$, called leading logarithmic terms, and terms of the type $[\alpha_s(Q)]^q[\alpha_s(Q)\Delta\eta]^p$, called sub-leading logarithmic terms. In the region where $\alpha_s(Q)\Delta\eta \approx 1$ and $\alpha_s(Q)$ is small, the leading logarithmic terms dominate the cross section. Then, in the Leading Logarithmic Approximation (LLA), the total partonic cross section can be written as:

$$\hat{\sigma} = \left(\frac{\alpha_s C_A}{\pi}\right)^2 \frac{\pi^3}{2Q^2} \left[1 + \sum_{n\geq 1} a_n (\alpha_s \Delta\eta)^n\right]. \tag{14}$$

In order to sum all powers of the leading logarithmic terms $\alpha_s\Delta\eta$, the Balitsky-Fadin-Kuraev-Lipatov (BFKL) theory is used, which utilizes a multigluon amplitude. Both real and virtual gluons are considered. The contribution of real gluons results in the production of additional jets which fill the rapidity interval between the two highest-$|\eta|$ jets (*tagging jets*). The jets are strongly ordered in longitudinal momentum (i.e., in x), whereas there is no strong ordering in transverse momentum (i.e., in Q).

The result of the BFKL summation for the partonic dijet cross section at large rapidity intervals $\Delta\eta$ is given by:

$$\hat{\sigma} = \left(\frac{\alpha_s C_A}{\pi}\right)^2 \frac{\pi^3}{2Q^2} \frac{e^{(\alpha_{\mathrm{BFKL}}-1)\Delta\eta}}{\sqrt{\frac{7}{2}\alpha_s C_A \zeta(3)\Delta\eta}}, \tag{15}$$

where $(\alpha_{\mathrm{BFKL}} - 1)$ is given by eq. (2).

Substituting eq. (15) into eq. (9) we find that the total dijet cross section at large rapidity intervals is proportional to:

$$\sigma(x_1, x_2, Q^2, \Delta\eta) \sim x_1 P(x_1, Q^2)\, x_2 P(x_2, Q^2)\, \frac{1}{Q^2} \frac{e^{(\alpha_{\mathrm{BFKL}}-1)\Delta\eta}}{\sqrt{\alpha_s \Delta\eta}}. \tag{16}$$

Due to the effect of the PDF's, which die off at large values of x, it is not possible to observe the exponential growth of the dijet cross section with the rapidity interval $\Delta\eta$.

However, if we take the ratio of the dijet cross sections at two different center-of-mass energies, $\sqrt{s_A}$ and $\sqrt{s_B}$, while keeping x_1, x_2 and Q^2 fixed, the PDF's will cancel and the ratio of the cross sections reduces to the ratio of the partonic cross sections, which is directly sensitive to BFKL dynamics:

$$R = \frac{\sigma(x_1, x_2, Q^2, s_A)}{\sigma(x_1, x_2, Q^2, s_B)} = \frac{e^{(\alpha_{\mathrm{BFKL}}-1)(\Delta\eta_A - \Delta\eta_B)}}{\sqrt{\Delta\eta_A/\Delta\eta_B}} = \frac{e^{(\alpha_{\mathrm{BFKL}}-1)\ln(s_A/s_B)}}{\sqrt{\Delta\eta_A/\Delta\eta_B}}. \tag{17}$$

Using eq. (17), we can extract an effective value for the BFKL intercept α_{BFKL}.

3 Data Sample

The data used at center-of-mass energy $\sqrt{s} = 1800$ GeV were collected during Run Ic, taken in January 1996, under special low luminosity conditions (LOWLUM runs). The data set at center-of-mass energy $\sqrt{s} = 630$ GeV was collected during the low energy Run Ic, taken in December 1995 (LNR runs).

The trigger used in this analysis is Jet 12B, which required:

- at Level 1: two trigger towers above 2 GeV;
- at Level 2: one jet with E_T above 12 GeV.

The integrated luminosity of trigger Jet 12B in the LOWLUM data was 0.69 nb^{-1}, and in the LNR data 31.82 nb^{-1}.

The data were reconstructed using RECO 12.21. The jet energy scale was determined according to CAFIX 5.2 [9, 10], with a different offset and rapidity-dependent correction for the low energy sample [11].

It should be noted here that additional data exist at $\sqrt{s} = 1800$ GeV, taken with low E_T triggers during Run Ib (QNT runs). However, there are some important differences between the QNT and the LOWLUM/LNR runs. The first

- contain no vertex information reconstructed from tracking;
- were taken with an online requirement for single $p\bar{p}$ interactions, which resulted in a wrong calculation of the integrated luminosity. In addition, this contradicts the fact that no single interaction requirement is applied in this analysis (see section 6.4).
- were taken with a different trigger than the data in the LOWLUM and LNR runs.

On the contrary, the LOWLUM data at $\sqrt{s} = 1800$ GeV were taken under the exact same run conditions as the LNR data at $\sqrt{s} = 630$ GeV, which is important when taking the ratio of the dijet cross section at the two center-of-mass energies. Therefore, we choose not to use the QNT data.

4 Data Selection

During data taking in Run Ic there was no requirement on the Level-0 detector, due to a large number of rapidity gap triggers taken at the same time. Therefore, a good Level-0 fast Z-vertex is required offline.

A vertex cut is applied in order to ensure good jet resolution. Events are selected if their primary Z-vertex lies within 50 cm from the center of the detector [12].

In order to remove cosmic ray background, the ratio of the E_T of the leading jet to the missing E_T of the event ($\not\!\!E_T$) is required to be greater than 1.4 [12].

In order to ensure good jet reconstruction efficiency, jets are selected with a minimum E_T of 20 GeV. A maximum jet rapidity cut of $|\eta| < 3$ is also imposed, due to the large uncertainties in the more forward jet energy scale and resolutions.

In addition, jets are required to satisfy the standard jet quality cuts [12]:

- ElectroMagnetic Fraction: EMFR < 0.9
- Hot Cell Fraction: CELFR < 20
- Coarse Hadronic Fraction: CHFR < 0.4

All events that pass the event selection criteria and have at least two jets that pass the jet selection criteria, are kept in the sample.

5 Event and Jet Corrections

The measured dijet cross sections have to be corrected for inefficiencies of the trigger, the jet reconstruction algorithm, and the data selection procedure. The methods to estimate and the values of the above (in)efficiencies are described in the following.

5.1 Trigger Efficiency

As discussed in paragraph 3, the trigger Jet 12B used in this analysis required two trigger towers (TT) with transverse energy greater than 2 GeV at trigger Level 1, and one jet with transverse energy greater than 12 GeV at trigger Level 2. The immediately less restrictive trigger was Jet 12, which required one TT above 2 GeV at Level 1 and one jet above 12 GeV at Level 2. Therefore, the efficiency of the Jet 12B trigger at Level 1 can be measured in respect to the Level 1 trigger efficiency of Jet 12.

The Level 1 (L1) *single jet* trigger efficiency for Jet 12 is measured using MIN-BIAS data. It is equal to the fraction of jets in events passing the MIN-BIAS trigger that have at least one TT with transverse energy greater than 2 GeV. It is measured as a function of the *uncorrected* (measured) jet E_T^{meas} and jet η:

$$\epsilon_{12}^{L1,j}(E_{Tj}^{meas}, \eta_j) = \frac{\text{number of jets in MIN}-\text{BIAS events with 1 TT above threshold}}{\text{number of jets in MIN}-\text{BIAS events}}. \tag{18}$$

The single jet trigger efficiency for Jet 12 has been measured using MIN-BIAS data during Run Ib [13]. It is equal to:

$$\epsilon_{12}^{L1,j}(E_{Tj}^{meas}, \eta_j) = 1 - e^{-\left(\frac{E_{Tj}^{meas}}{a(\eta_j)}\right)^{b(\eta_j)}}, \tag{19}$$

where the parameters $a(\eta_j)$ and $b(\eta_j)$ are given in Table 1.

L1 Single Jet Trigger Eff. for Jet 12		
η_j	$a(\eta_j)$	$b(\eta_j)$
0.0-0.6	11.215	1.842
0.6-1.6	16.903	1.979
1.6-3.5	12.102	1.686

Table 1: *Parameters for L1 single jet efficiency for trigger Jet 12.*

The L1 *event* trigger efficiency for Jet 12 is then calculated as:

$$\epsilon_{12}^{L1} = 1 - \prod_{j=1}^{Njets} [1 - \epsilon_{12}^{L1,j}(E_{Tj}^{meas}, \eta_j)]. \tag{20}$$

The L1 *event* trigger efficiency for Jet 12B in respect to Jet 12 is measured using Mark-&-Pass (MP) data. It is equal to the fraction of MP events with one TT of E_T

greater than 2 GeV that have two TT of E_T above threshold:

$$\epsilon_{12B}^{L1} = \frac{\text{number of MP events with 2 TT above threshold}}{\text{number of MP events with 1 TT above threshold}}. \tag{21}$$

We use the MP data taken during the Ic $\sqrt{s}$ = 630 GeV run. The L1 event trigger efficiency for Jet 12B, plotted as a function of the *uncorrected* transverse energy of the *leading* jet of the event E_{T1}^{meas}, is shown in Fig. 1. Due to limited statistics, only the global efficiency is measured (i.e., *not* as a function of the leading jet η). The efficiency is parametrized as following:

$$\epsilon_{12B}^{L1} = 1 - e^{-\left(\frac{E_{T1}^{meas}}{a}\right)^{b} + c}. \tag{22}$$

The parameters a, b and c are given in Table 2.

L1 Event Trigger Eff. for Jet 12B		
a	b	c
14.641	2.271	-0.414

Table 2: *Parameters for L1 event efficiency for trigger Jet 12B.*

The Level 2 (L2) *event* trigger efficiency for Jet 12B in respect to L1 is equal to the fraction of MP events with two TT above threshold that have the leading L2 jet $E_T > 12$ GeV:

$$\epsilon_{12B}^{L2} = \frac{\text{number of MP events with 2 TT above threshold and } \mathrm{L2E_T} > 12\mathrm{GeV}}{\text{number of MP events with 2 TT above threshold}}. \tag{23}$$

The L2 event trigger efficiency for Jet 12B, plotted as a function of E_{T1}^{meas}, is shown in Fig. 2. Due to limited statistics, only the global efficiency is measured. The efficiency is parametrized as following:

$$\epsilon_{12B}^{L2} = 1 - e^{-\left(\frac{E_{T1}^{meas}}{a}\right)^{b} + c}. \tag{24}$$

The parameters a, b and c are given in Table 3.

L2 Event Trigger Eff. for Jet 12B		
a	b	c
5.062	1.134	1.724

Table 3: *Parameters for L2 event efficiency for trigger Jet 12B.*

The total *event* trigger efficiency for Jet 12B is then equal to:

$$\epsilon_{12B} = \epsilon_{12}^{L1} \cdot \epsilon_{12B}^{L1} \cdot \epsilon_{12B}^{L2}. \tag{25}$$

It is shown in Fig. 3 as a function of the leading jet measured E_T, for the 1800 and 630 GeV samples. The trigger is 85% efficient for leading jets of 20 GeV measured E_T, 95% for jets of 25 GeV, and becomes fully efficient at 30 GeV.

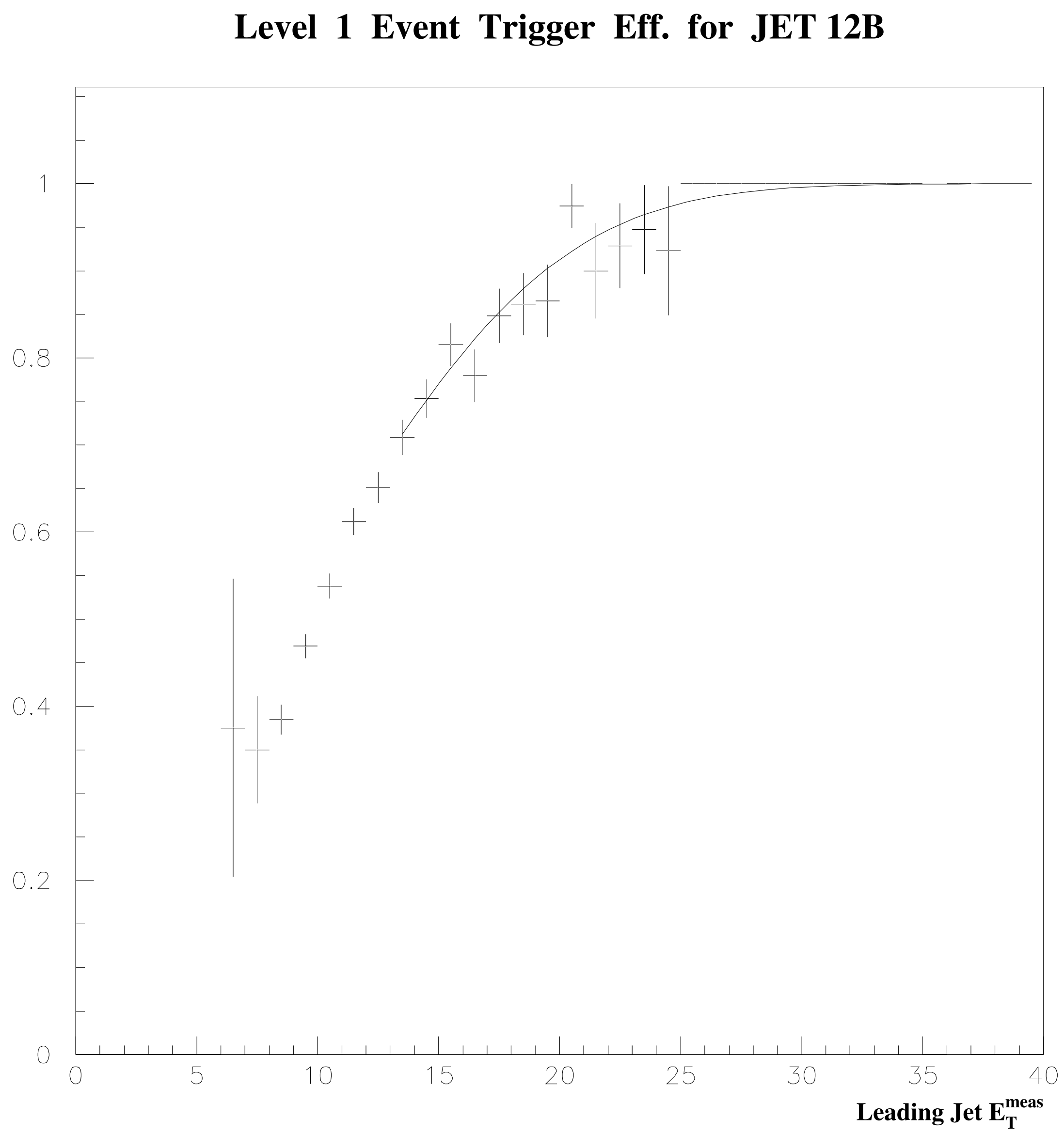

Figure 1: The L1 Event Trigger Efficiency for Jet 12B plotted as a function of the leading jet measured E_T. The error bars represent binomial statistical errors.

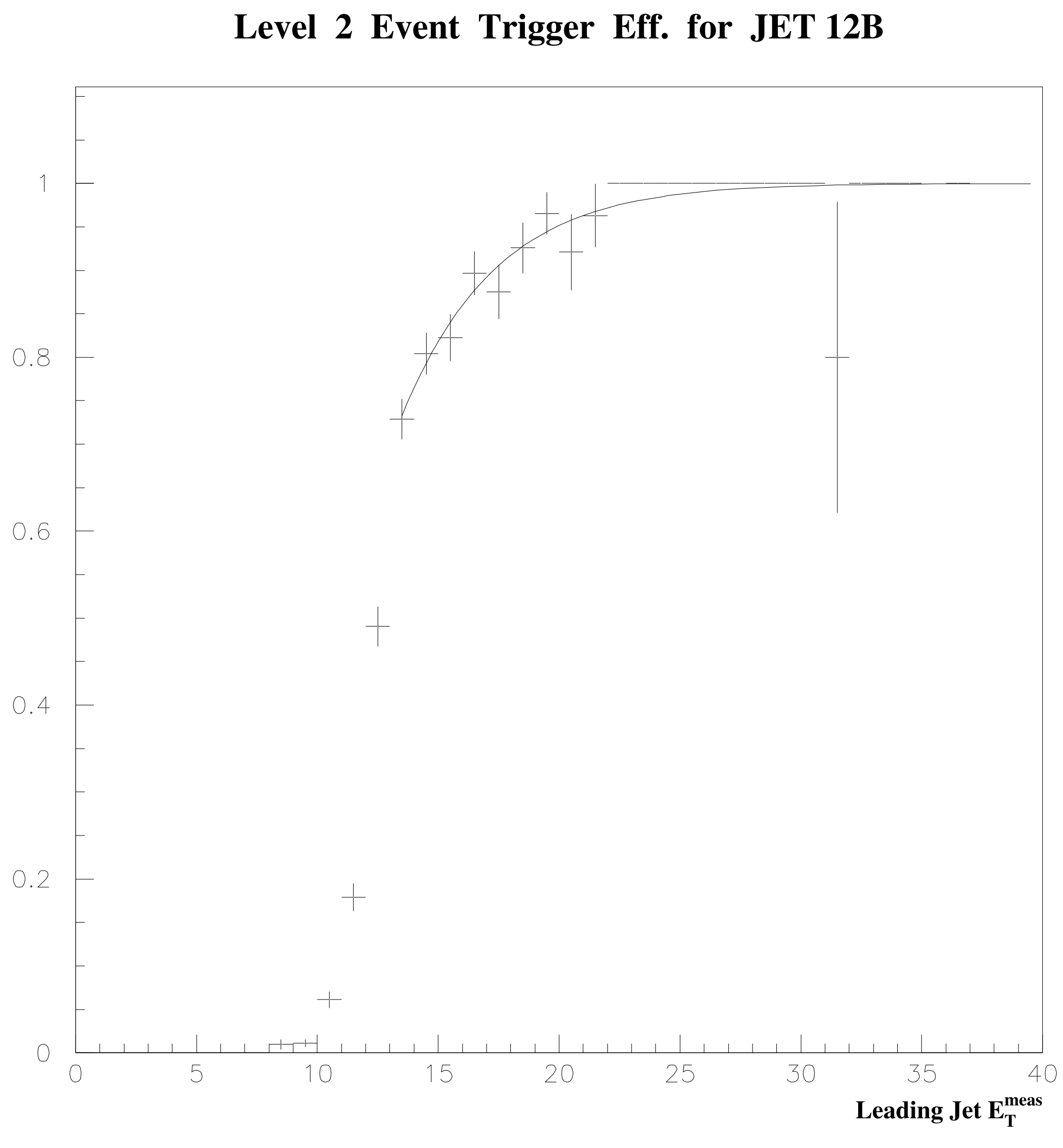

Figure 2: The L2 Event Trigger Efficiency for Jet 12B plotted as a function of the leading jet measured E_T. The error bars represent binomial statistical errors.

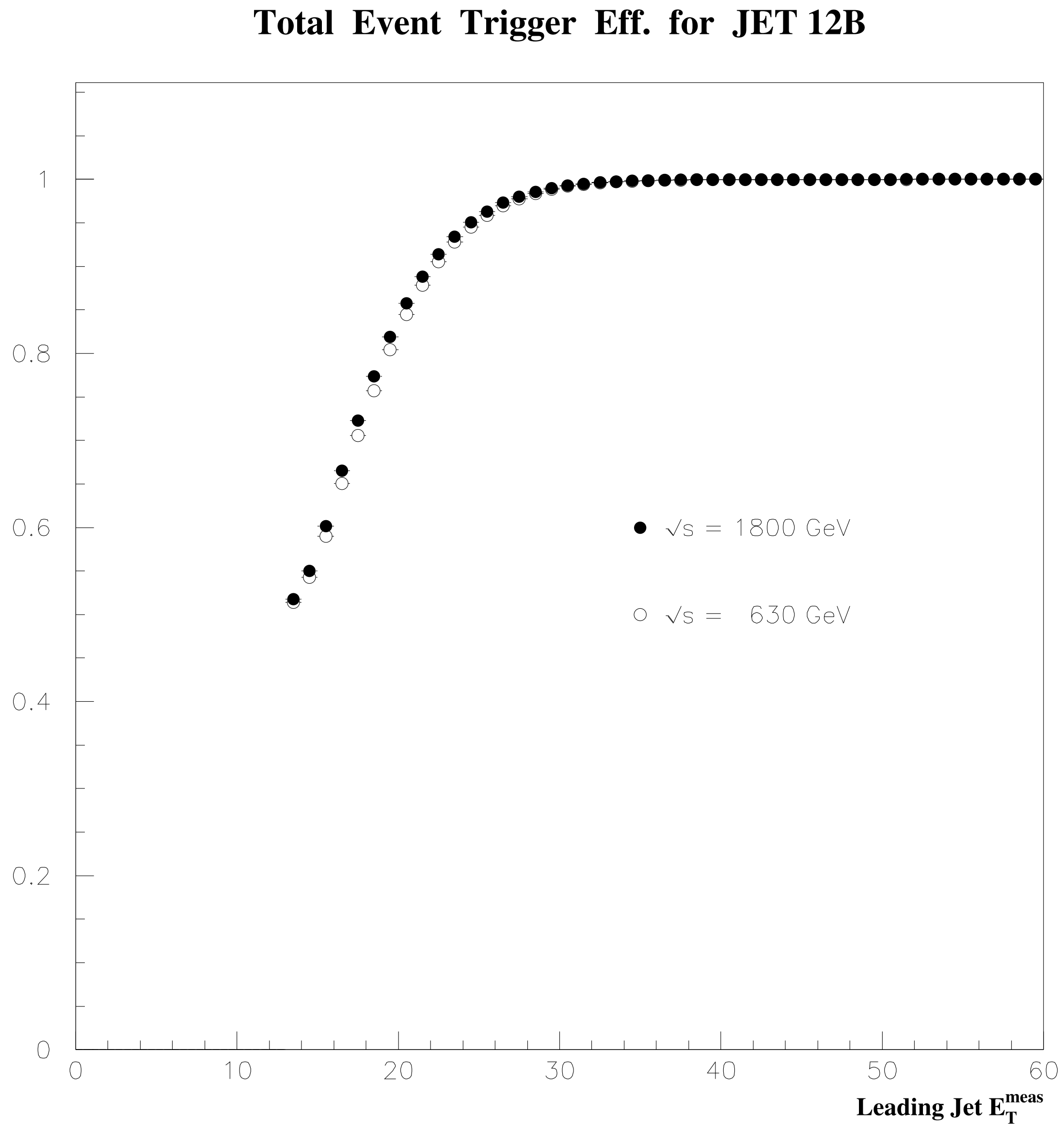

Figure 3: Total Event Trigger Efficiency for Jet 12B plotted as a function of the leading jet measured E_T.

5.2 Jet Reconstruction Efficiency

Jets are reconstructed from energy deposits in the calorimeter using the cone algorithm with a radius of 0.7 in $\eta \times \phi$ space. The algorithm searches for calorimeter towers with transverse energy greater than 1 GeV (*seed* towers), draws a cone around them, and sums the transverse energy of all calorimeter towers in the cone to determine the E_T of the jet [14]. It is evident that the reconstruction of a calorimeter energy deposit into a jet depends strongly on the existence of seed towers above threshold within the energy deposit. Therefore, in order to evaluate the efficiency of the jet reconstruction algorithm, we examine the E_T distributions of the seed towers for jets in various E_T ranges. The algorithm efficiency is then defined as the fraction of the seed towers with transverse energy above threshold [15].

In this analysis, we are mainly interested in the efficiency of the reconstruction algorithm for jets with E_T around 20 GeV. However, since the samples have been selected with triggers that already required one jet with E_T above 12 GeV, the reconstruction efficiency will be biased towards higher values. In order to avoid this trigger bias, we use the efficiency measured in photon-jet samples, requiring a photon of E_T greater than 6 or 14 GeV [16]. The measured jet E_T is required to be at least equal to the photon E_T in order to avoid radiative jets. The results are shown in Fig. 4. The jet reconstruction efficiency is plotted versus the *corrected* (using CAFIX 5.1) jet E_T for the three detector regions. It is parametrized with the following function:

$$\epsilon^{j}_{reco}(E_{Tj}, \eta_j) = a(\eta_j) \cdot \tanh\{b(\eta_j) \cdot [E_{Tj} + c(\eta_j)]\}, \tag{26}$$

where the parameters $a(\eta_j)$, $b(\eta_j)$ and $c(\eta_j)$ are given in Table 4.
The algorithm is fully efficient for jets with $E_T > 20$ GeV.

Single Jet Reco Eff.			
η_j	$a(\eta_j)$	$b(\eta_j)$	$c(\eta_j)$
0.0-0.8	1.000	0.179	-2.450
0.8-1.6	1.002	0.172	-1.275
1.6-3.5	0.998	0.332	-9.887

Table 4: *Parameters for single jet reconstruction efficiency.*

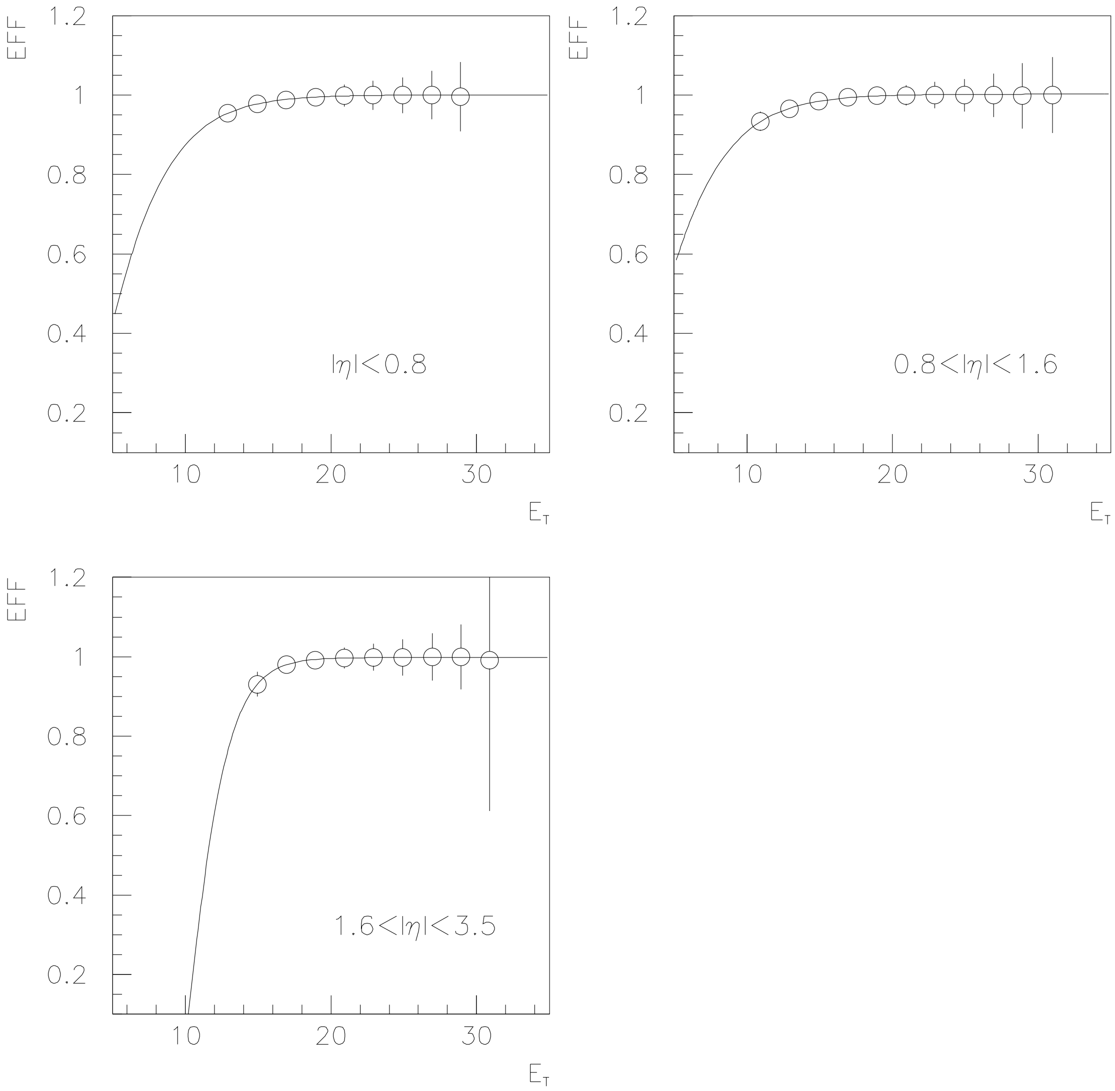

Figure 4: Jet Reconstruction Efficiency. The error bars represent the (binomial) statistical and systematic errors added in quadrature.

5.3 Event and Jet Cuts Efficiency

Performing an event and jet selection is necessary in order to remove background and correct for detector imperfections. However, signal events (jets) are also removed by the selection procedure. Therefore, the measured cross section has to be corrected for selection inefficiencies.

The efficiency of a selection criterion is defined as:

$$\epsilon = \frac{\text{number of events (jets) surviving the cut}}{\textit{true} \text{ total number of events (jets)}}. \tag{27}$$

The *true* distributions for the cut variables can only be estimated approximately. The methods to estimate them, as well as to calculate the cut efficiencies and their uncertainties, are described in reference [12]. Following these methods, the cut efficiencies have been calculated for the specific data samples of this analysis.

The vertex cut efficiency is given in Tables 5 and 6 for the 1800 and 630 GeV data, respectively.

Vertex Cut Eff. at $\sqrt{s} = 1800$ GeV
ϵ_{vertex}
$93.17 \pm 0.04(stat.) \pm 0.85(syst.)$ %

Table 5: *Vertex cut efficiency for the* $\sqrt{s} = 1800$ *GeV data.*

Vertex Cut Eff. at $\sqrt{s} = 630$ GeV
ϵ_{vertex}
$85.51 \pm 0.03(stat.) \pm 0.45(syst.)$ %

Table 6: *Vertex cut efficiency for the* $\sqrt{s} = 630$ *GeV data.*

The $\not{E}_T$ cut event efficiency is measured as a function of the corrected (using CAFIX 5.1) transverse energy and rapidity of the *leading* jet of the event, E_{T1} and η_1. The $\not{E}_T$ cut efficiency plots are shown in Figures 5 and 6 for the 1800 and 630 GeV data, respectively. The efficiency is parametrized with the following function:

$$\epsilon^j_{\not{E}_T}(E_{T1}, \eta_1) = a(\eta_1) \cdot \tanh\{b(\eta_1) \cdot [E_{T1} + c(\eta_1)]\}. \tag{28}$$

The parameters $a(\eta_1)$, $b(\eta_1)$ and $c(\eta_1)$ are given in Tables 7 and 8 for the 1800 and 630 GeV data, respectively.

$\not\!\!E_T$ Cut Eff. at $\sqrt{s} = 1800$ GeV			
η_j	$a(\eta_j)$	$b(\eta_j)$	$c(\eta_j)$
0.0-0.8	0.998	0.077	12.412
0.8-1.6	0.998	0.089	5.888
1.6-3.5	0.999	0.161	-3.560

Table 7: *Parameters for the event* $\not\!\!E_T$ *cut efficiency for the* $\sqrt{s} = 1800$ *GeV data.*

$\not\!\!E_T$ Cut Eff. at $\sqrt{s} = 630$ GeV			
η_j	$a(\eta_j)$	$b(\eta_j)$	$c(\eta_j)$
0.0-0.8	0.994	0.056	31.998
0.8-1.6	0.993	0.099	6.754
1.6-3.5	0.996	0.081	18.056

Table 8: *Parameters for the event* $\not\!\!E_T$ *cut efficiency for the* $\sqrt{s} = 630$ *GeV data.*

The jet cuts efficiency is measured as a function of the corrected (using CAFIX 5.1) jet E_{Tj} and η_j. The jet cuts efficiency plots are shown in Figures 7 and 8 for the 1800 and 630 GeV data, respectively. The efficiency is parametrized with a straight line:

$$\epsilon^j_{jcut}(E_{Tj}, \eta_j) = a(\eta_j) + b(\eta_j) \cdot E_{Tj}. \tag{29}$$

The parameters $a(\eta_j)$, $b(\eta_j)$ and $c(\eta_j)$ are given in Tables 9 and 10 for the 1800 and 630 GeV data, respectively.

Single Jet Cut Eff. at $\sqrt{s} = 1800$ GeV		
η_j	$a(\eta_j)$	$b(\eta_j)$
0.0-0.8	0.987	-0.00011
0.8-1.6	0.983	-0.00012
1.6-3.5	0.969	-0.00017

Table 9: *Parameters for the single jet cut efficiency for the* $\sqrt{s} = 1800$ *GeV data.*

Single Jet Cut Eff. at $\sqrt{s} = 630$ GeV		
η_j	$a(\eta_j)$	$b(\eta_j)$
0.0-0.8	0.980	-0.00025
0.8-1.6	0.974	-0.00024
1.6-3.5	0.938	-0.00010

Table 10: *Parameters for the single jet cut efficiency for the* $\sqrt{s} = 630$ *GeV data.*

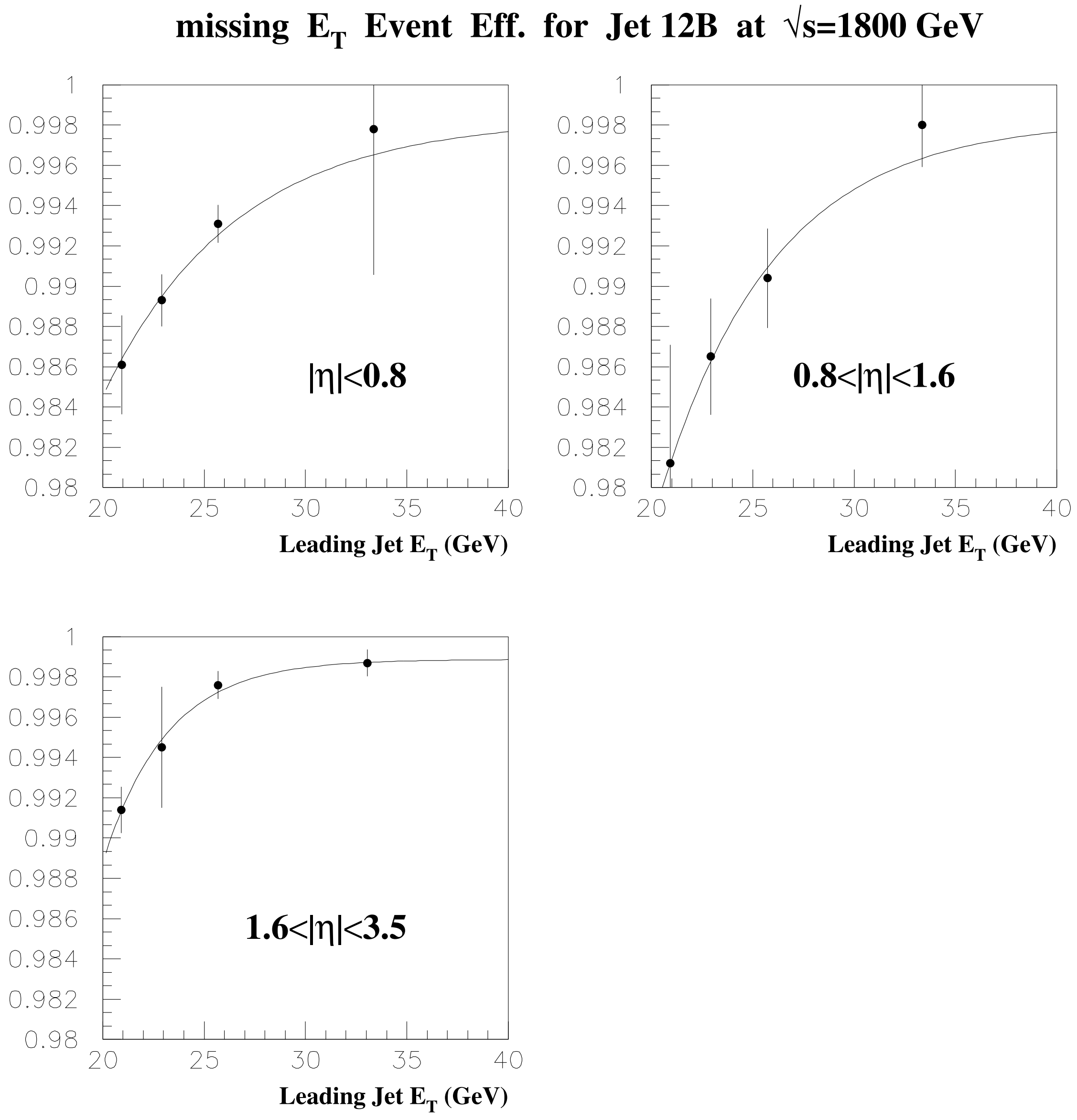

Figure 5: Missing E_T Cut Efficiency for the $\sqrt{s} = 1800$ GeV data. The error bars represent the (binomial) statistical and systematic errors added in quadrature.

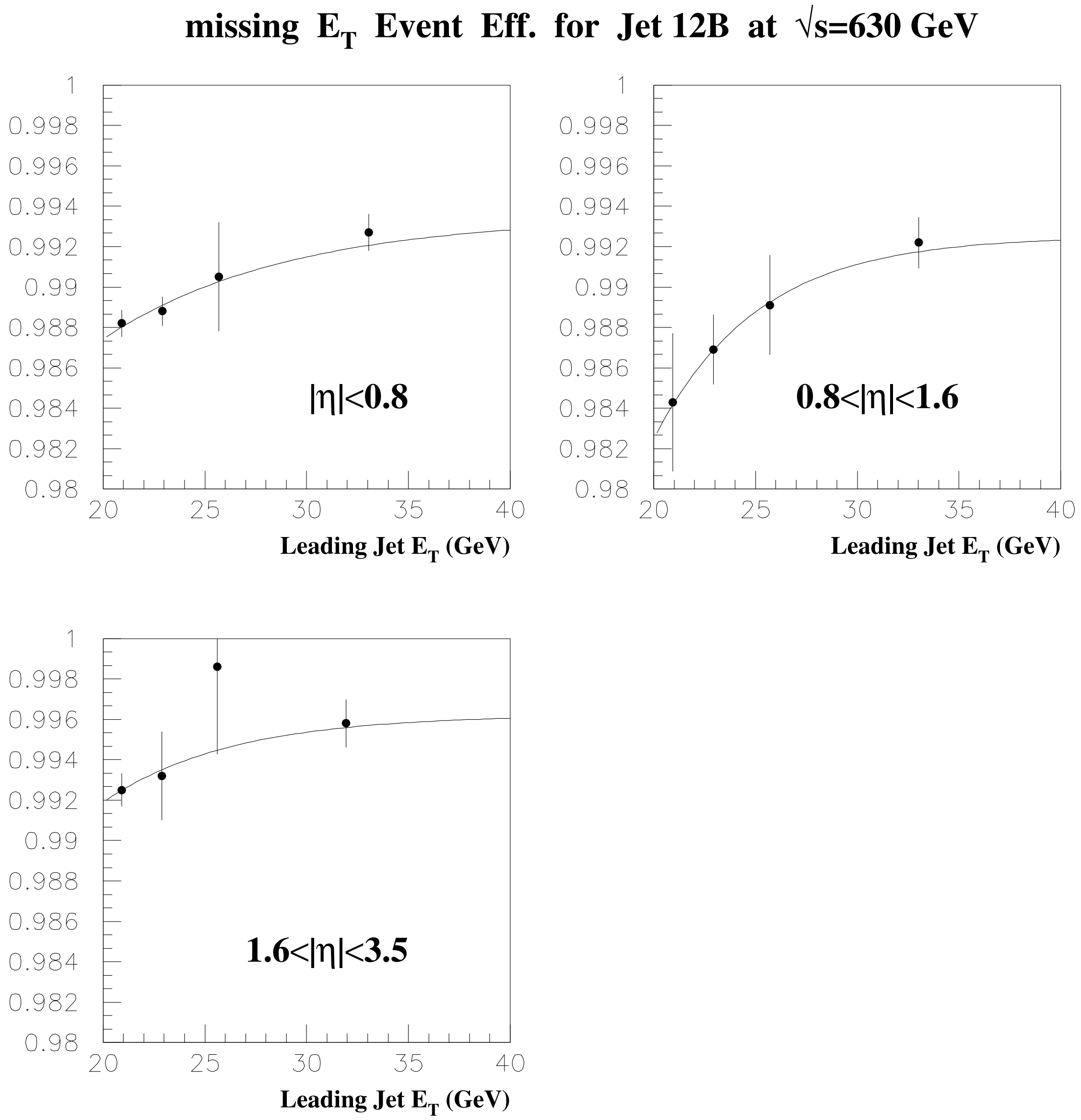

Figure 6: Missing E_T Cut Efficiency for the $\sqrt{s} = 630$ GeV data. The error bars represent the (binomial) statistical and systematic errors added in quadrature.

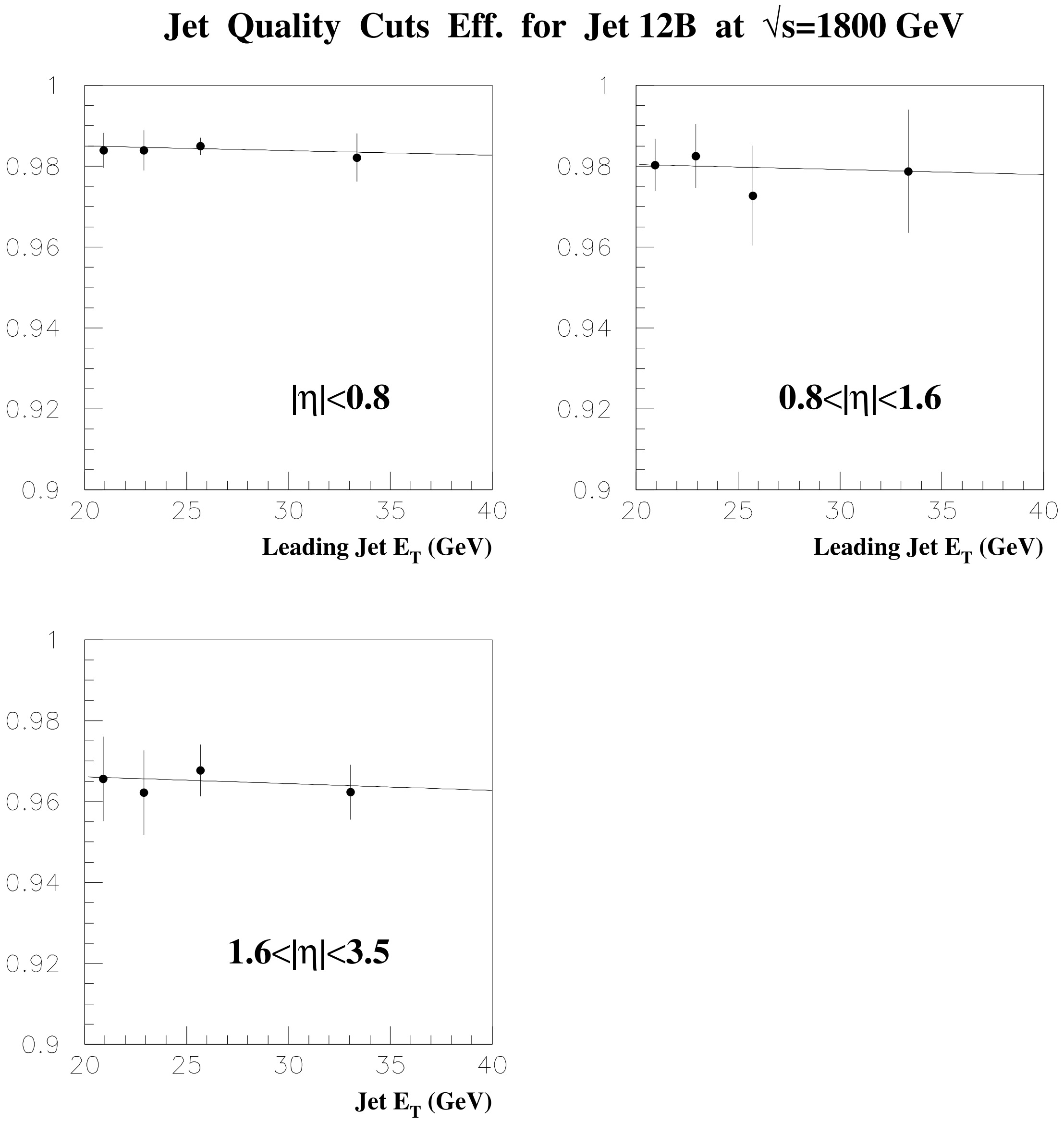

Figure 7: Jet Cuts Efficiency for the $\sqrt{s} = 1800$ GeV data. The error bars represent the (binomial) statistical and systematic errors added in quadrature.

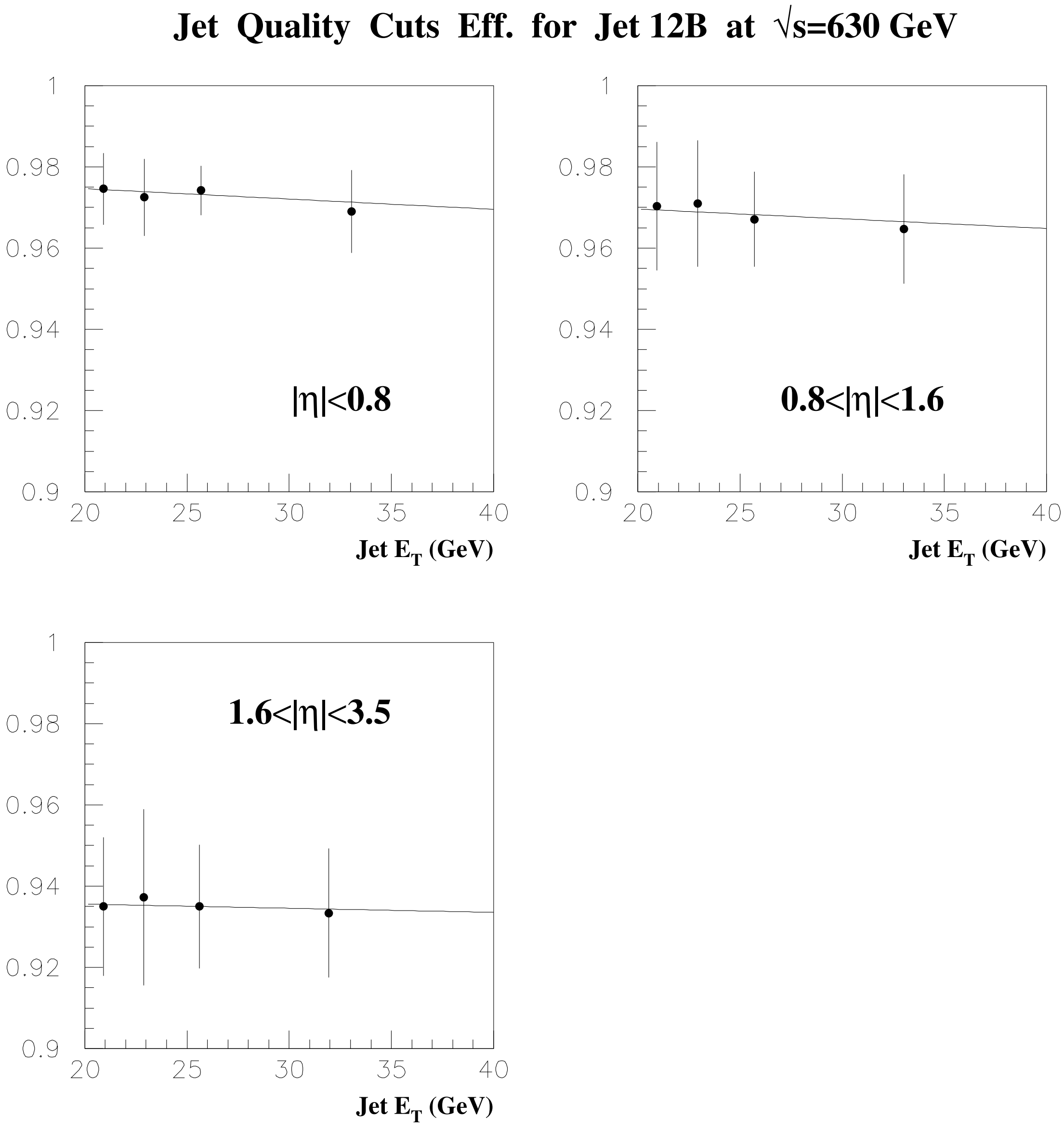

Figure 8: Jet Cuts Efficiency for the $\sqrt{s} = 630$ GeV data. The error bars represent the (binomial) statistical and systematic errors added in quadrature.

5.4 Rapidity Bias

The rapidity of the jets reconstructed in the DØ calorimeters, η_{cal}, is slightly biased towards more central values compared to the rapidity of the jet that entered the calorimeter (i.e., at the particle level), η_{par} [17]. An additional bias is caused from the jet reconstruction algorithm: jets reconstructed with the DØ algorithm [18] are slightly biased towards more forward rapidities compared to jets reconstructed with the Snowmass algorithm [19]. The two effects, studied in Monte Carlo, can be seen in Fig. 9. In this figure, 'RECO η-BIAS' refers to $\eta_{cal}^{DØ} - \eta_{par}^{DØ}$, whereas 'ALGORITHM η-BIAS' refers to $\eta_{par}^{DØ} - \eta_{par}^{Snowmass}$. The total η-bias, defined as $\eta_{cal}^{DØ} - \eta_{par}^{Snowmass}$, is shown in Fig. 10 for jets of $20 < E_T < 40$ GeV. The bias is fitted as a function of absolute rapidity with a 2nd–degree polynomial and applied as a correction to the measured jet rapidities.

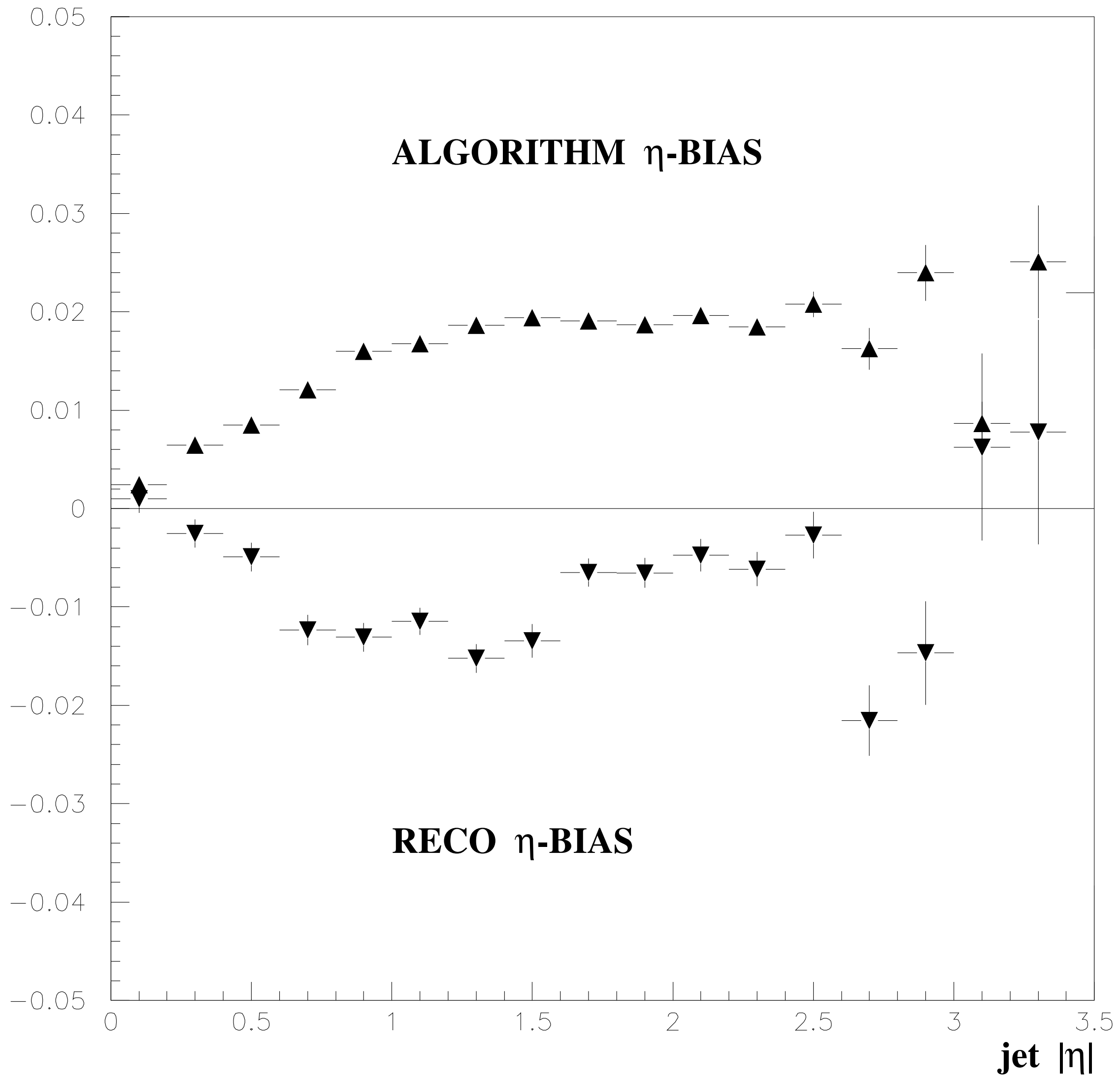

Figure 9: The algorithm η-bias, defined as $\eta_{par}^{DØ} - \eta_{par}^{Snowmass}$, and the reconstruction η-bias, defined as $\eta_{cal}^{DØ} - \eta_{par}^{DØ}$, for jets of $20 < E_T < 40$ GeV.

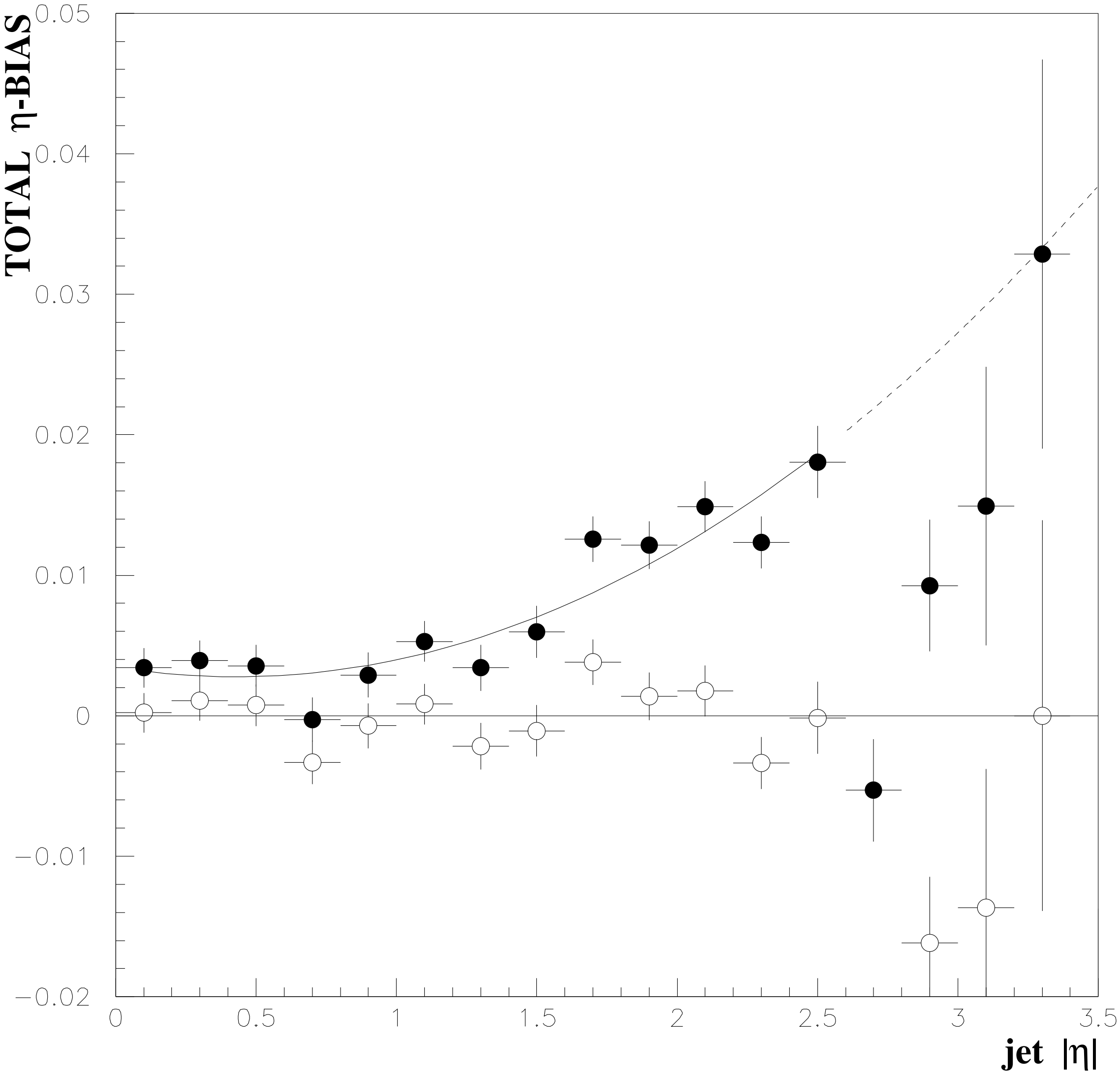

Figure 10: The total η-bias, defined as $\eta_{cal}^{D\O} - \eta_{par}^{Snowmass}$, for jets of $20 < E_T < 40$ GeV (solid circles). The same quantity is also shown after the η-bias correction has been applied (open circles).

6 Dijet Cross Section

6.1 Final Sample

After the event and jet selection is performed (see section 4), the jets of an event are ordered according to pseudorapidity η. The pseudorapidity of the most forward jet will henceforth be denoted by η_1, and that of the most backward jet by η_2. Similarly, the transverse energy of the most forward jet will henceforth be denoted by E_{T_1}, and that of the most backward jet by E_{T_2}.

The rapidity boost is defined as the mean rapidity of the most forward and most backward jet:

$$\bar{\eta} = (\eta_1 + \eta_2)/2 \tag{30}$$

The rapidity boost parametrizes the collective motion of the parton subprocess in the hadron reference frame. The distributions of $\bar{\eta}$ for the 1800 and 630 GeV samples are shown in Fig. 11.

The rapidity interval between the most forward and most backward jet is:

$$\Delta\eta = \eta_1 - \eta_2 \tag{31}$$

The distributions of $\Delta\eta$ for the 1800 and 630 GeV samples are shown in Fig. 12. We require a minimum rapidity interval between the two jets:

$$\Delta\eta > 2. \tag{32}$$

The E_{T_1} and E_{T_2} distributions for the 1800 and 630 GeV final samples (i.e., after the $\Delta\eta$ cut) are shown in Fig. 13. The η_1 and η_2 distributions for the 1800 and 630 GeV final samples are shown in Fig. 14. The jet multiplicities for the two samples are shown in Fig. 15.

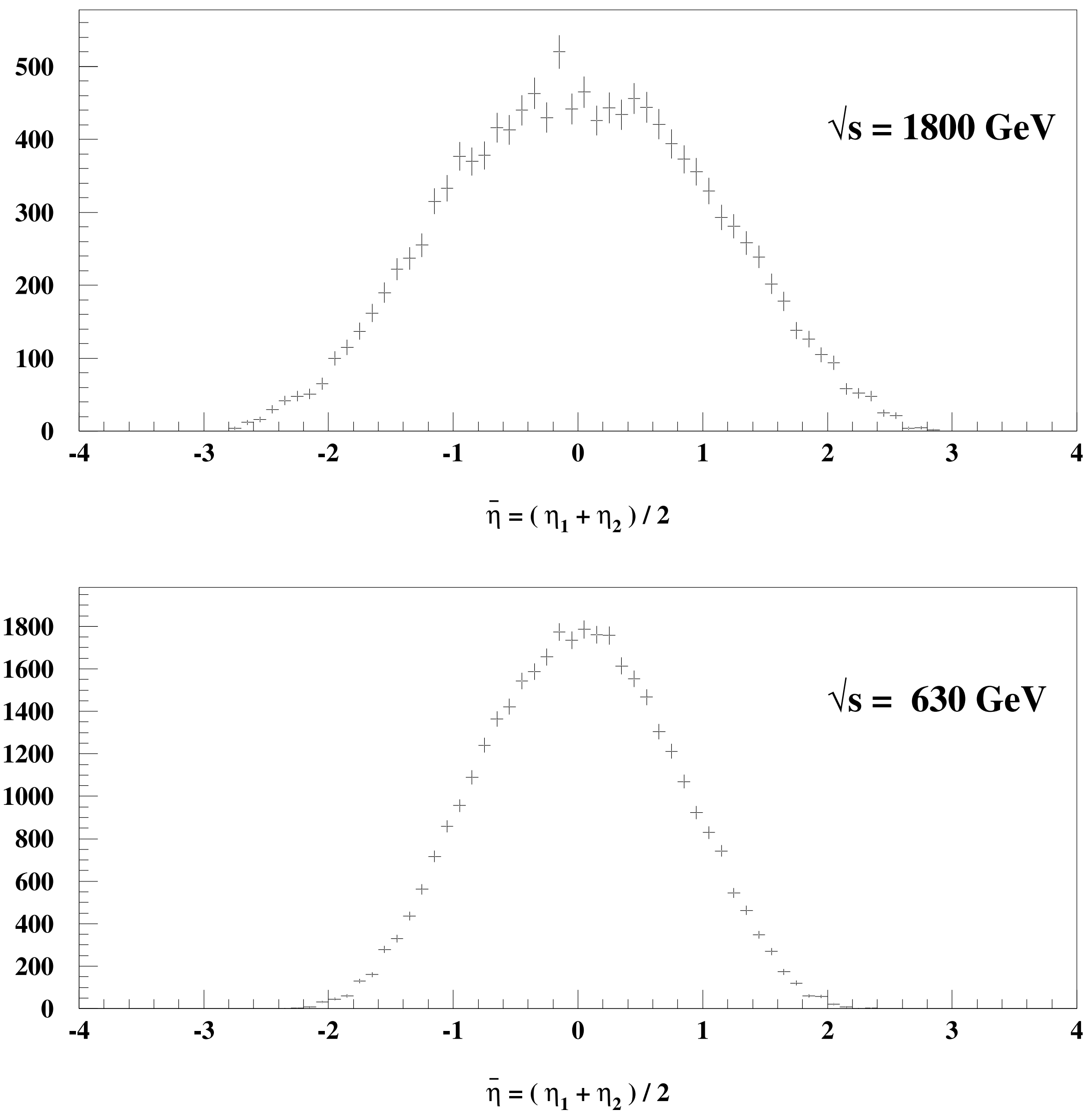

Figure 11: The rapidity boost distributions for the $\sqrt{s} = 1800$ and 630 GeV samples.

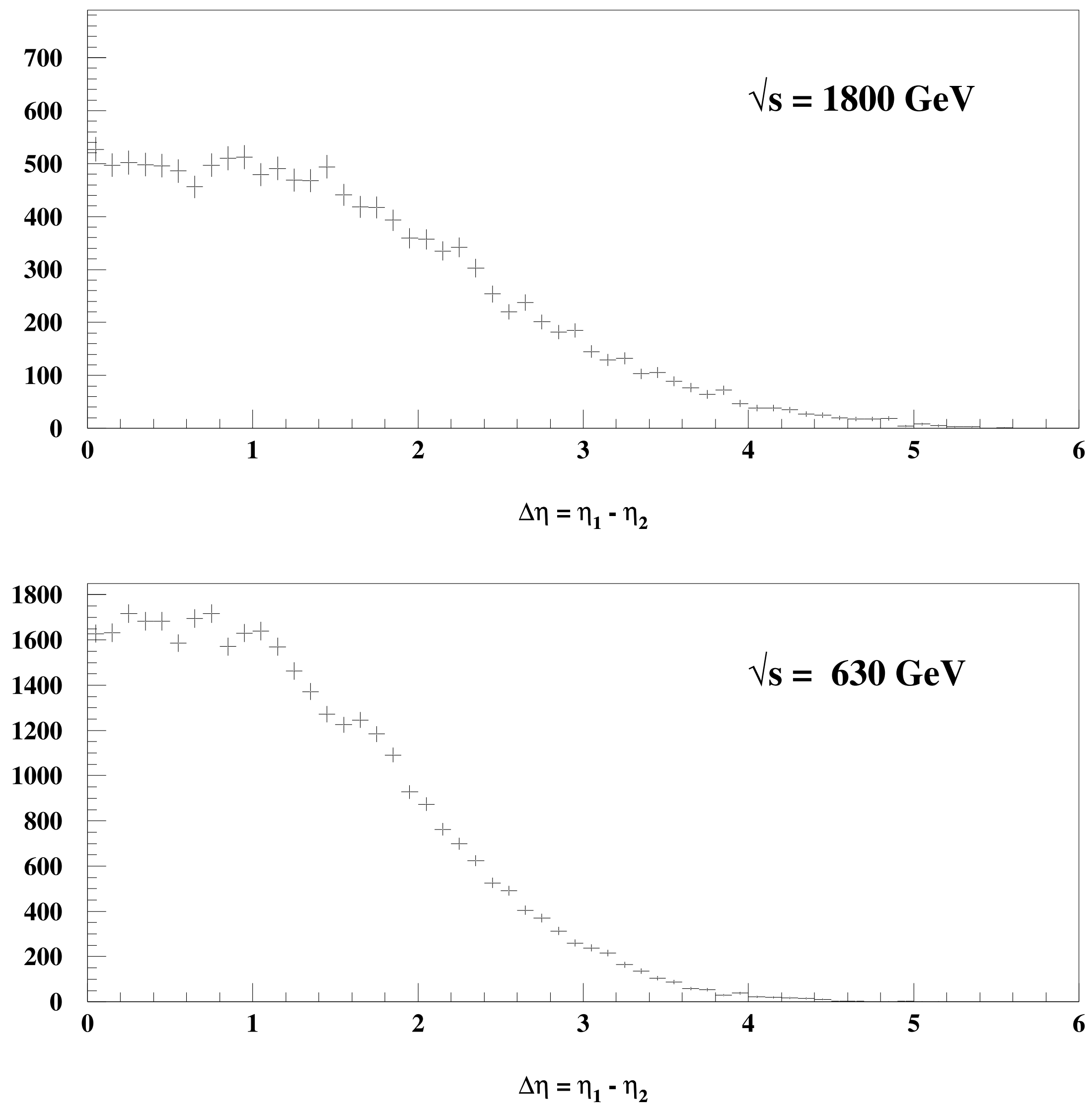

Figure 12: The rapidity interval $\Delta\eta$ between the most forward and most backward jet for the $\sqrt{s} = 1800$ and 630 GeV samples.

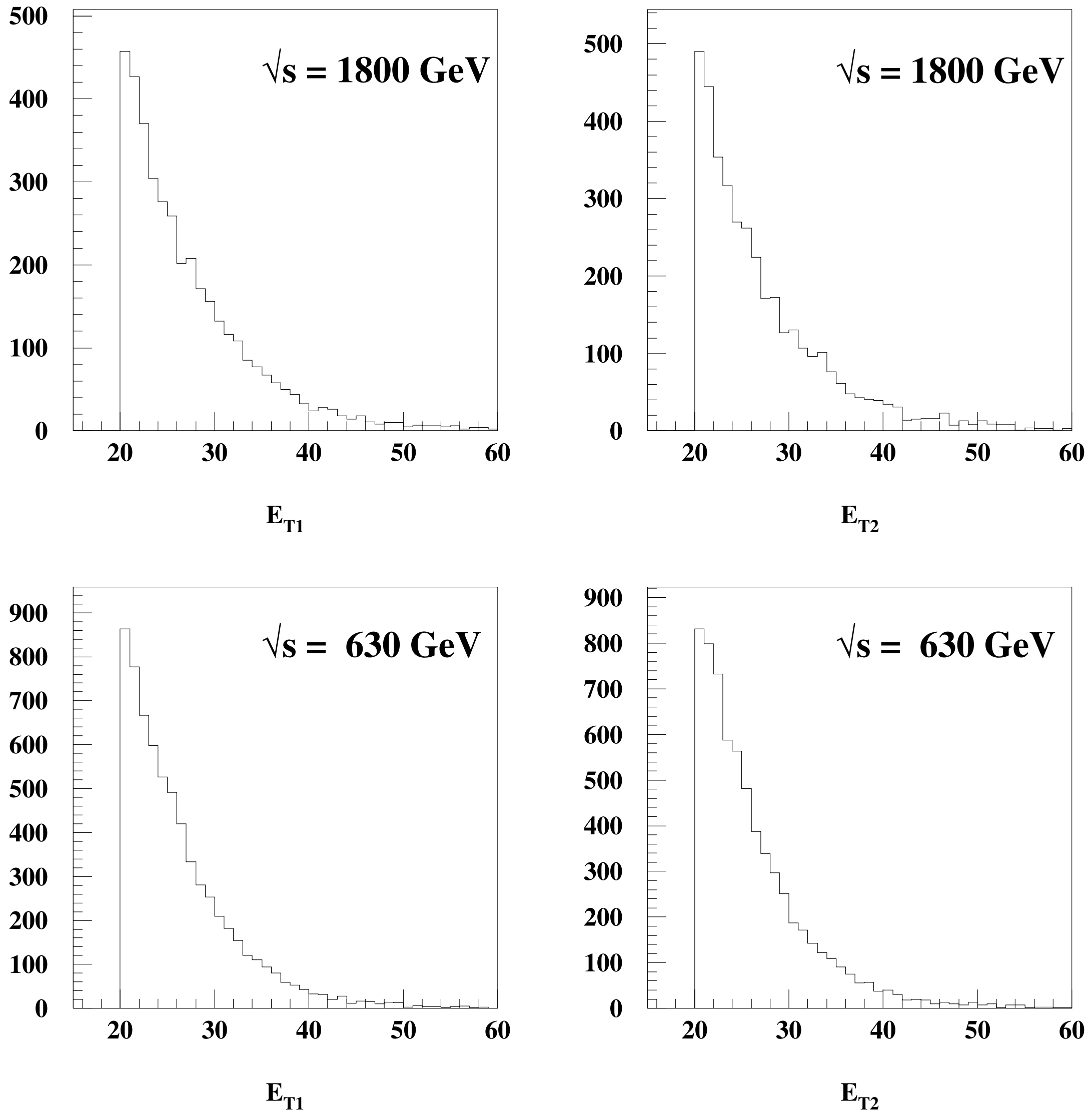

Figure 13: Transverse energy distributions for the most forward (E_{T_1}) and most backward (E_{T_2}) jet for the $\sqrt{s} = 1800$ and 630 GeV samples.

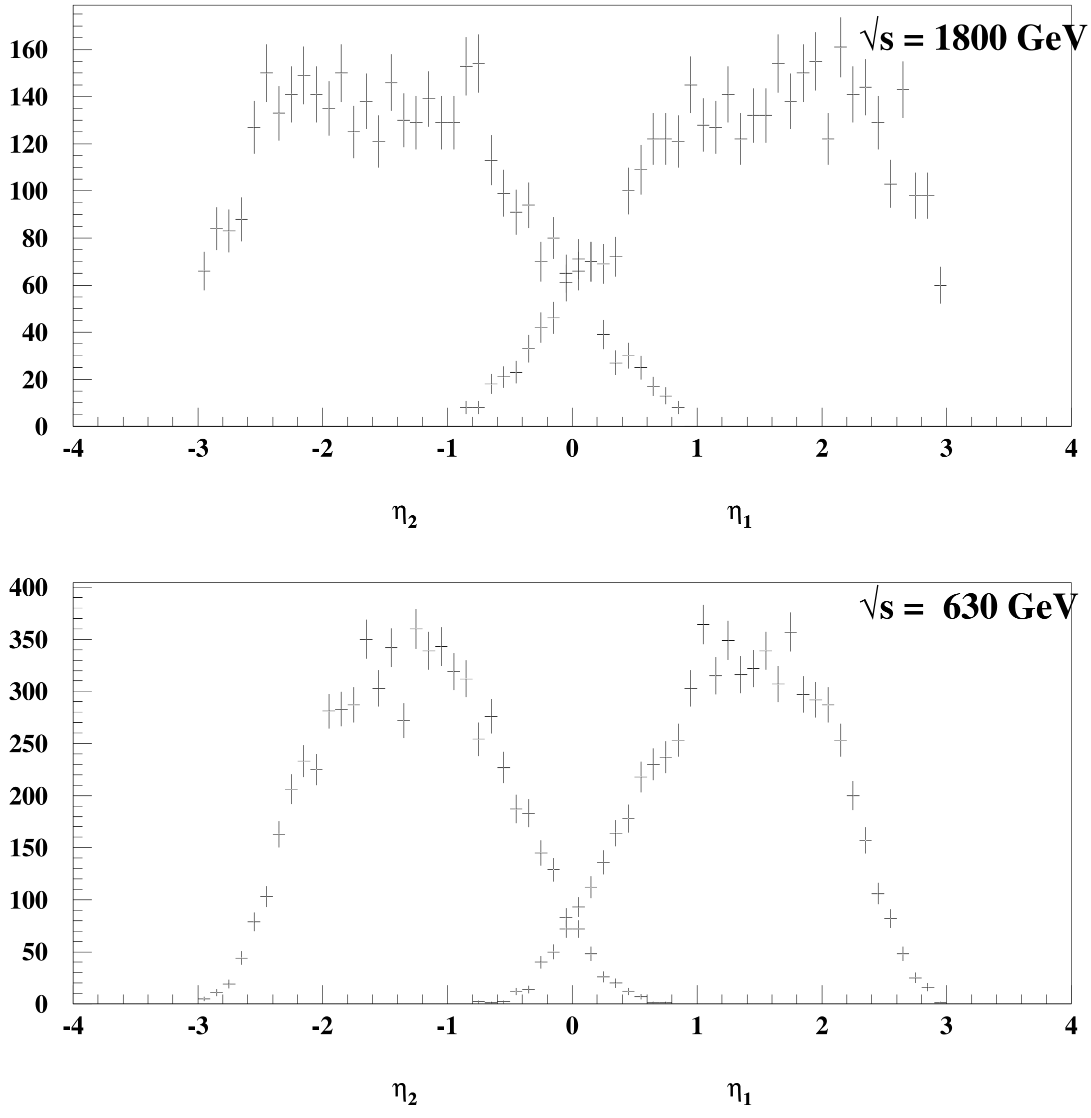

Figure 14: Rapidity distributions for the most forward (η_1) and most backward (η_2) jet for the $\sqrt{s} = 1800$ and 630 GeV samples.

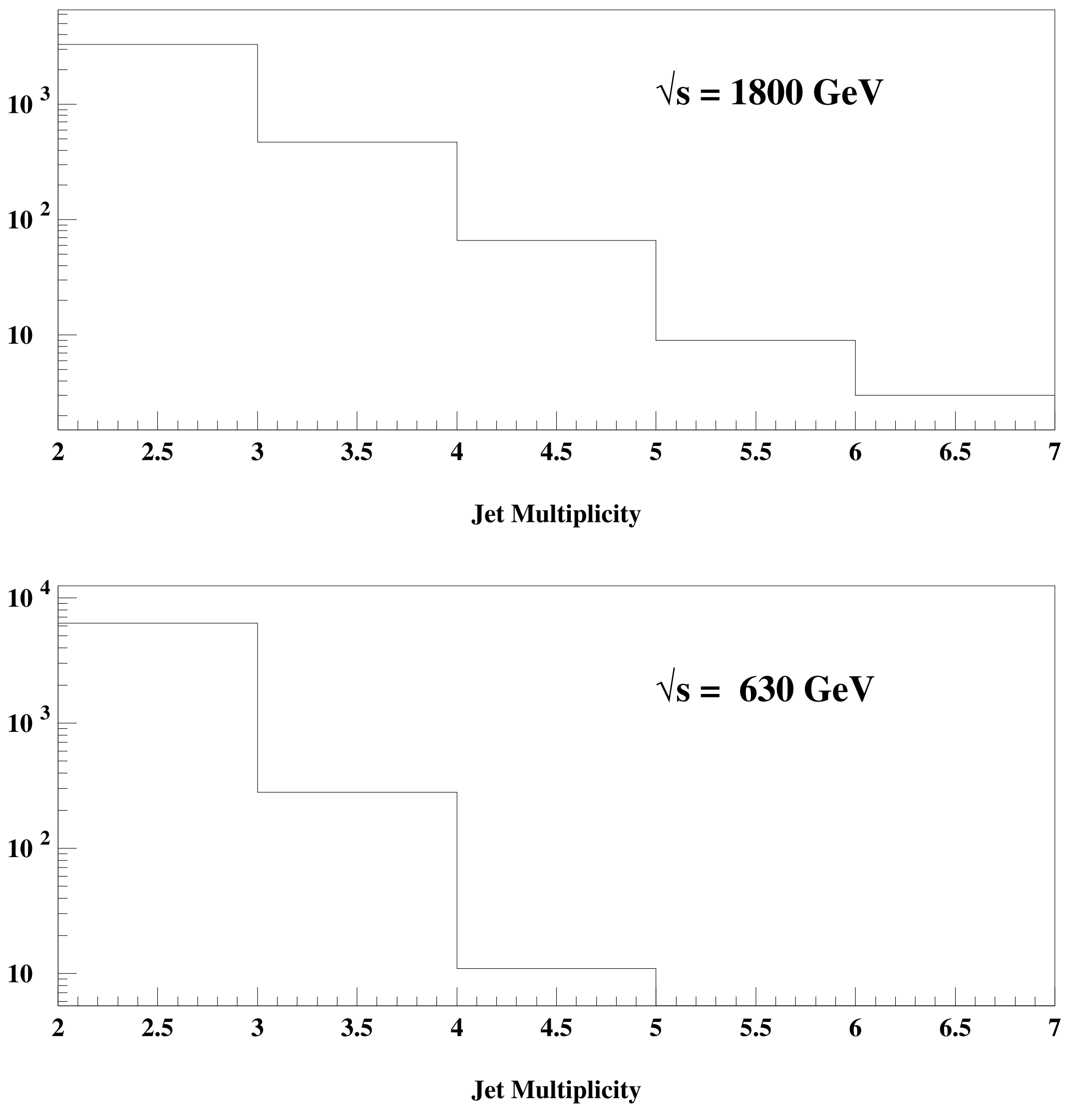

Figure 15: Jet multiplicities for the $\sqrt{s} = 1800$ and 630 GeV samples.

6.2 Reconstruction of Kinematics and Choice of (x_1, x_2, Q^2) Bins

At the lowest order (Born level) hard scattering, two partonic jets are produced back to back. At this level, the parton momentum fractions x_1 and x_2 are given by:

$$x_1 = \frac{2E_{T_1}}{\sqrt{s}} e^{\bar{\eta}} \cosh(\Delta\eta/2) = \frac{E_{T_1}}{\sqrt{s}} (e^{\eta_1} + e^{\eta_2}) \tag{33}$$

$$x_2 = \frac{2E_{T_2}}{\sqrt{s}} e^{-\bar{\eta}} \cosh(\Delta\eta/2) = \frac{E_{T_2}}{\sqrt{s}} (e^{-\eta_1} + e^{-\eta_2}) \tag{34}$$

The above equations give the exact kinematics for dijet production (i.e., no assumption made about the size of the rapidity interval $\Delta\eta$).

The x_1 and x_2 distributions for the 1800 and 630 GeV samples are shown in Fig. 16.

The momentum transfer Q is of the order of the transverse momenta of the jets. We choose:

$$Q^2 = E_{T_1} E_{T_2}, \tag{35}$$

so that, at the large $\Delta\eta$ limit:

$$\ln(\hat{s}/Q^2) \equiv \ln(x_1 x_2 s/Q^2) \simeq \Delta\eta. \tag{36}$$

The Q^2 distributions for the 1800 and 630 GeV samples are shown in Fig. 17.

Due to limited statistics, only one bin in Q^2 is used:

$$400 < Q^2 < 1000 \text{ GeV}^2. \tag{37}$$

The binning in x_1 and x_2 is given in Table 11.

i,j	$x_{1,2}$ range
1	0.02 – 0.06
2	0.06 – 0.10
3	0.10 – 0.14
4	0.14 – 0.18
5	0.18 – 0.22
6	0.22 – 0.26
7	0.26 – 0.30
8	0.30 – 0.60

Table 11: *Definition of the x_1 and x_2 bins.*

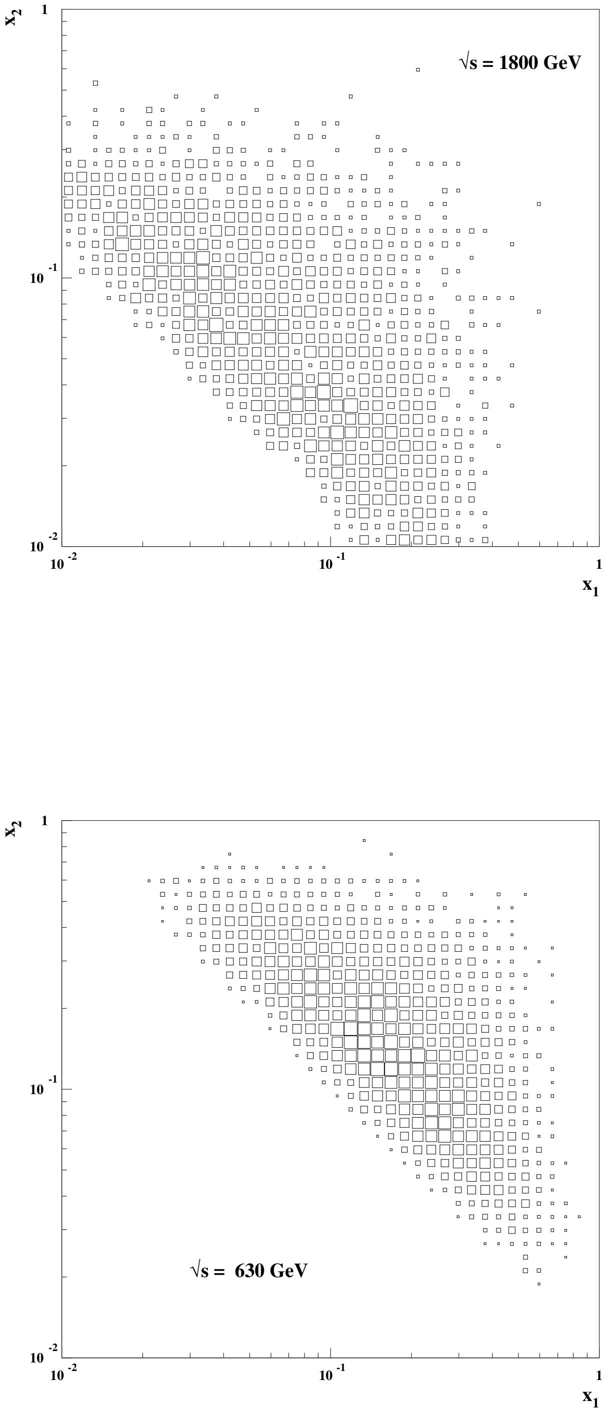

Figure 16: x_1 and x_2 distributions for the $\sqrt{s} = 1800$ and 630 GeV samples.

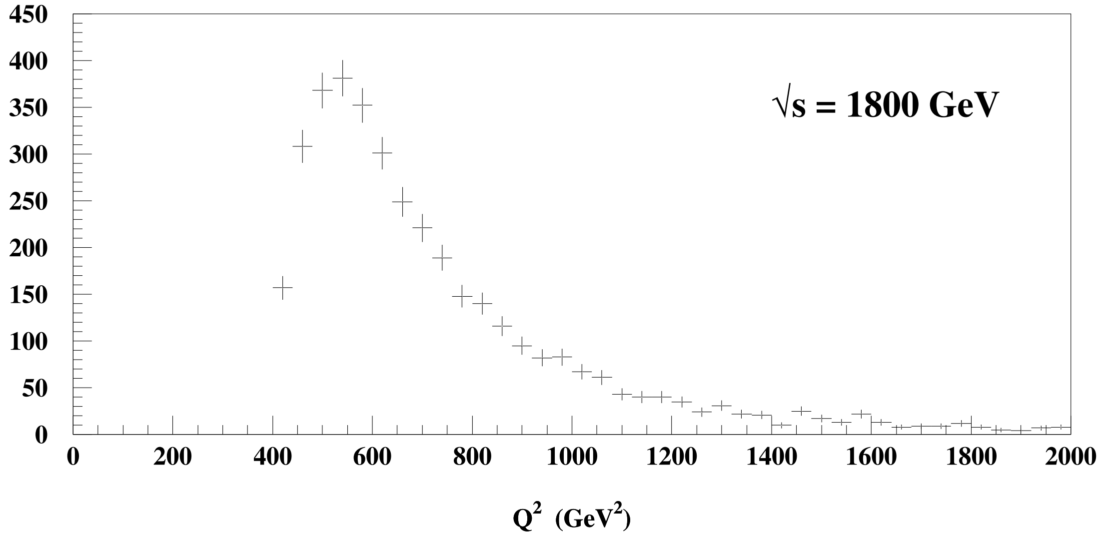

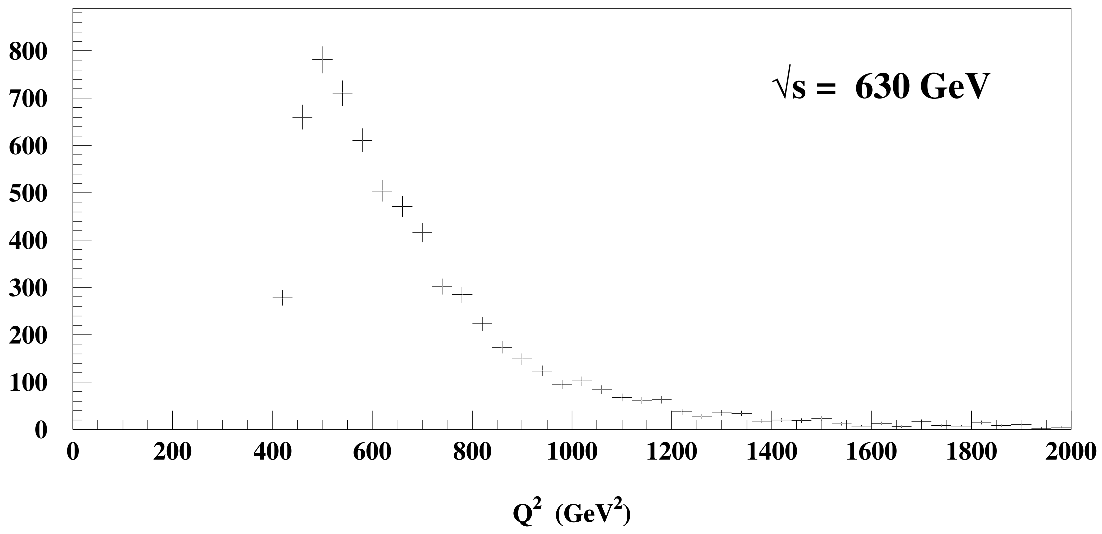

Figure 17: Q^2 distributions for the $\sqrt{s} = 1800$ and 630 GeV samples.

6.3 Measurement of the Dijet Cross Section at 1800 and 630 GeV

The number of data events in each (x_1,x_2,Q^2) bin must be corrected for trigger, jet reconstruction and selection inefficiencies. The total event efficiency is:

$$\epsilon_{tot} = \epsilon_{trig} \cdot \epsilon_{reco} \cdot \epsilon_{sele} \, , \tag{38}$$

where the selection efficiency ϵ_{sele} is given by the product of the vertex, missing E_T, and jet quality cuts efficiencies:

$$\epsilon_{sele} = \epsilon_{vtx} \cdot \epsilon_{\not{E}_T} \cdot \epsilon_{jqc} \, . \tag{39}$$

The inverse of the total efficiency is used as an event weight in measuring the number of events in each bin, $N^{meas}(x_1, x_2, Q^2)$. The measured cross section in the bin is then obtained using the total integrated luminosity of the sample:

$$\sigma^{meas}(x_1, x_2, Q^2) = \frac{N^{meas}(x_1, x_2, Q^2)}{L}. \tag{40}$$

6.4 Multiple Interactions

Multiple $p\bar{p}$ interactions occur primarily at high luminosities. The luminosity profiles for the two samples are shown in Fig. 18. The histograms include events selected with trigger Jet 12B and having a good slow-z vertex. The instantaneous luminosity of the $\sqrt{s} = 1800$ GeV sample is so low that no serious contamination of multiple interactions is expected. In order to evaluate the effect of possible multiple interactions to the $\sqrt{s} = 630$ GeV cross section, we divide the 630 GeV sample in two parts, having instantaneous luminosity above or below 0.2E^{30} particles/cm^2/s. For each part, we measure a cross section in (x_1, x_2, Q^2) bins normalized to the total number of events in the subsample. The study is performed using uncorrected jet transverse energies, in order to isolate any possible luminosity effects from the effects of the jet energy scale correction. Given the limited statistics of the subsamples, the logarithm of the ratio of the two cross sections is taken in each bin, in order to make the results symmetric under the interchange of the subsamples. The error on the high(low)-luminosity cross section in each bin is taken equal to the error on the expected cross section in the bin. The best estimate for the expected cross section consists of the mean of the high- and low-luminosity cross sections in each bin:

$$\sigma_{expect} = \frac{1}{2}(\sigma_{HighL} + \sigma_{LowL}). \tag{41}$$

The error on the expected cross section in each bin is then:

$$\Delta\sigma_{expect} = \frac{1}{2}\sqrt{(\Delta\sigma_{HighL})^2 + (\Delta\sigma_{LowL})^2}, \tag{42}$$

and the error on the logarithm of the ratio of the two cross sections is given by:

$$\Delta(\ln\frac{\sigma_{HighL}}{\sigma_{LowL}}) = \Delta\sigma_{expect}\sqrt{\frac{1}{\sigma^2_{HighL}} + \frac{1}{\sigma^2_{LowL}}}. \tag{43}$$

The results are shown in Fig. 19. We see that the luminosity cut does not affect the cross section, within statistical errors. In order to quantify the comparison, a χ^2 is calculated for the deviation of the logarithm of the ratio from zero. It is found equal to $\chi^2/d.o.f. = 1.21$. Therefore, neither a luminosity cut, nor any other selection procedure designed to remove multiple interactions, is applied in the final samples.

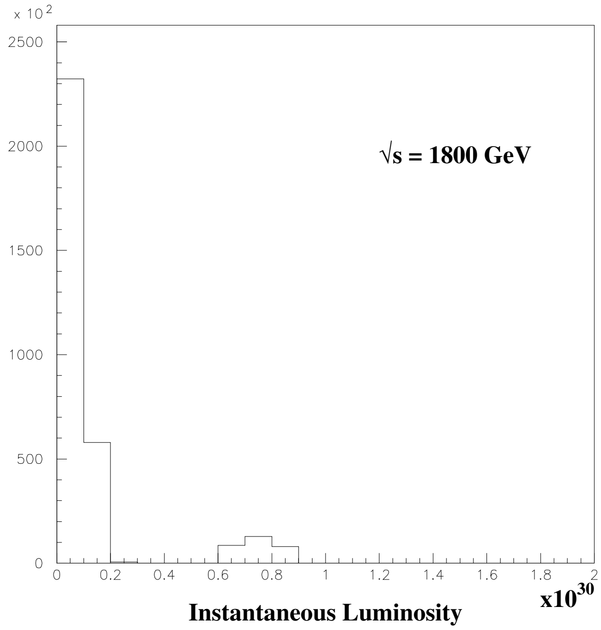

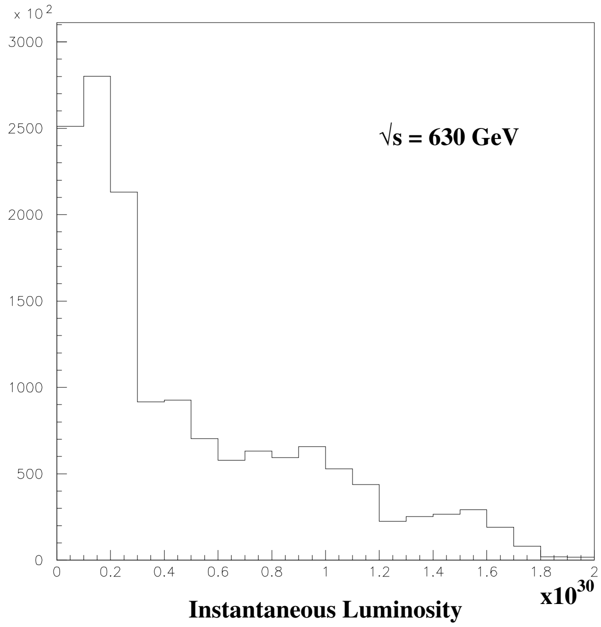

Figure 18: Instantaneous Luminosity distributions for the $\sqrt{s} = 1800$ and 630 GeV samples.

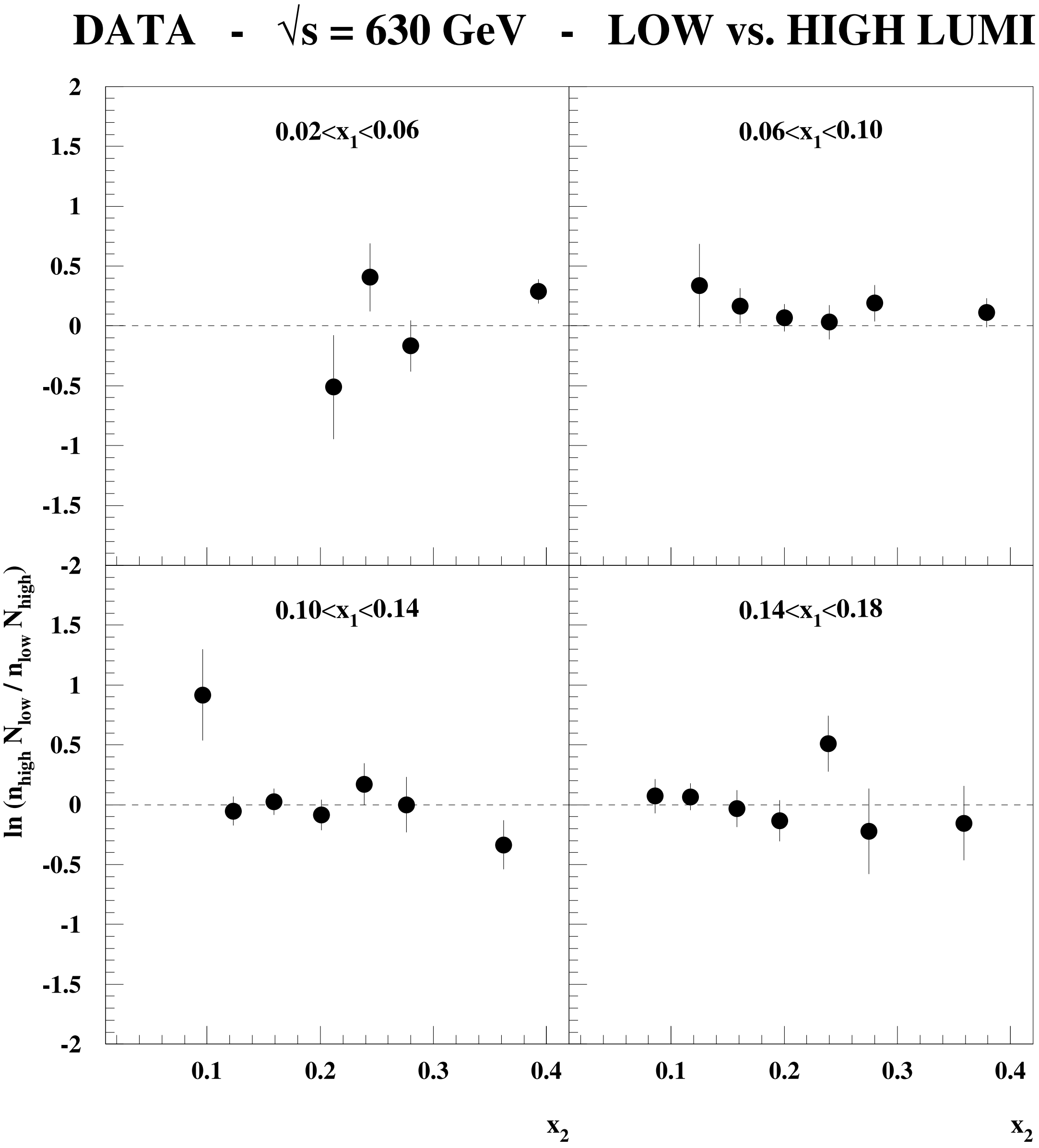

Figure 19: Comparison of the 630 GeV cross section for high and low instantaneous luminosity.

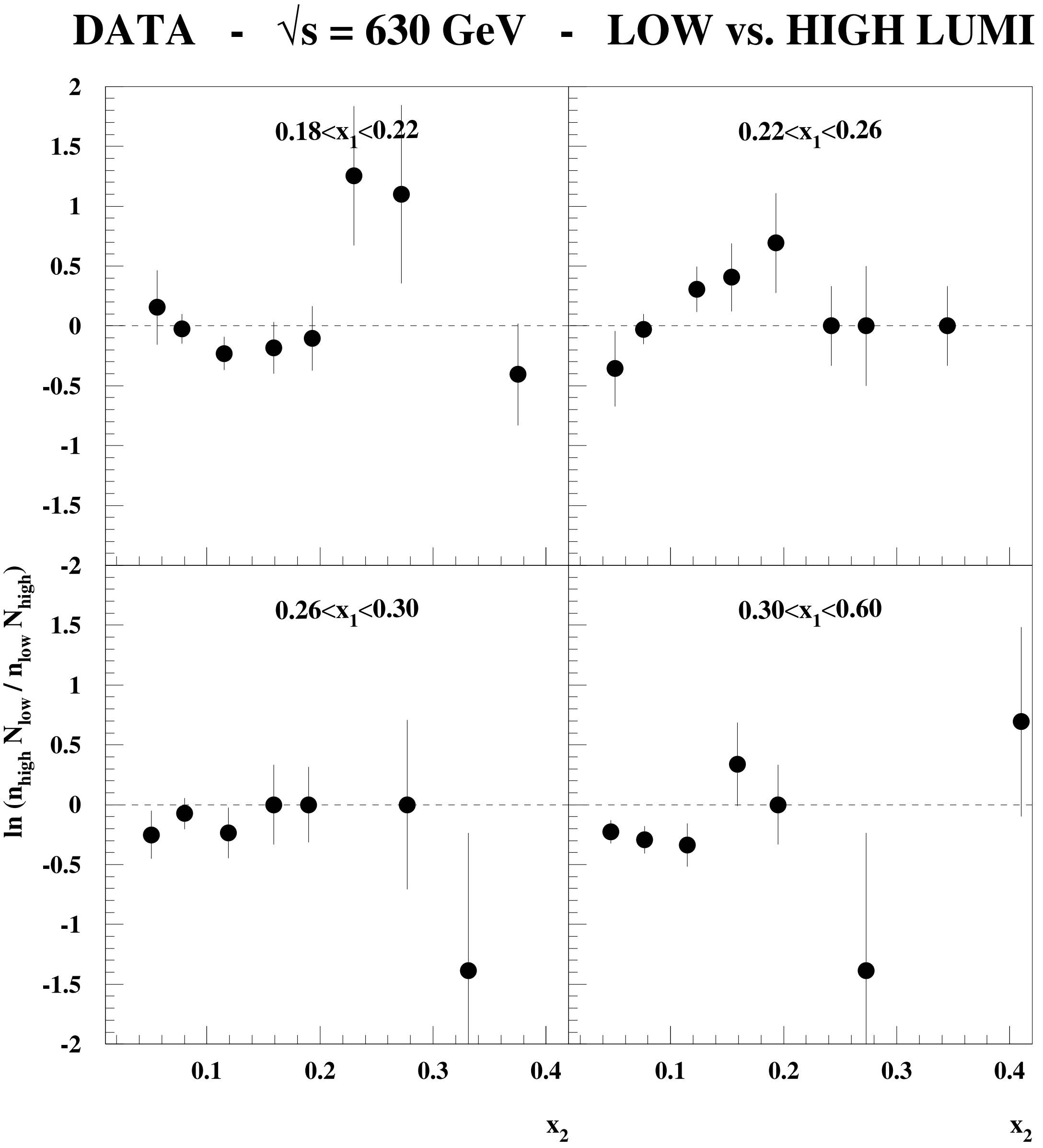

Figure 19: Comparison of the 630 GeV cross section for high and low instantaneous luminosity.

6.5 Detector Smearing Effects

The energy of a jet as measured in the calorimeter is shifted compared to the jet energy at the particle level due to non-linearities in the calorimeter response to low energy particles, unistrumented regions in the calorimeter, particle reconstruction inefficiencies, the underlying event, and electronics noise in the calorimeter cells. The jet energy scale correction [9, 10, 11] corrects the calorimeter-measured jet energy back to the particle level.

The detector effects, however, not only shift the energy of a jet to a different than the particle level value, but also produce a smeared energy distribution, due to the finite resolution of the calorimeter. The smeared jet energy distribution shifts the reconstructed event kinematics x_1, x_2 and Q^2 to different values than the particle level kinematics. This results in a different number of events in an (x_1,x_2,Q^2) bin measured at the calorimeter level than at the particle level.

In order to investigate the detector smearing effects on the event kinematics we use Monte Carlo (MC) samples, generated with HERWIG 5.9 [20] and with CTEQ4M [21] as the input PDF's. The particle level jet energy is smeared with the jet energy resolutions as extractred from the data (see Appendix A). A Z-vertex cut of 50 cm is applied, to match the vertex requirement in the data sample the resolutions were derived from. The jet energy resolutions added to the MC E_T distributions for the two samples are shown in Fig. 20. The particle level (E_T^{par}) and smeared (E_T^{smr}) jet E_T distributions are shown in Fig. 21. In Figures 22 and 23 we plot the smeared jet E_T distributions corresponding to bins of 5 GeV particle jet E_T. In Figures 24 and 25 we plot the particle jet E_T distributions corresponding to bins of 5 GeV smeared jet E_T. No $\Delta\eta$ cut has been applied in the above figures.

After applying the jet E_T and the $\Delta\eta$ cuts *on the smeared jets*, we reconstruct the smeared event kinematics x_1^{smr}, x_2^{smr} and $Q^{2\ smr}$ using the smeared transverse energies of the most forward and most backward jets, $E_{T_1}^{smr}$ and $E_{T_2}^{smr}$, respectively. For the *same sample*, we reconstruct the particle kinematics x_1^{prk}, x_2^{prk} and $Q^{2\ prk}$ using the particle level transverse energies of the most forward and most backward jets. We define the fractional smearing factors for x_1, x_2 and Q^2 as

$$\frac{x_{1,2}^{smr} - x_{1,2}^{prk}}{x_{1,2}^{prk}} \quad \text{and} \quad \frac{Q^{2\ smr} - Q^{2\ prk}}{Q^{2\ prk}}$$

where the variables represent the mean x_1, x_2 and Q^2 values before and after smearing. The fractional smearing factors for x_1 and x_2 are plotted as a function of the smeared variables in Figures 26 and 27 for the 1800 and 630 GeV samples, respectively. The fractional smearing factors for Q^2, plotted as a function of the smeared variable, are shown in Figure 28.

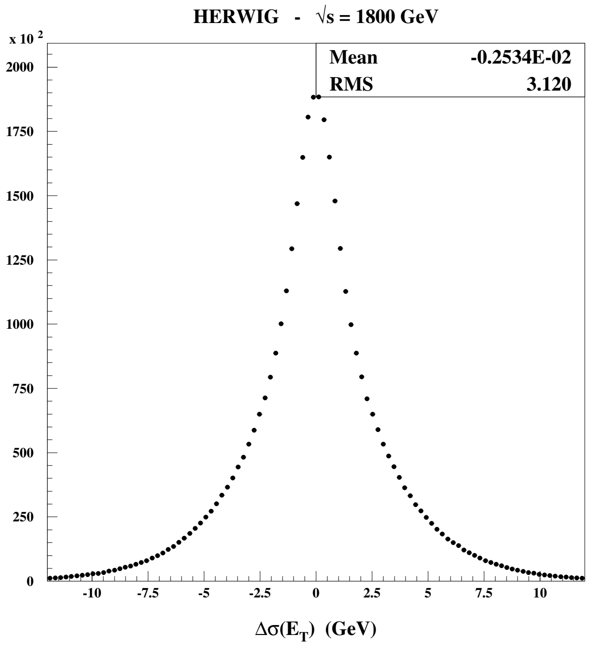

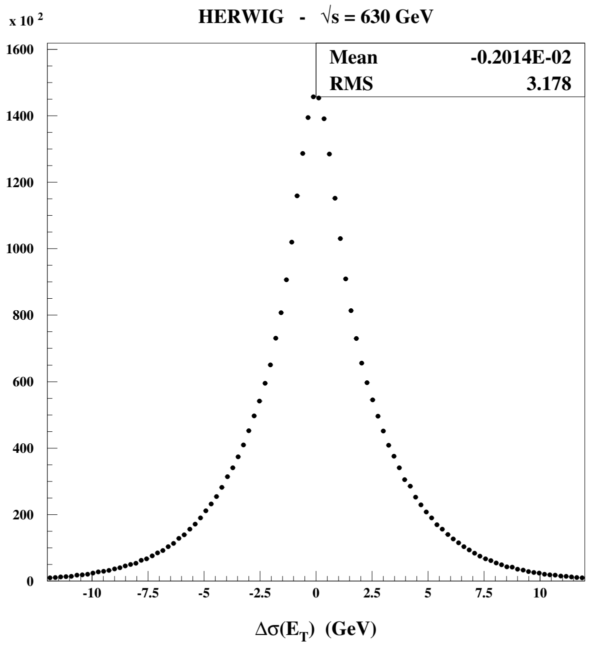

Figure 20: Jet energy resolutions used to smear the HERWIG jets. The Z-vertex cut has been applied.

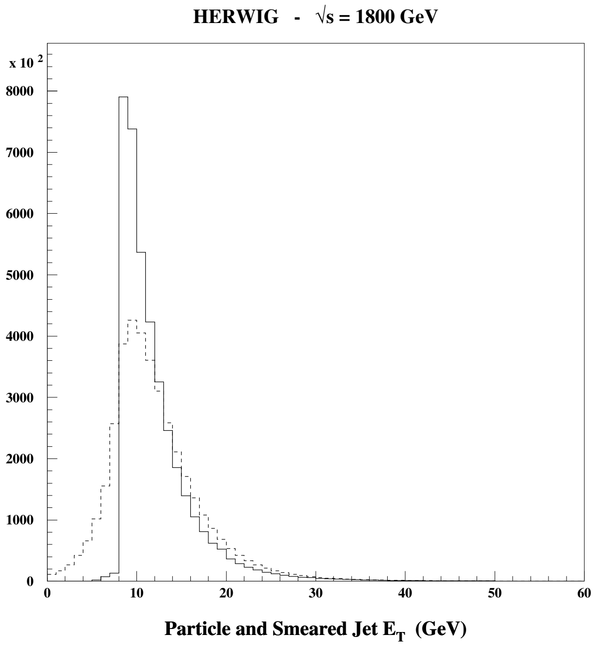

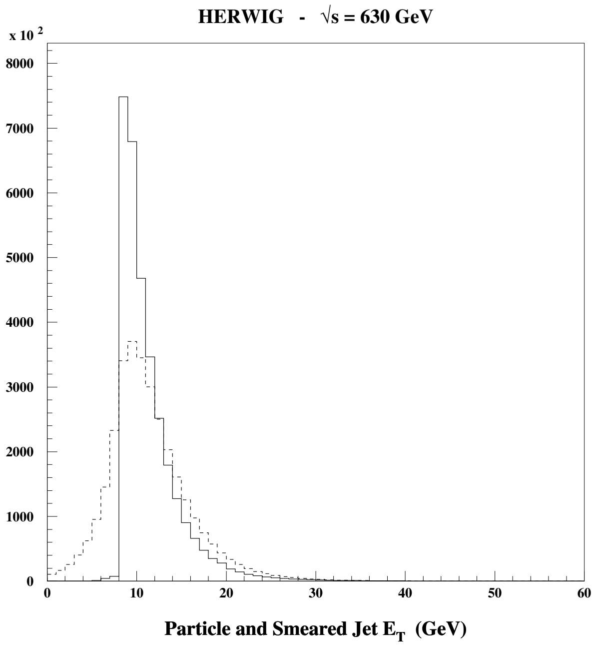

Figure 21: Particle (solid line) and Smeared (dashed line) jet E_T distributions. The Z-vertex cut has been applied.

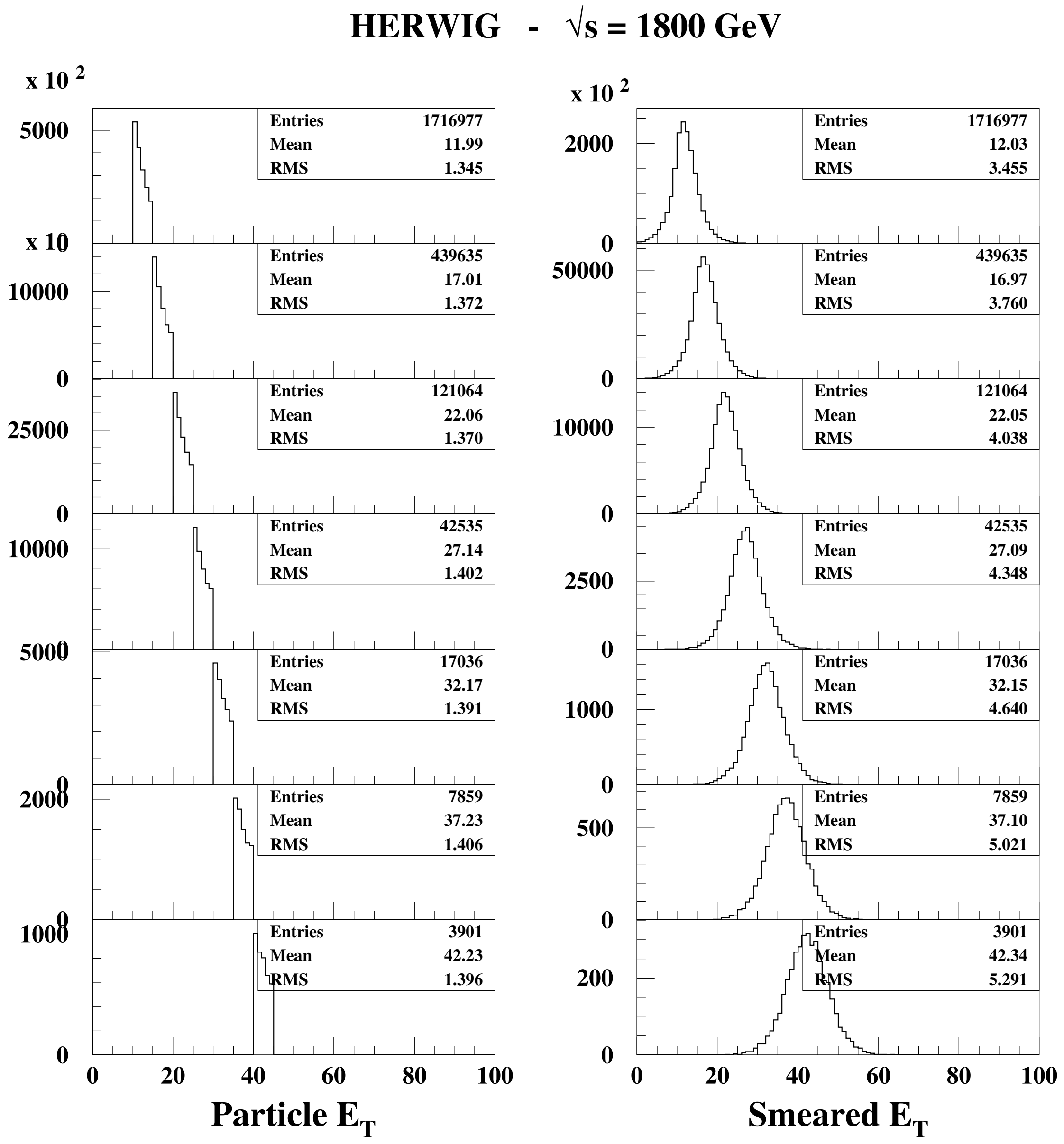

Figure 22: Smeared jet E_T distributions for different particle E_T bins for the 1800 GeV HERWIG sample. The Z-vertex cut has been applied.

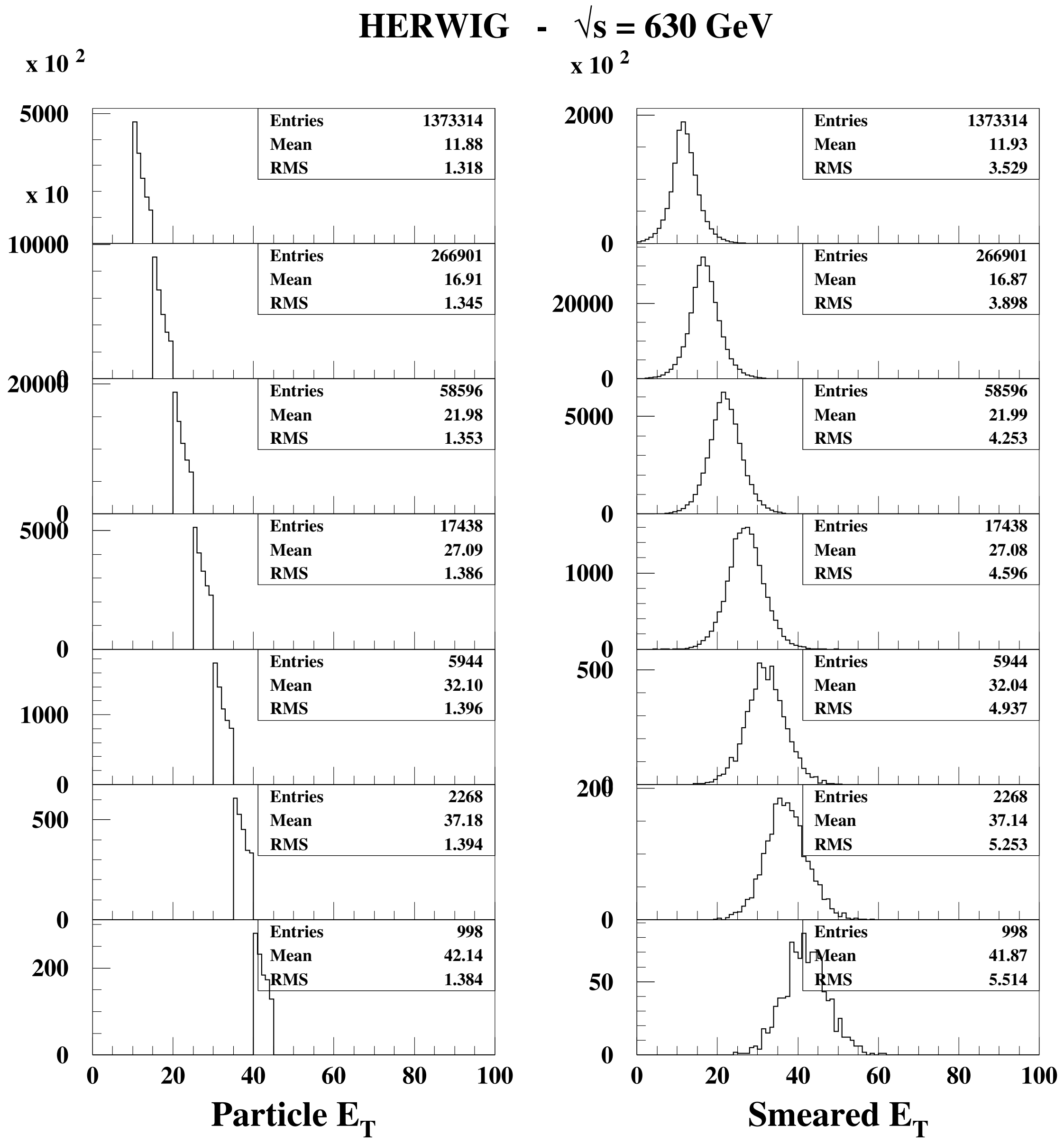

Figure 23: Smeared jet E_T distributions for different particle E_T bins for the 630 GeV HERWIG sample. The Z-vertex cut has been applied.

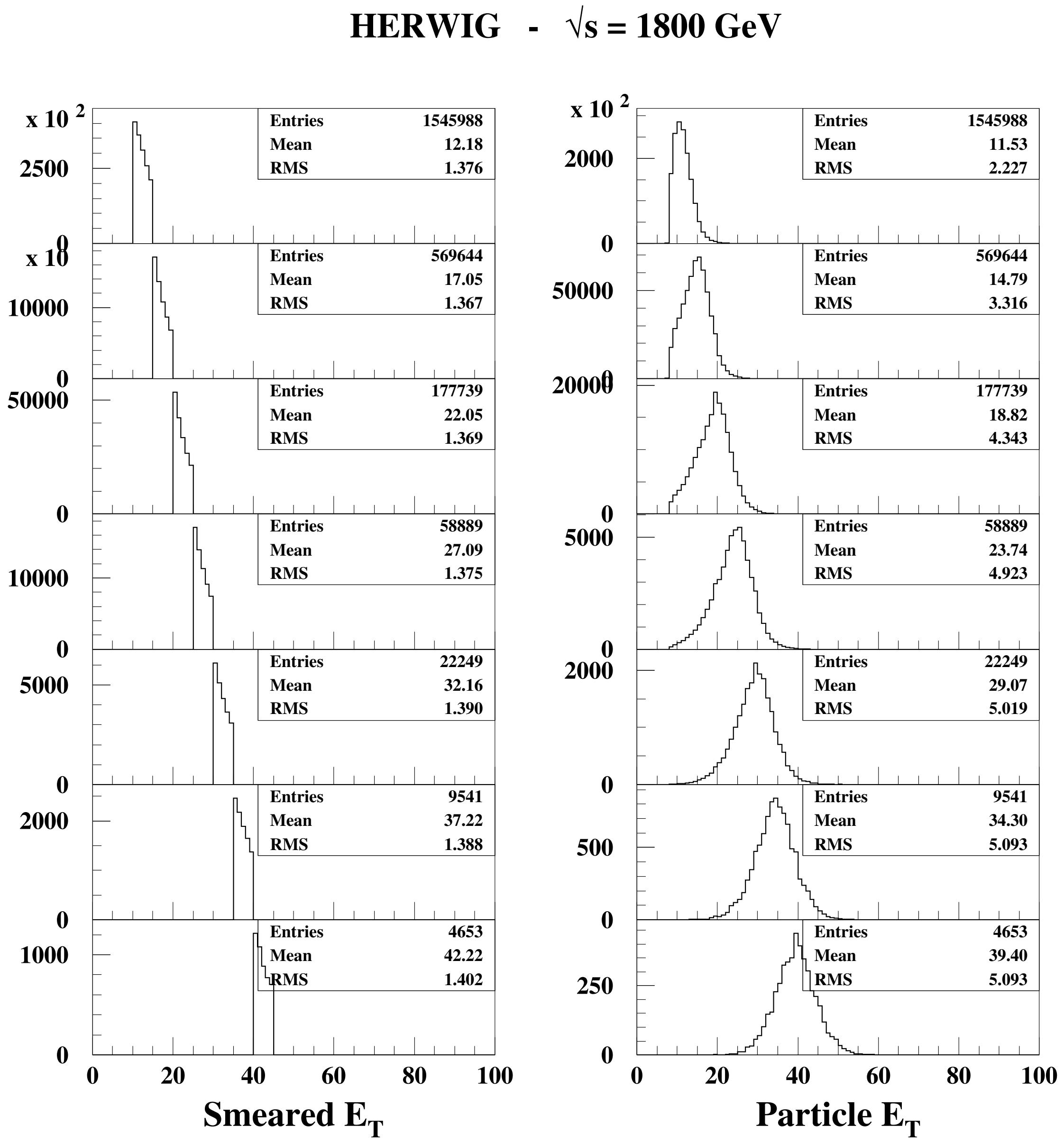

Figure 24: Particle jet E_T distributions for different smeared E_T bins for the 1800 GeV HERWIG sample. The Z-vertex cut has been applied.

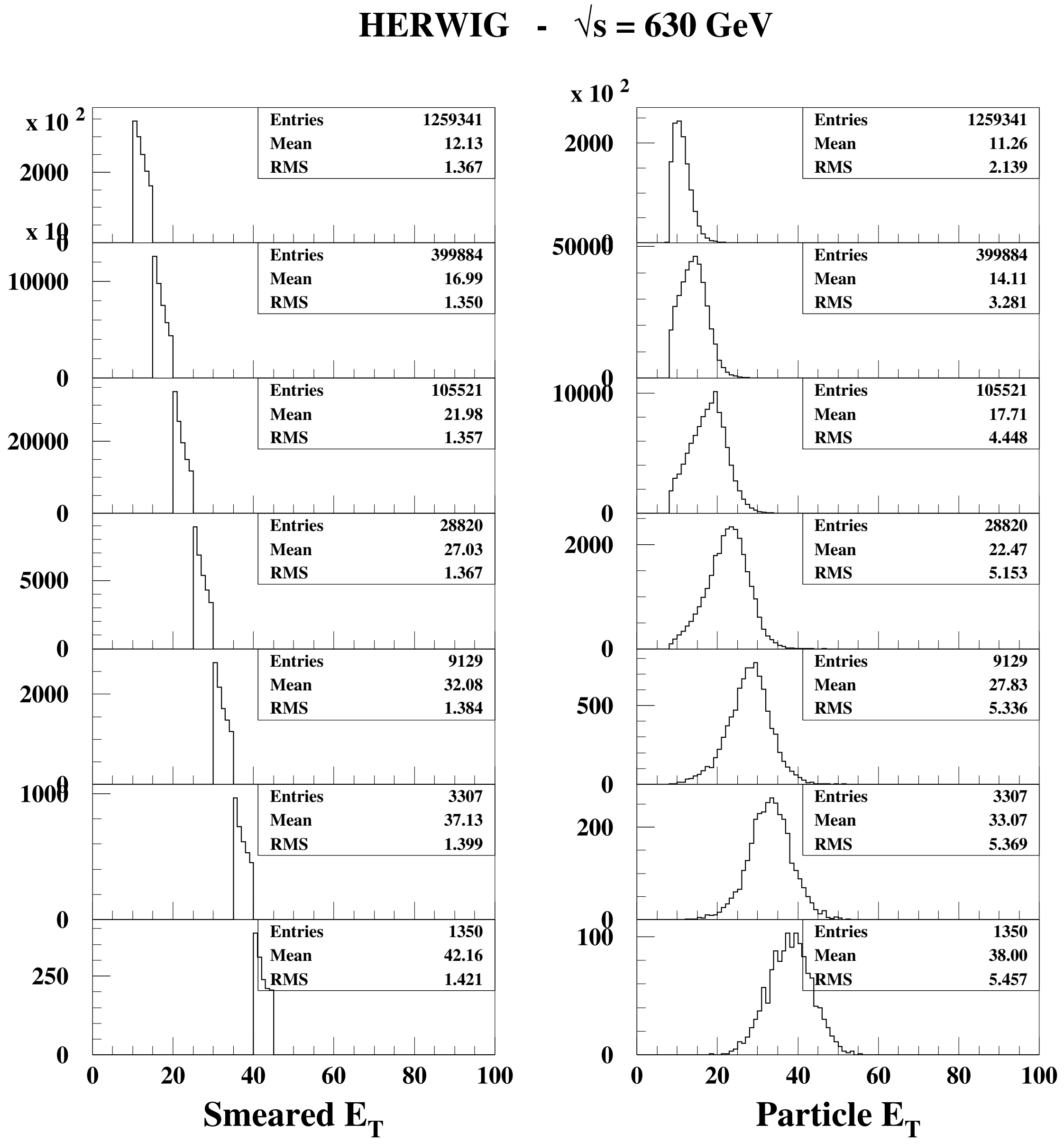

Figure 25: Particle jet E_T distributions for different smeared E_T bins for the 630 GeV HERWIG sample. The Z-vertex cut has been applied.

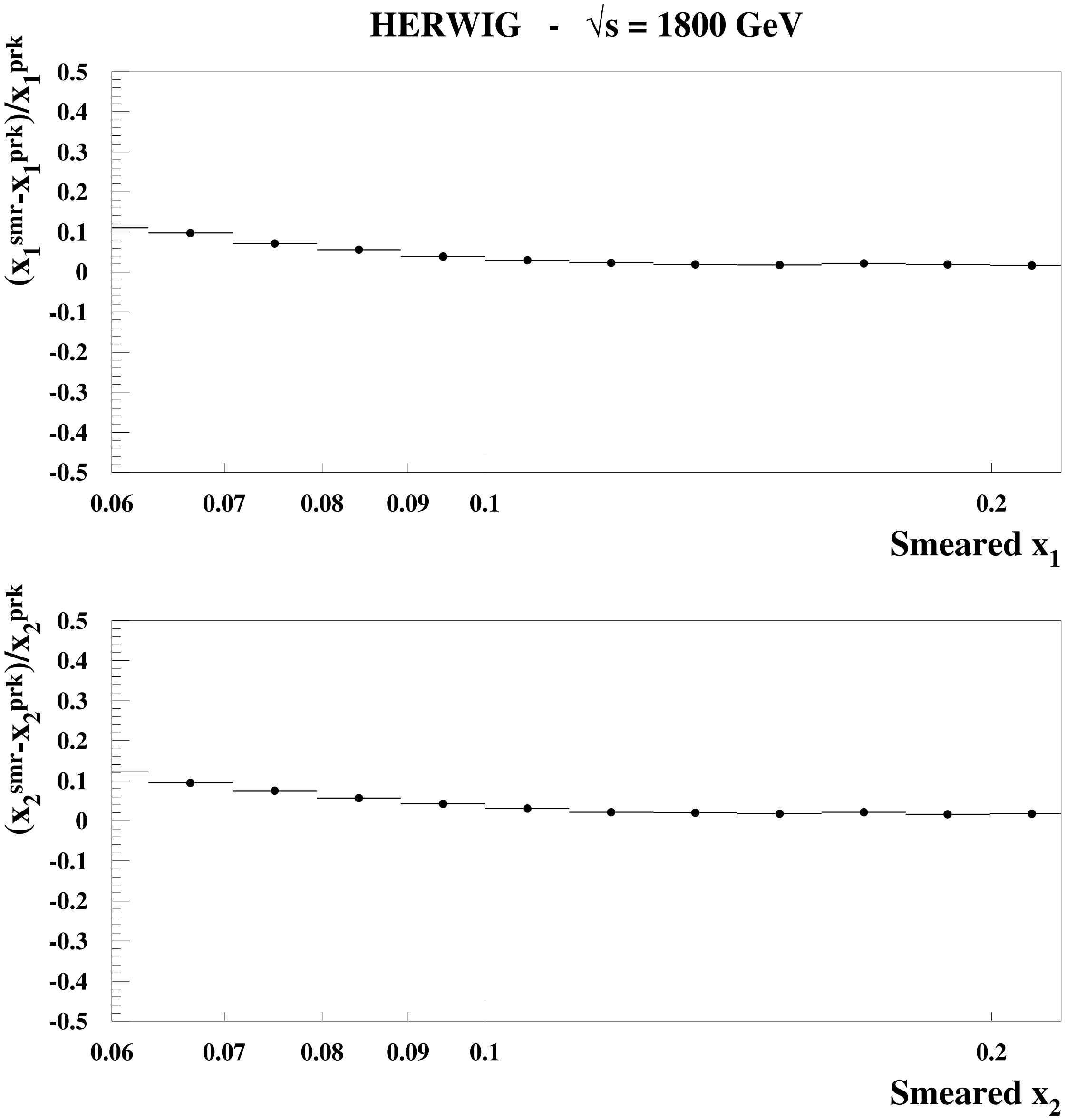

Figure 26: Fractional smearing factors for x_1 and x_2 as a function of the smeared variables for the 1800 GeV HERWIG sample. The $E_T > 20$ GeV and the $\Delta\eta > 2$ cuts have been applied on the *smeared* variables. The Z-vertex cut has also been applied.

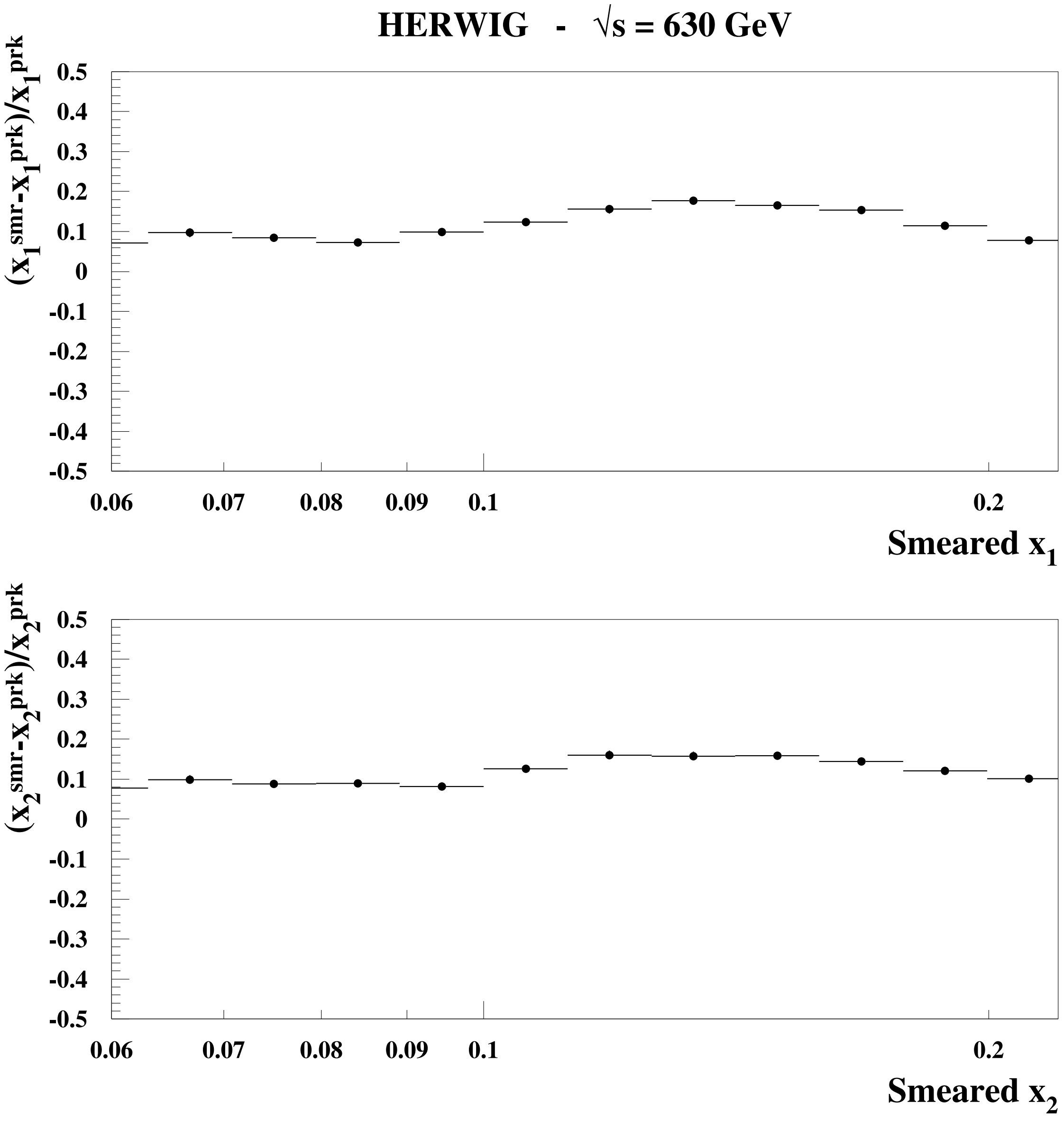

Figure 27: Fractional smearing factors for x_1 and x_2 as a function of the smeared variables for the 630 GeV HERWIG sample. The $E_T > 20$ GeV and the $\Delta\eta > 2$ cuts have been applied on the *smeared* variables. The Z-vertex cut has also been applied.

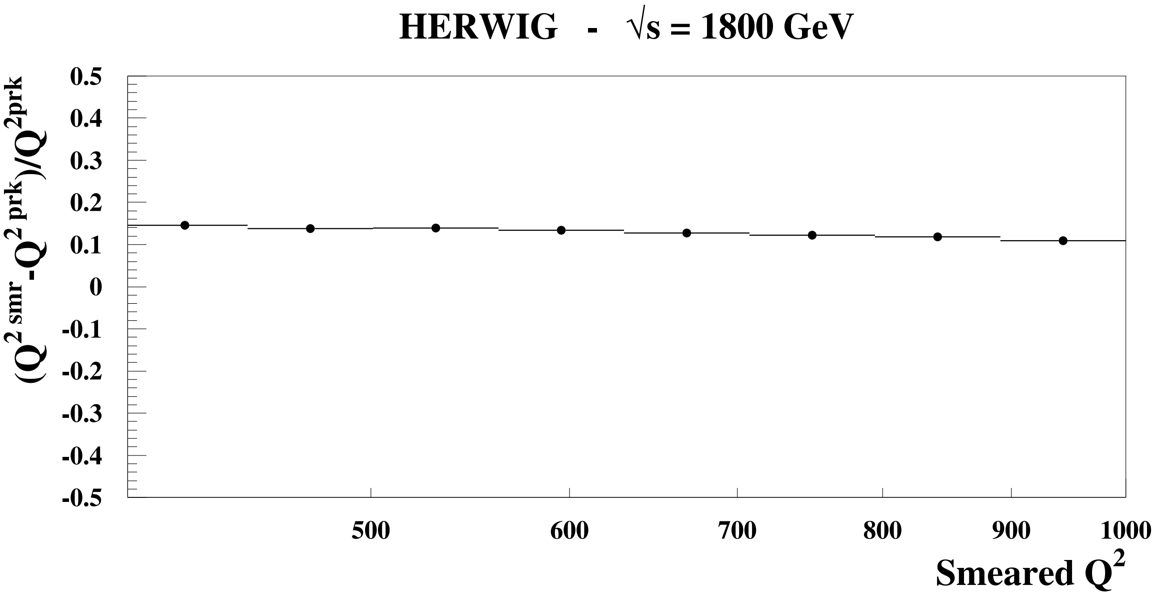

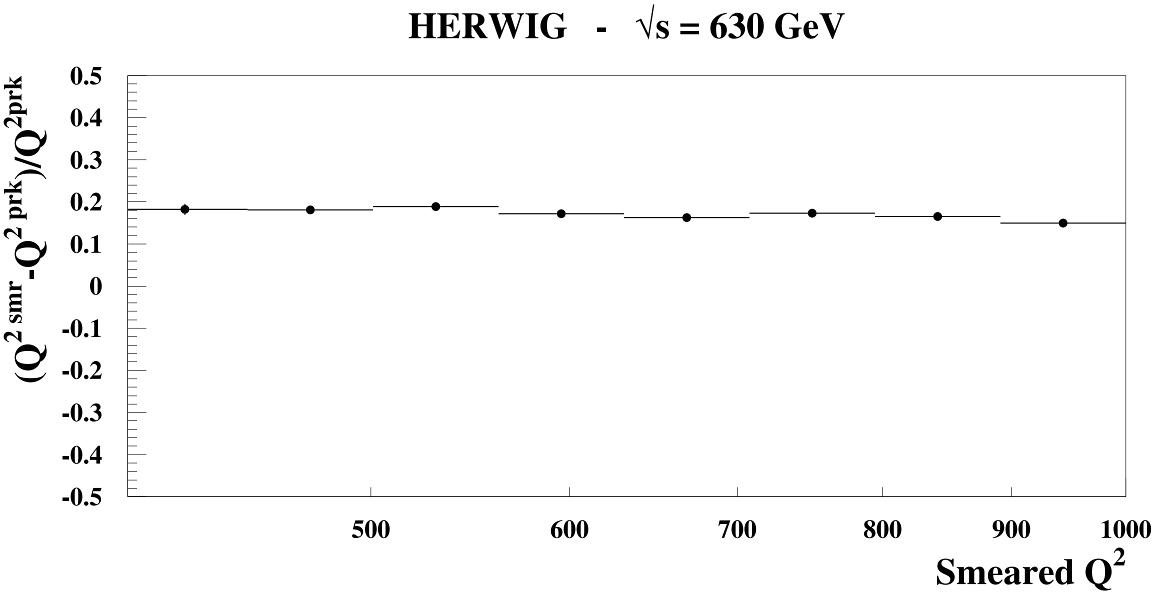

Figure 28: Fractional smearing factor for Q^2 as a function of the smeared variable for the 1800 and 630 GeV HERWIG samples. The $E_T > 20$ GeV and the $\Delta\eta > 2$ cuts have been applied on the *smeared* variables. The Z-vertex cut has also been applied.

6.6 Unsmearing of the Cross Section

The smearing of the jet energy results in a smearing of the event kinematics and thus, of the cross section in a (x_1,x_2,Q^2) bin, as discussed in the previous paragraph. An additional danger arises for events with jets of particle transverse energy slightly lower or higher than the 20 GeV cut. In those cases, the event can be counted when it should not have been, or, in contrast, completely lost. The effect is illustrated in Fig. 29. Let n be the initial number of events in a bin. Assume that the event in question has one jet of particle $E_T = 19$ GeV and smeared (calorimeter) $E_T = 21$ GeV, and the other jet well above 20 GeV. After considering the above event, the number of events in the bin will be $n+1$ at the calorimeter level, whereas it would have still be equal to n at the particle level. The effect can be reversed for jets of E_T slighly higher than 20 GeV. In the case that such an event has an third jet of particle E_T well above 20 GeV (Fig. 30), the event will be reconstructed with a different configuration ($\Delta\eta$) and thus, counted in the wrong (x_1,x_2,Q^2) bin.

In order to remove the effects of detector smearing from the measured cross section in each (x_1, x_2, Q^2) bin, we compare the particle level Monte Carlo cross section to the smeared Monte Carlo cross section in the bin.

First, the minimum jet E_T cut of 20 GeV is applied on the particle level transverse energy of the jets (E_T^{par}). For the event configuration that results after this cut, i.e., for a rapidity interval $\Delta\eta^{par}$, the particle level event kinematics x_1^{par}, x_2^{par} and $Q^{2\ par}$ are calulated using E_T^{par} and $\Delta\eta^{par}$. After applying the $\Delta\eta^{par} > 2$ cut, the particle cross section $\sigma^{par}(x_1^{par}, x_2^{par}, Q^{2\ par})$ is calculated in each bin.

The particle jet E_T is then smeared using the resolutions extracted from the data yielding an E_T^{smr}, as discussed in the previous paragraph. The minimum jet E_T cut of 20 GeV is applied on E_T^{smr}. For the event configuration that results after this cut, i.e., for a rapidity interval $\Delta\eta^{smr}$, the smeared (i.e., calorimeter level) event kinematics x_1^{smr}, x_2^{smr} and $Q^{2\ smr}$ are calulated using E_T^{smr} and $\Delta\eta^{smr}$. After applying the $\Delta\eta^{smr} > 2$ cut, the smeared cross section $\sigma^{smr}(x_1^{smr}, x_2^{smr}, Q^{2\ smr})$ is calculated in each bin. This is shown if Figures 31 and 32 for the $\sqrt{s} = 1800$ and 630 GeV HERWIG samples, respectively. Also shown in the above figures is the cross section measured from the data. Apart from the overall normalization and fluctuations of the data cross section in some bins, the shape of the cross section is consistent in MC and data.

The ratio of the particle cross section to the smeared cross section in each bin (which reduces to the ratio of number of events, M^{par} and M^{smr}, respectively) is used as an unsmearing correction to the measured data cross section in the bin:

$$\sigma^{unsmr}(x_1, x_2, Q^2) = \frac{N^{meas}}{L} \cdot \frac{M^{par}}{M^{smr}} \tag{44}$$

The statistical error on the unsmeared cross section in each bin is then given by:

$$\Delta\sigma^{unsmr}(x_1, x_2, Q^2) = \sigma^{unsmr}(x_1, x_2, Q^2) \cdot \left[\frac{1}{N^{meas}} + \frac{1}{M^{par}} + \frac{1}{M^{smr}}\right]^{\frac{1}{2}} \tag{45}$$

It should be noted here that the particle kinematics x_1^{par}, x_2^{par} and $Q^{2\ par}$, are different than the x_1^{prk}, x_2^{prk} and $Q^{2\ prk}$ kinematics discussed in the previous paragraph. The latter have been calculated after the minimum jet E_T cut has been applied to the *smeared* E_T and are useful for calculating the bin resolutions; however, they can *not* be used for calculating the unsmearing factors, due to the effect of the detector smearing on the events with jets of transverse energy around 20 GeV.

The unsmearing correction factors, M^{par}/M^{smr}, are shown in Figures 33 and 34 for the 1800 and 630 GeV samples, respectively.

The unsmeared cross section given from eq.(44) depends to some extend on the input Parton Distribution Function to the Monte Carlo. In order to remove this dependence, we should in principle follow an iteration procedure: calculate the ratio of the measured data cross section to the smeared MC cross section in each bin of *measured* (x_1,x_2,Q^2), apply this ratio as a weight to the MC events using the *particle* kinematics, smear again the MC, re-calculate the ratio of the measured data cross section to the new smeared MC cross section, and iterate the procedure until this ratio converges to unity. At that point, the unsmearing factors can be used to obtain an unsmeared data cross section that does not depend on the input PDF. In this analysis, however, the iteration procedure can not work. A MC event with a certain set of smeared kinematics does not always have a corresponding set of particle kinematics, due to the 20 GeV cut being applied separately on the smeared and particle jet E_T. Therefore, in order to account for the dependence on the input PDF, the data cross section is unsmeared also using a very different PDF set in the MC, and the deviation from the nominal unsmeared cross section is assigned as a systematic uncertainty in each (x_1,x_2,Q^2) bin (see section 7.4.3).

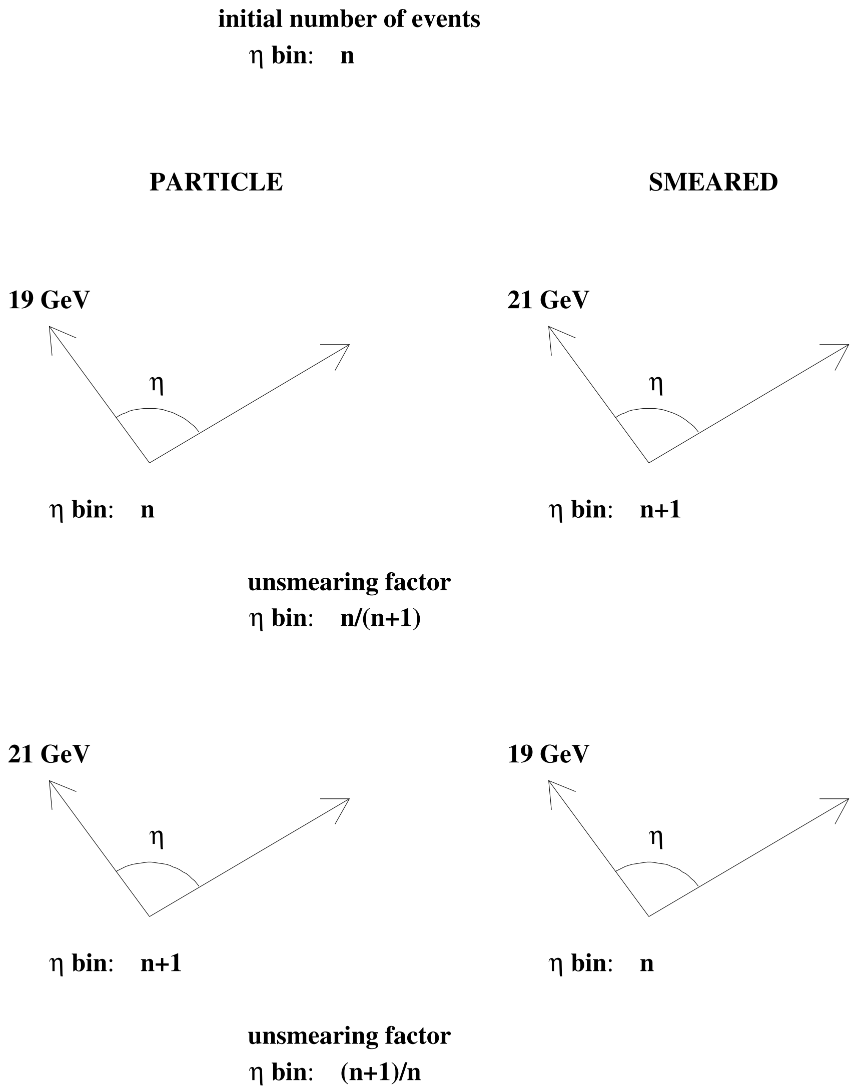

Figure 29: Examples of the effect of detector smearing on events with two jets.

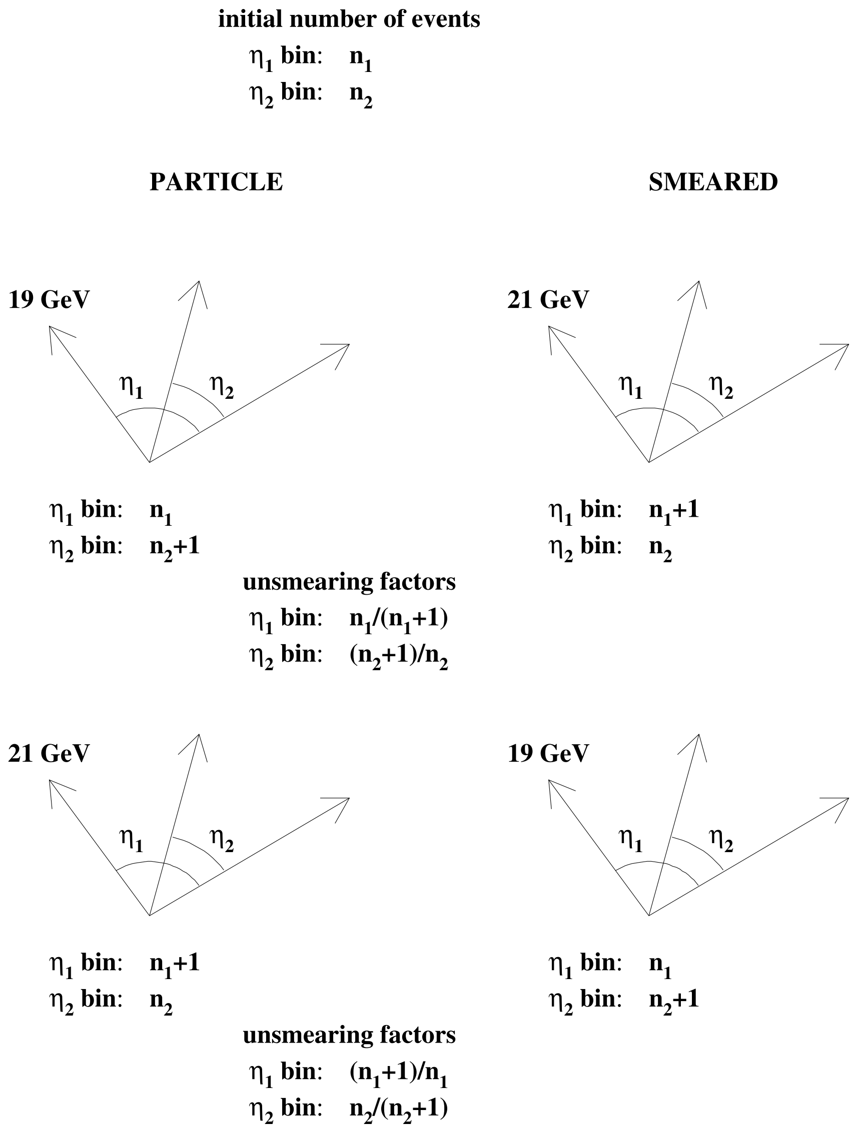

Figure 30: Examples of the effect of detector smearing on events with three jets.

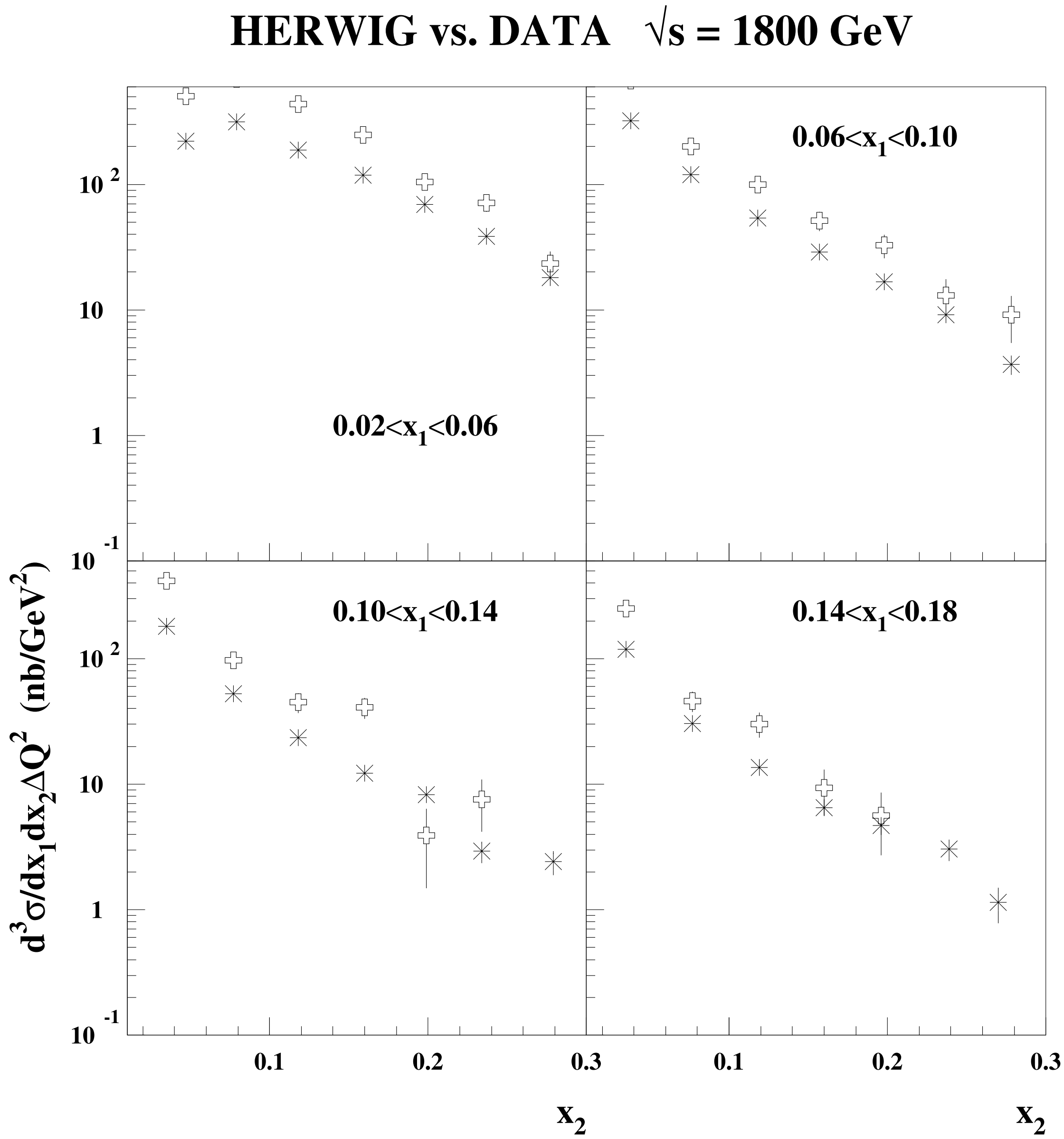

Figure 31: The dijet cross section in (x_1,x_2) bins as measured in the data (crosses) and in the HERWIG (stars) samples at $\sqrt{s} = 1800$ GeV. The data cross section is shown before any unsmearing procedure. The HERWIG sample has been smeared using data-extracted jet energy resolutions.

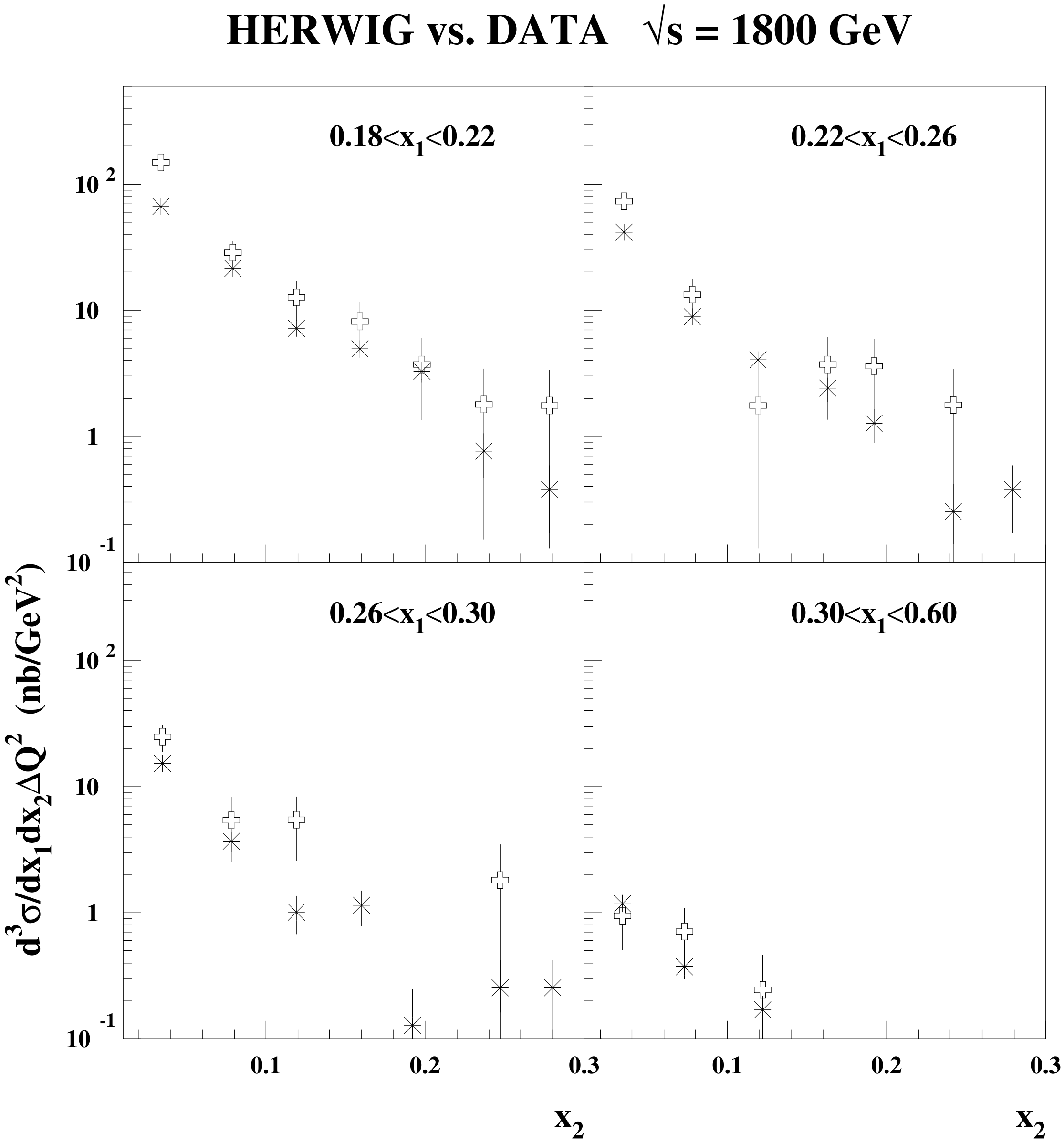

Figure 31: The dijet cross section in (x_1,x_2) bins as measured in the data (crosses) and in the HERWIG (stars) samples at $\sqrt{s} = 1800$ GeV. The data cross section is shown before any unsmearing procedure. The HERWIG sample has been smeared using data-extracted jet energy resolutions.

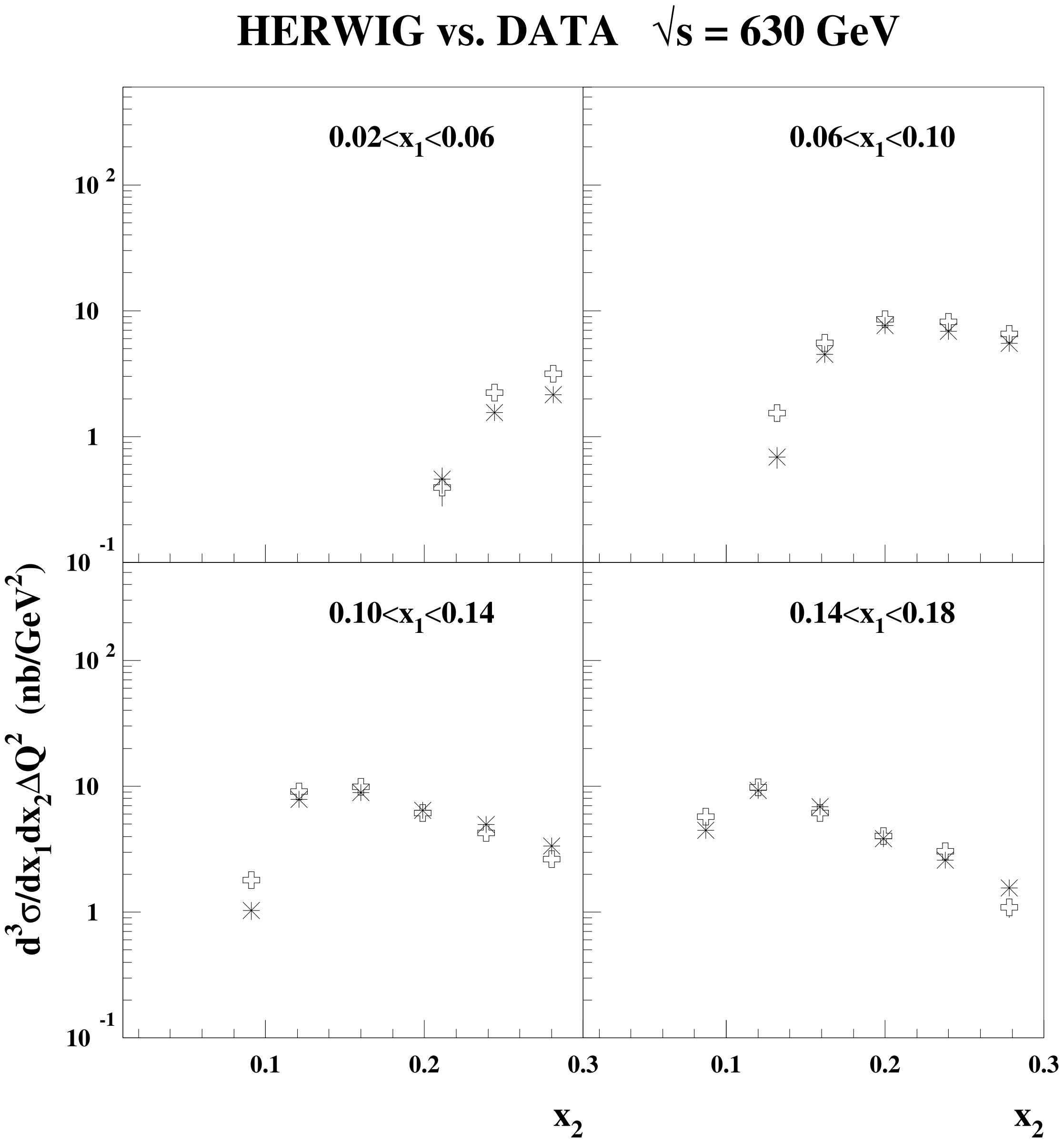

Figure 32: The dijet cross section in (x_1,x_2) bins as measured in the data (crosses) and in the HERWIG (stars) samples at $\sqrt{s} = 630$ GeV. The data cross section is shown before any unsmearing procedure. The HERWIG sample has been smeared using data-extracted jet energy resolutions.

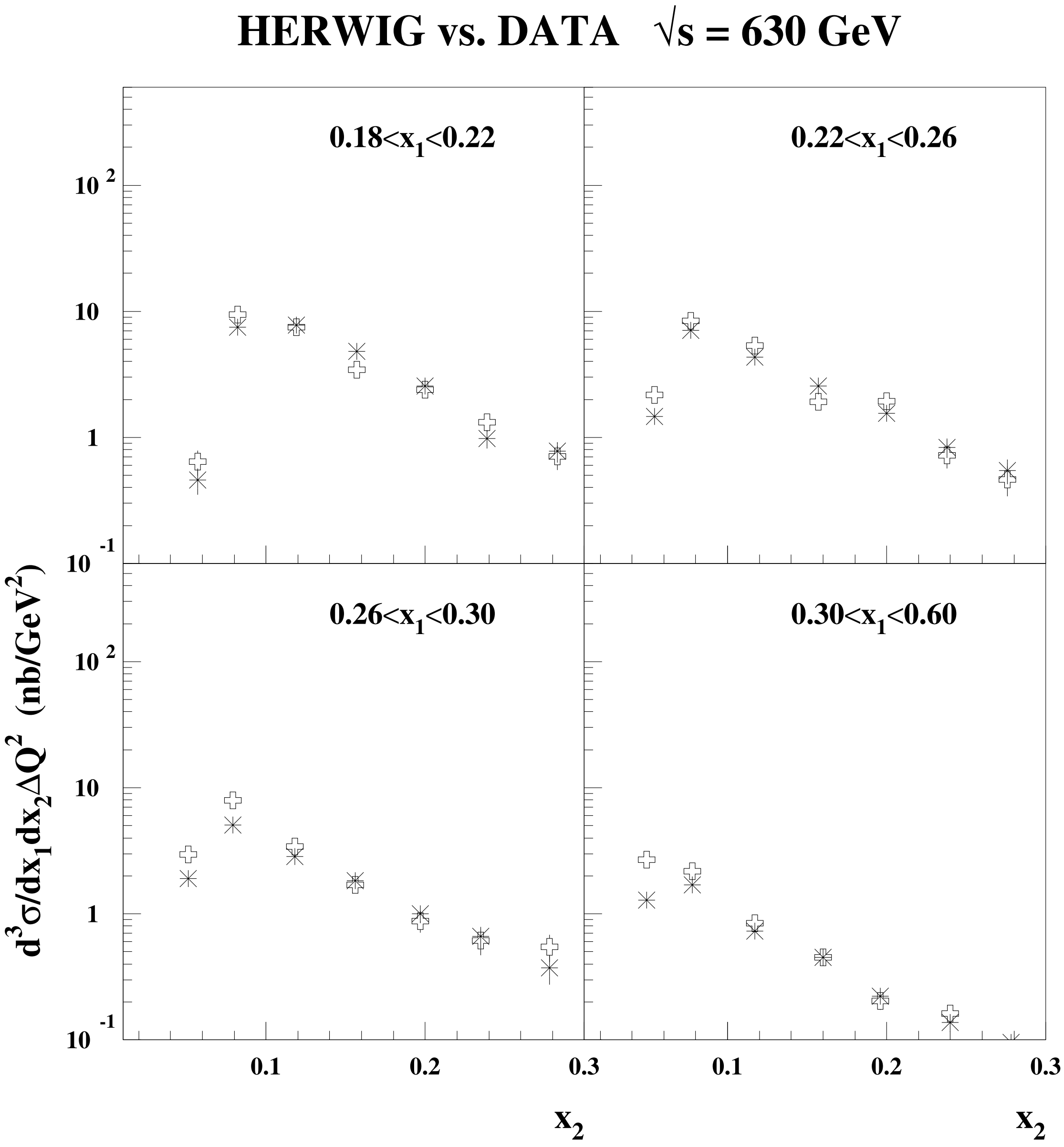

Figure 32: The dijet cross section in (x_1,x_2) bins as measured in the data (crosses) and in the HERWIG (stars) samples at $\sqrt{s} = 630$ GeV. The data cross section is shown before any unsmearing procedure. The HERWIG sample has been smeared using data-extracted jet energy resolutions.

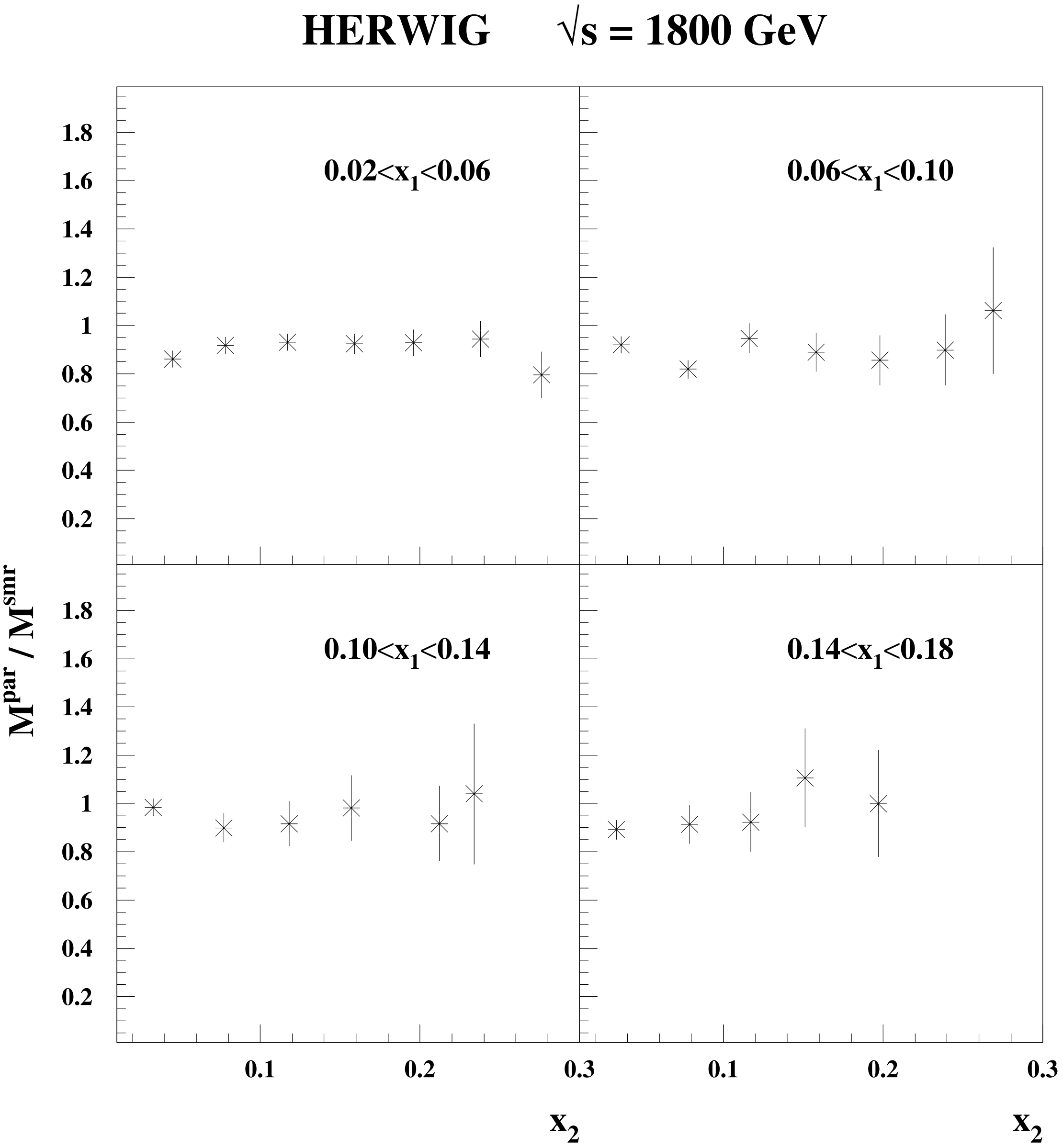

Figure 33: Unsmearing factors at $\sqrt{s}$ = 1800 GeV. The error bars represent statistical uncertainties.

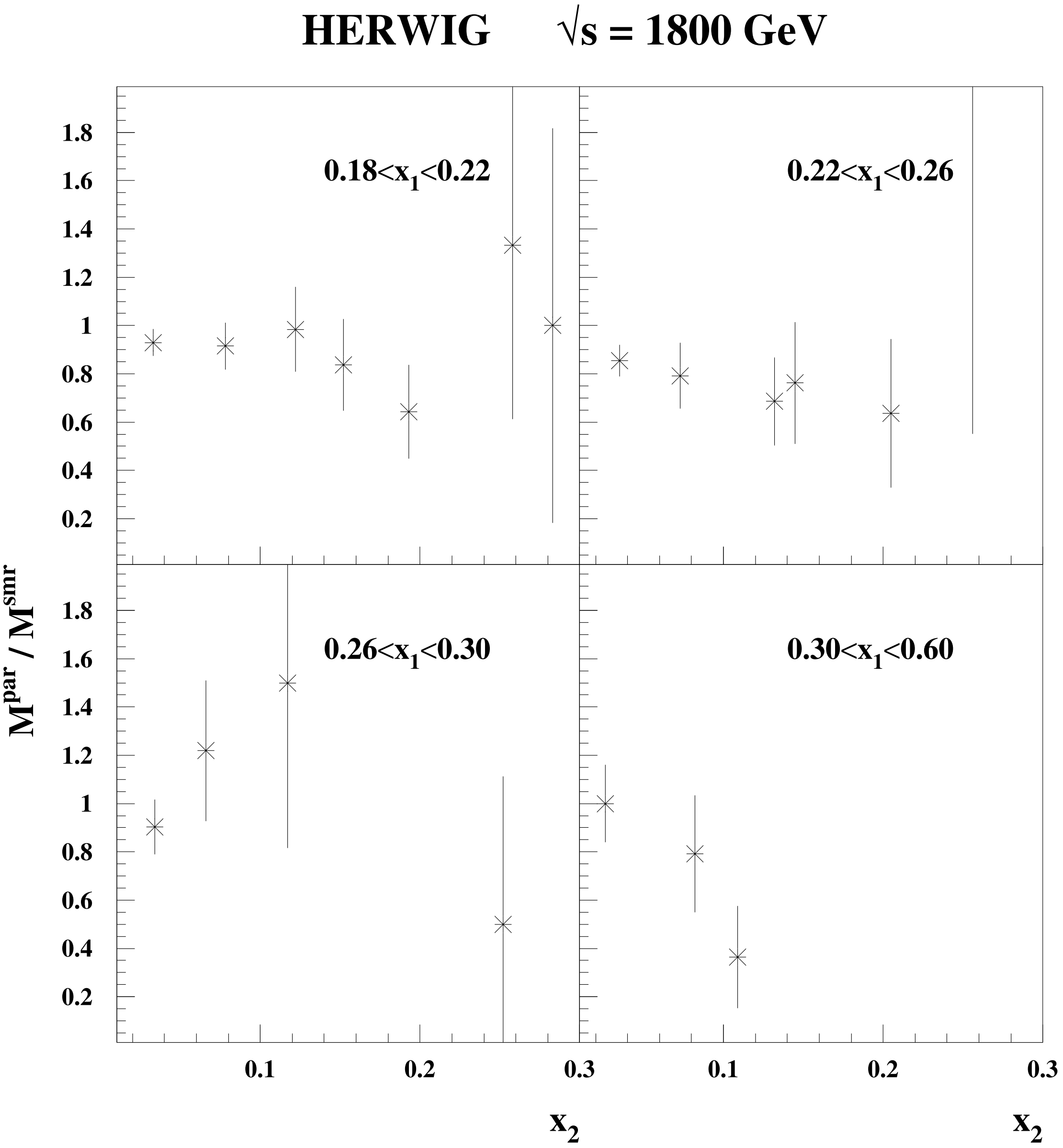

Figure 33: Unsmearing factors at $\sqrt{s} = 1800$ GeV. The error bars represent statistical uncertainties.

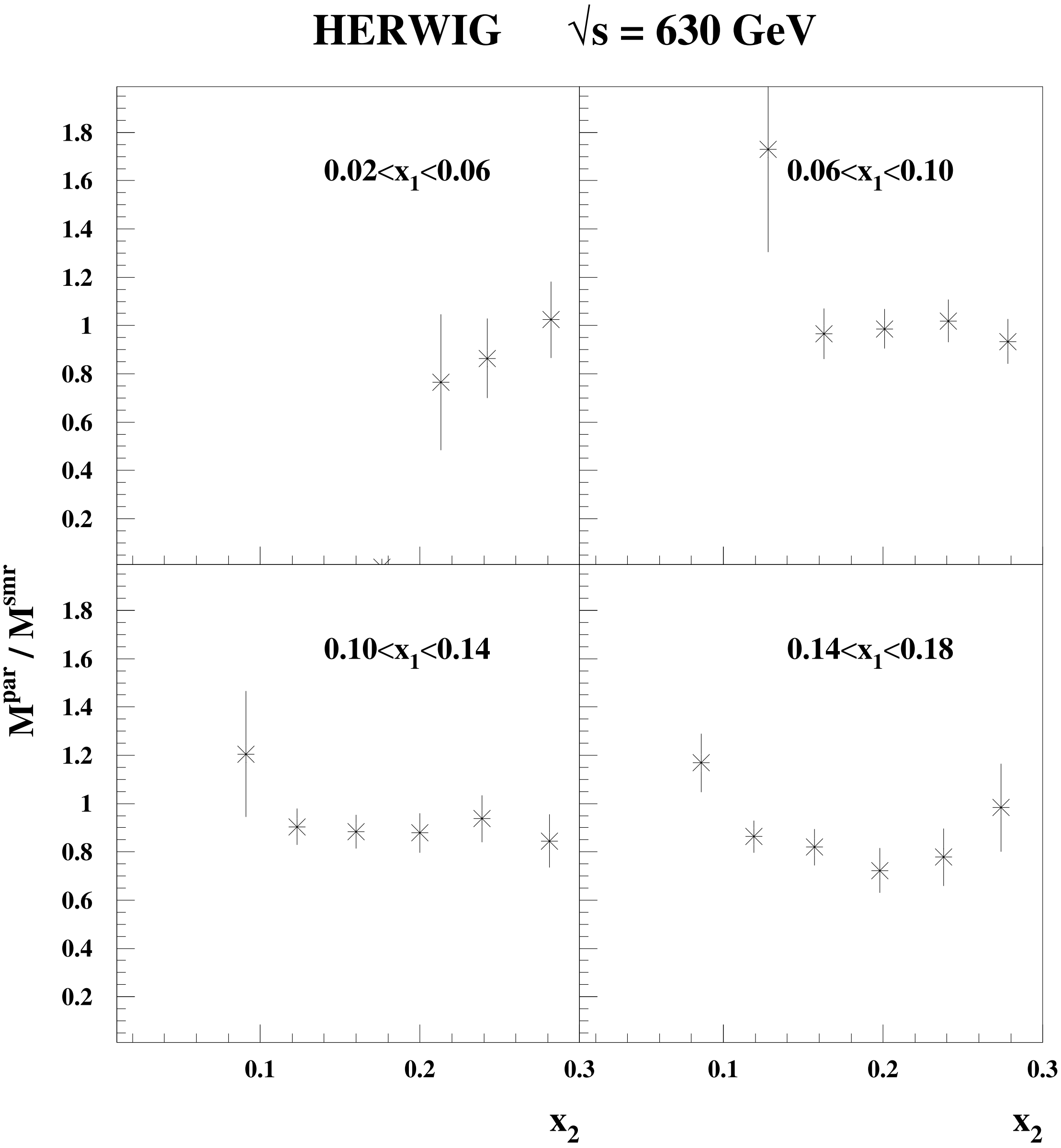

Figure 34: Unsmearing factors at $\sqrt{s} = 630$ GeV. The error bars represent statistical uncertainties.

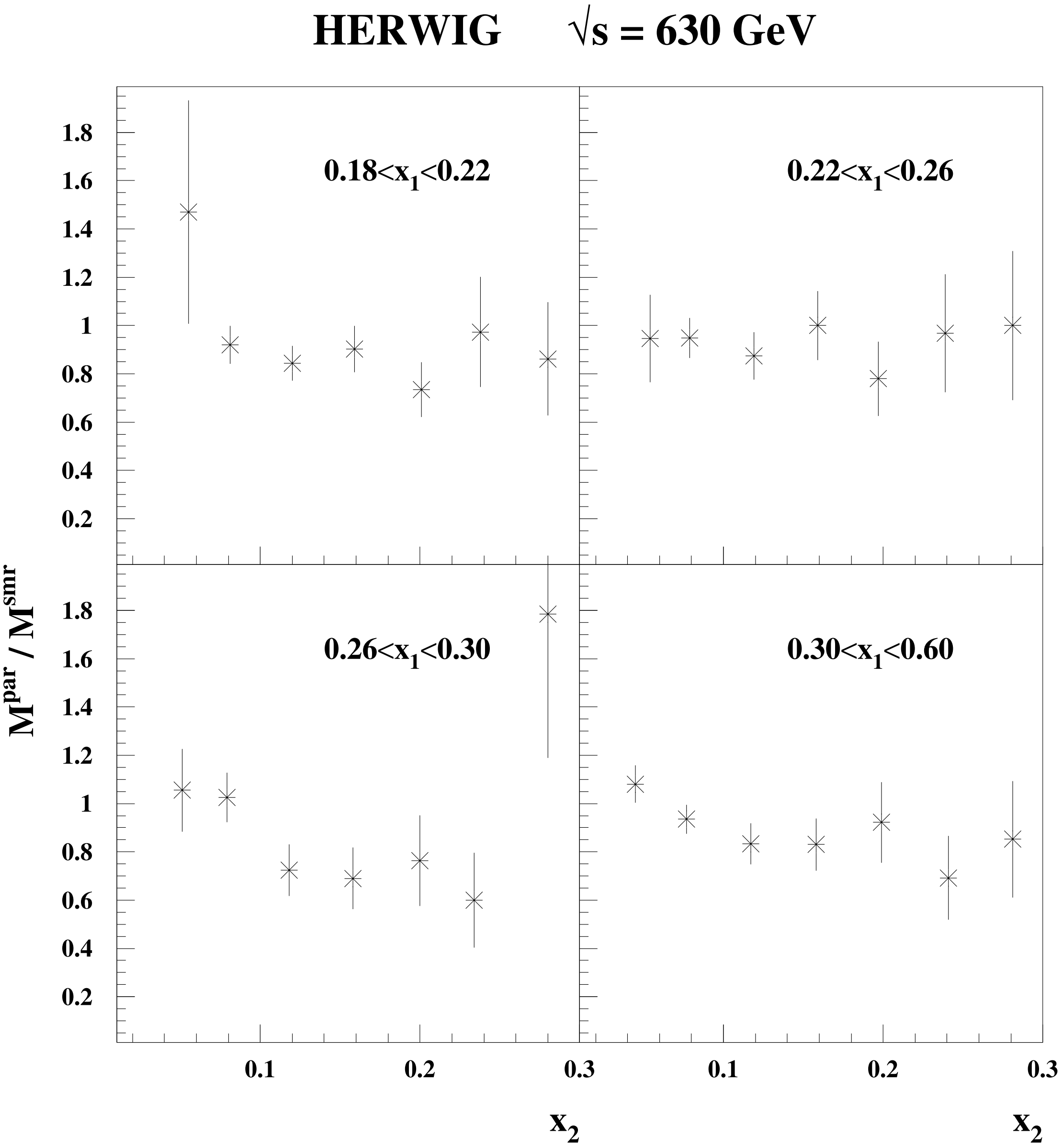

Figure 34: Unsmearing factors at $\sqrt{s}$ = 630 GeV. The error bars represent statistical uncertainties.

6.6.1 Test of the Unsmearing Method

In order to test the unsmearing procedure, we use a different Monte Carlo sample, generated with ISAJET. First we measure the particle–level cross section in bins of (x_1,x_2,Q^2). Then we smear the particle–level jet E_T's and measure again the dijet cross section. We unsmear the latter using the same unsmearing factors we use in the data (i.e., from HERWIG), and compare the unsmeared cross section to the particle–level one. The results are shown in Fig. 35. To quantify the comparison, we calculate the logarithms of the ratios of the unsmeared to the particle–level cross sections (shown in Fig. 36). The $\chi^2/d.o.f.$ for the consistency of the logarithms of the ratios with zero is equal to 1.46.

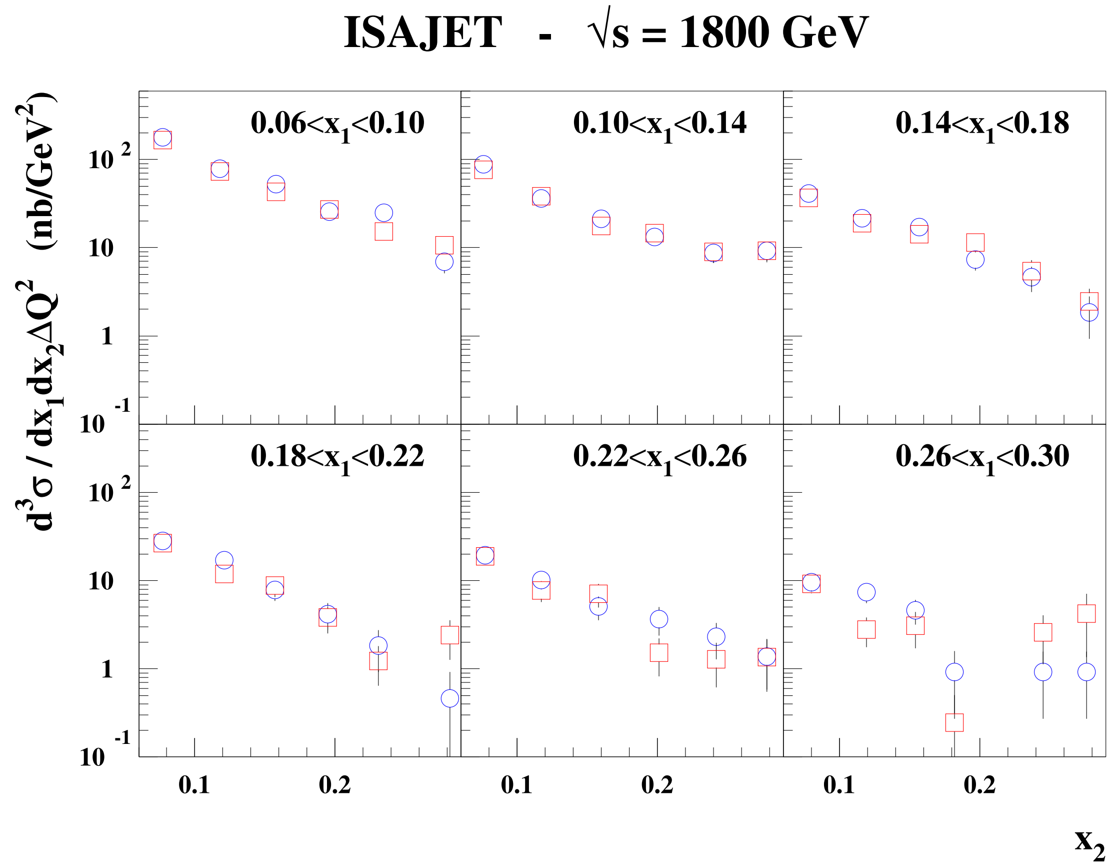

Figure 35: Unsmearing test using ISAJET Monte Carlo. The open circles represent the particle–level dijet cross section. The open squares represent the unsmeared dijet cross section (using the HERWIG unsmearing factors). The error bars represent statistical uncertainties.

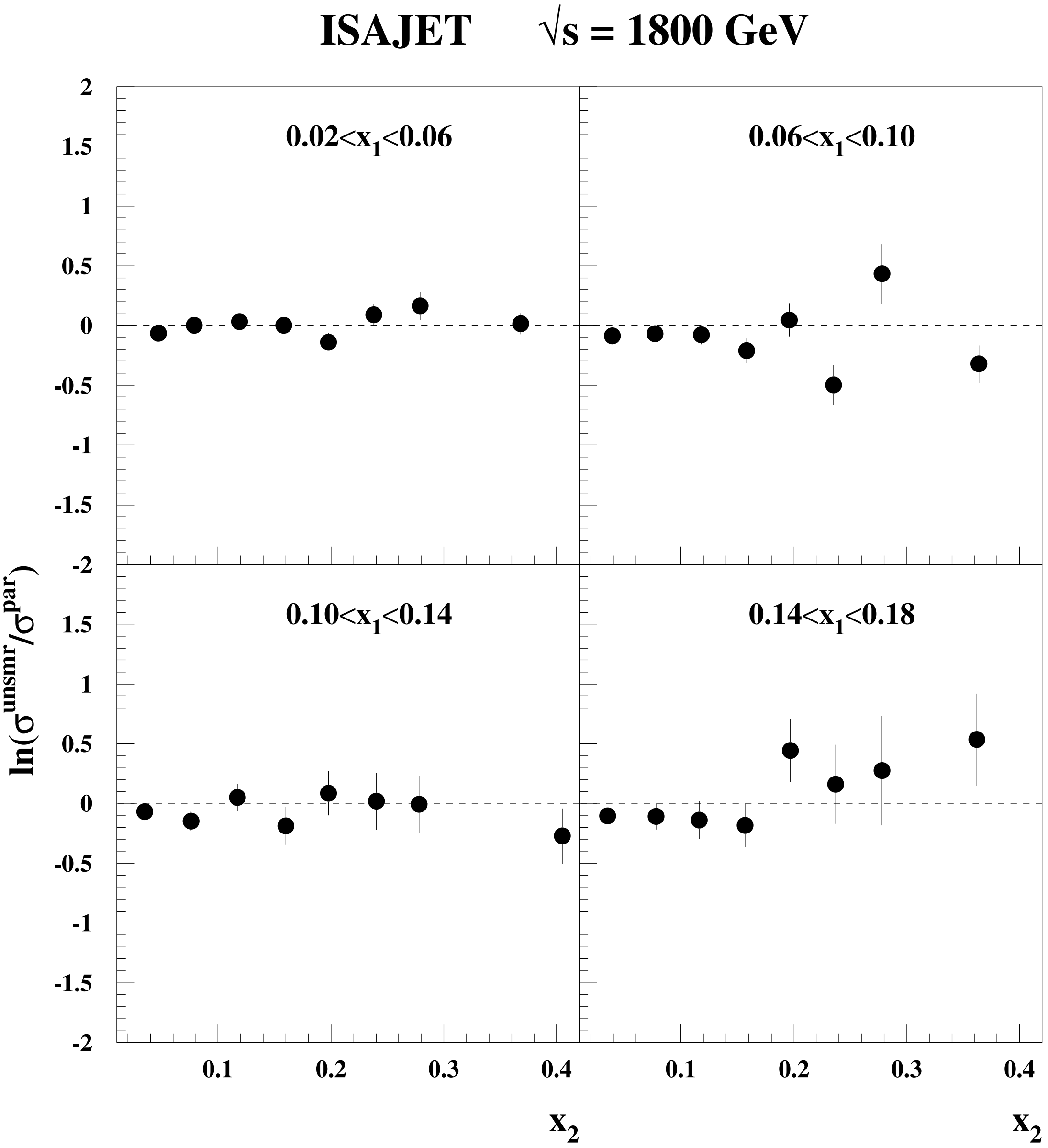

Figure 36: Unsmearing test using ISAJET Monte Carlo. The error bars represent statistical uncertainties.

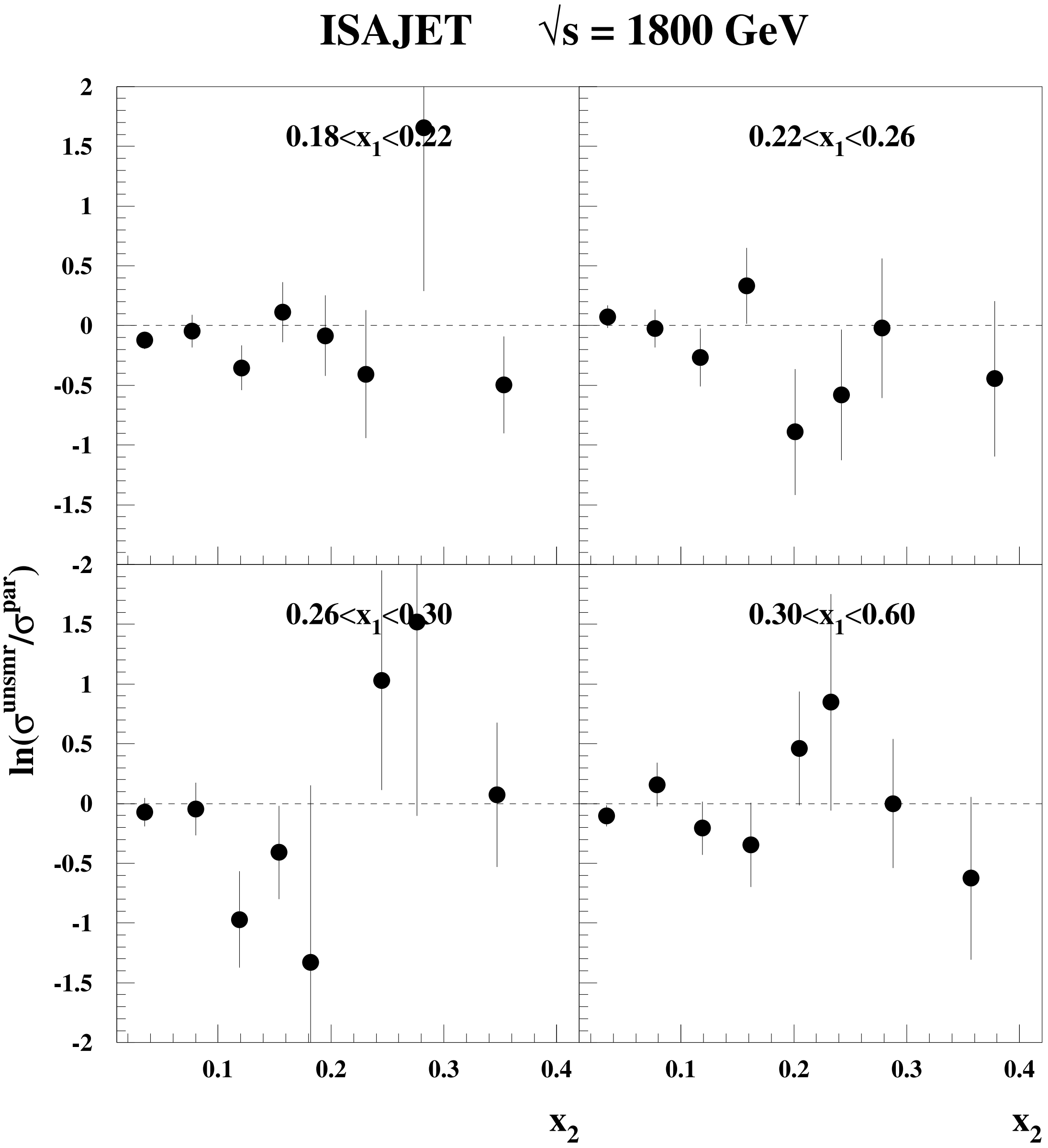

Figure 36: Unsmearing test using ISAJET Monte Carlo. The error bars represent statistical uncertainties.

6.7 Results on the Dijet Cross Section

The total dijet cross section, before and after unsmearing, corrected for experimental inefficiencies in both cases, is plotted in Figures 37 and 38, for the $\sqrt{s} = 1800$ and 630 samples, respectively. The cross section is plotted separately in each x_1-bin as a function of x_2. The errors shown are only statistical. The turn-over of the 630 GeV cross section at the lower values of x_1 and x_2 is an artifact of the $E_T > 20$ GeV and $\Delta\eta > 2$ requirements. These bins are not used when taking the ratio of the cross section at the two center-of-mass energies (see section 7.1).

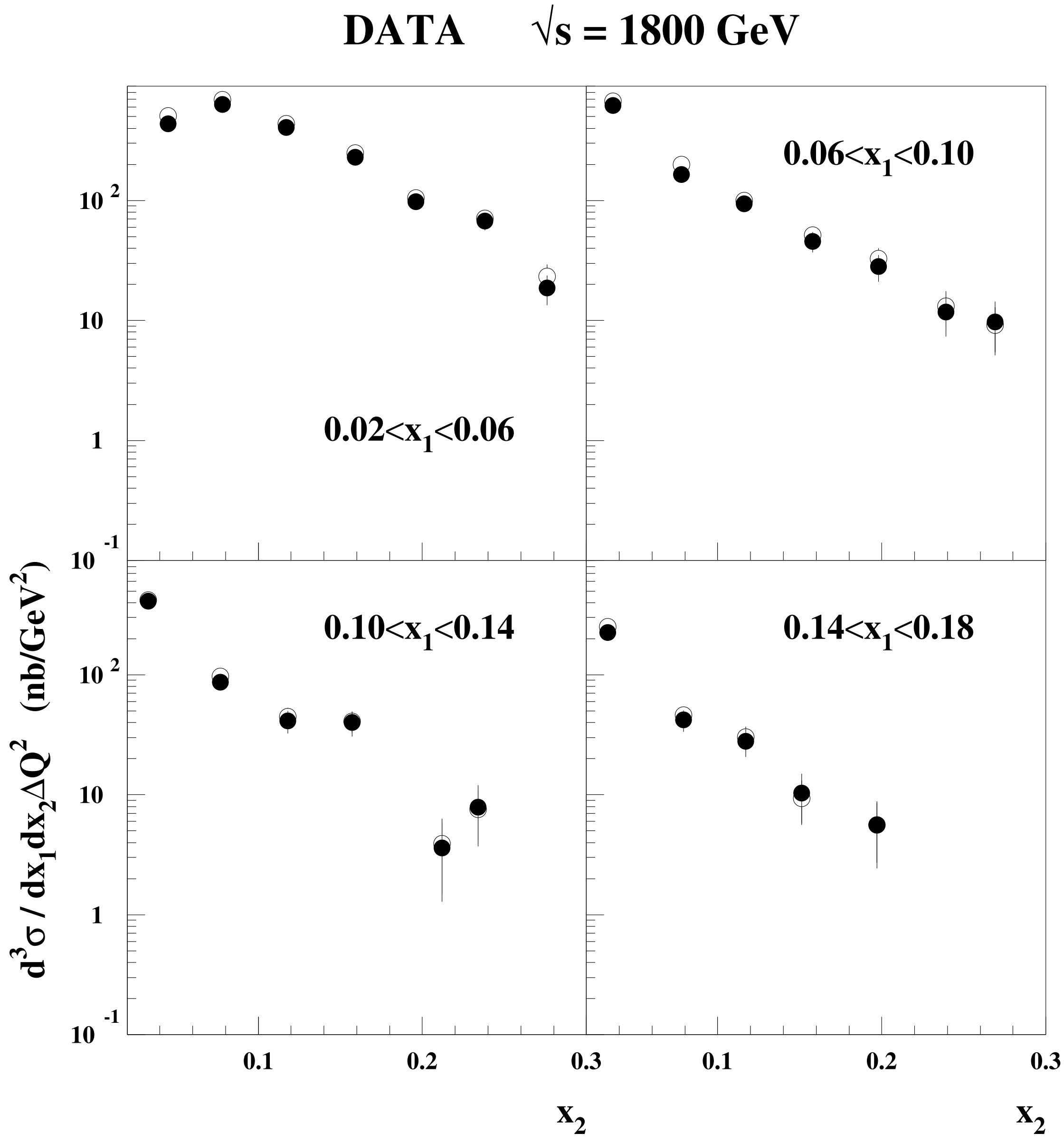

Figure 37: The dijet cross section before (open circles) and after (solid circles) unsmearing at $\sqrt{s} = 1800$ GeV. The error bars represent statistical uncertainties.

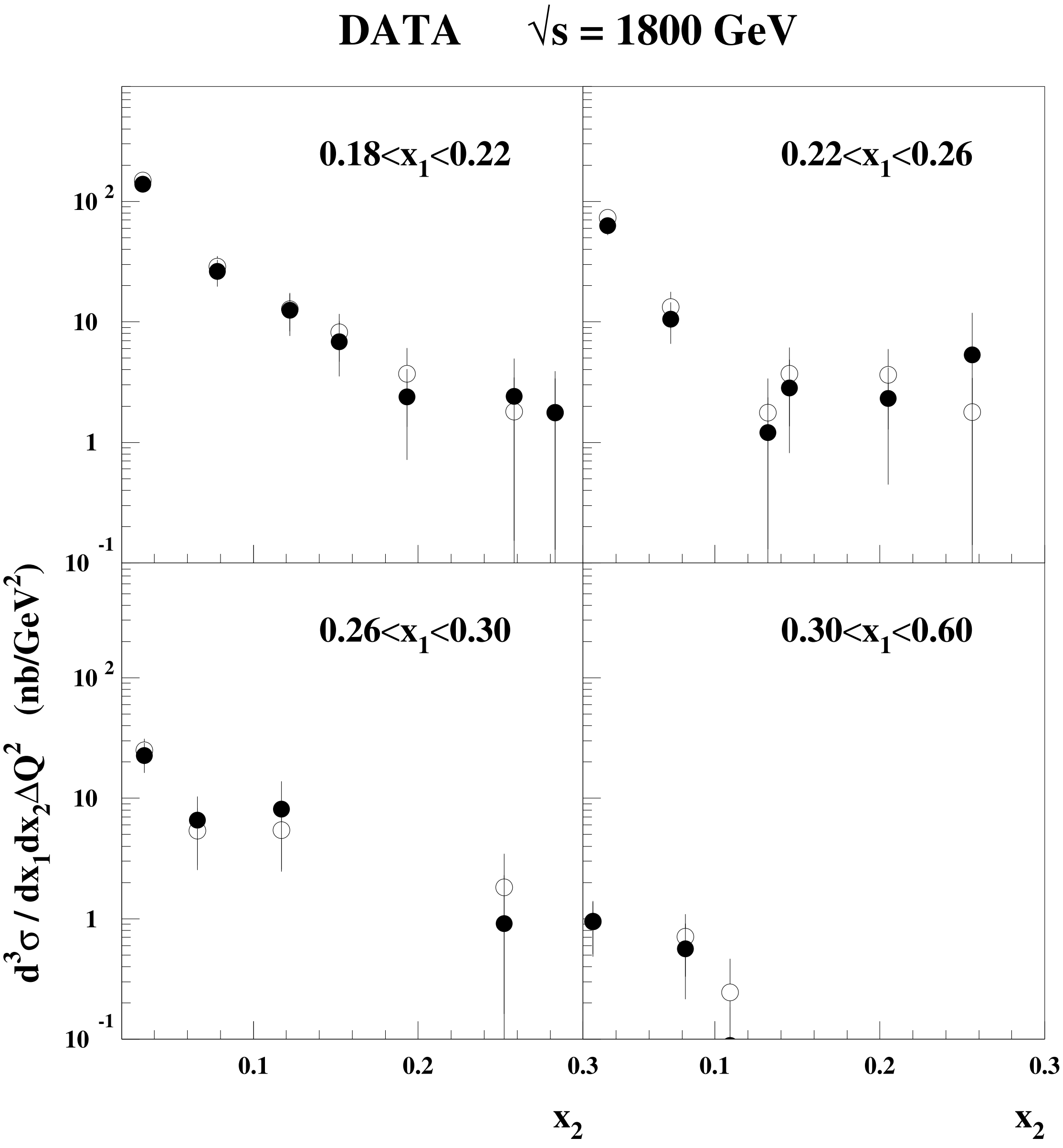

Figure 37: The dijet cross section before (open circles) and after (solid circles) unsmearing at $\sqrt{s} = 1800$ GeV. The error bars represent statistical uncertainties.

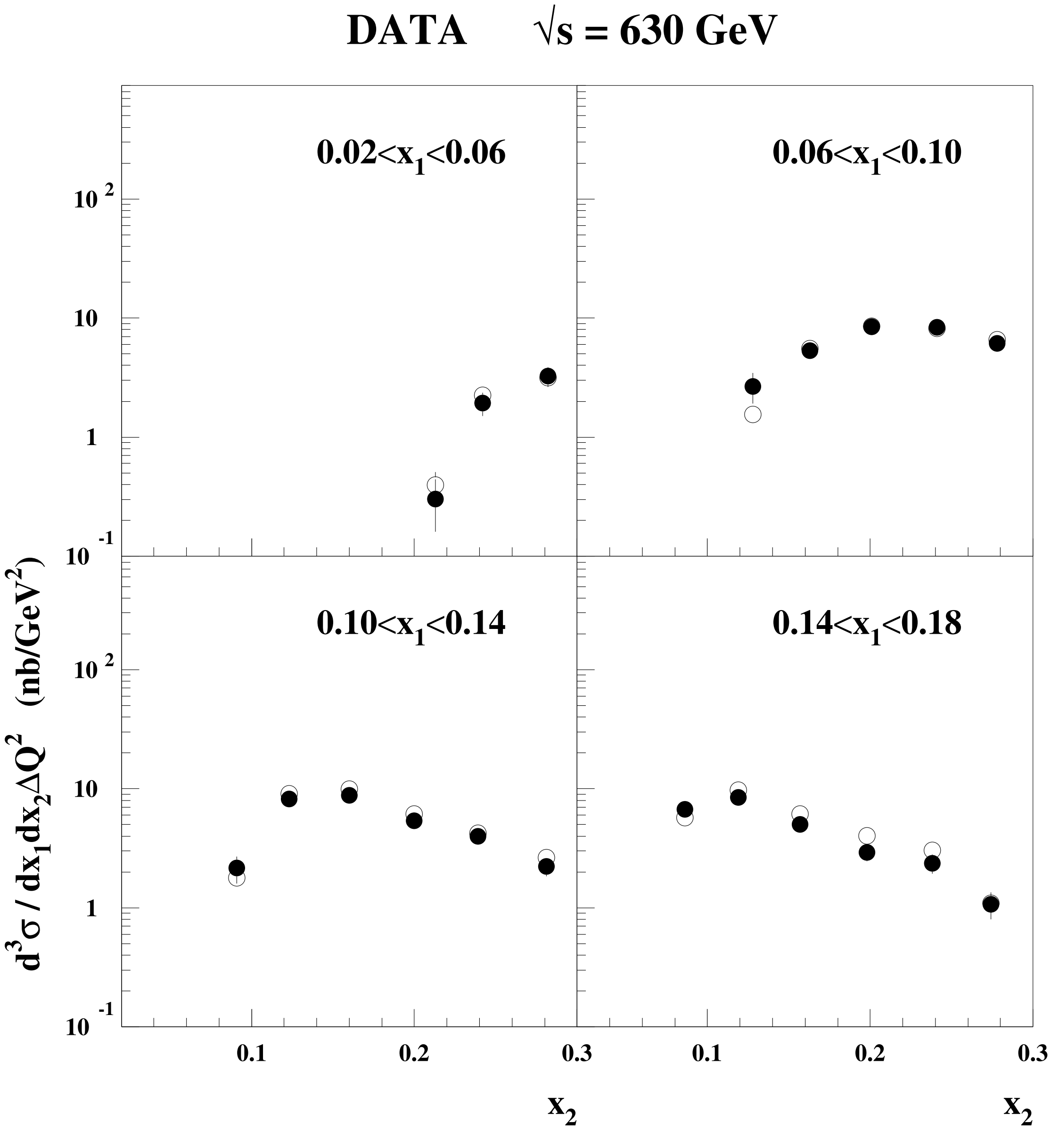

Figure 38: The dijet cross section before (open circles) and after (solid circles) unsmearing at $\sqrt{s} = 630$ GeV. The error bars represent statistical uncertainties.

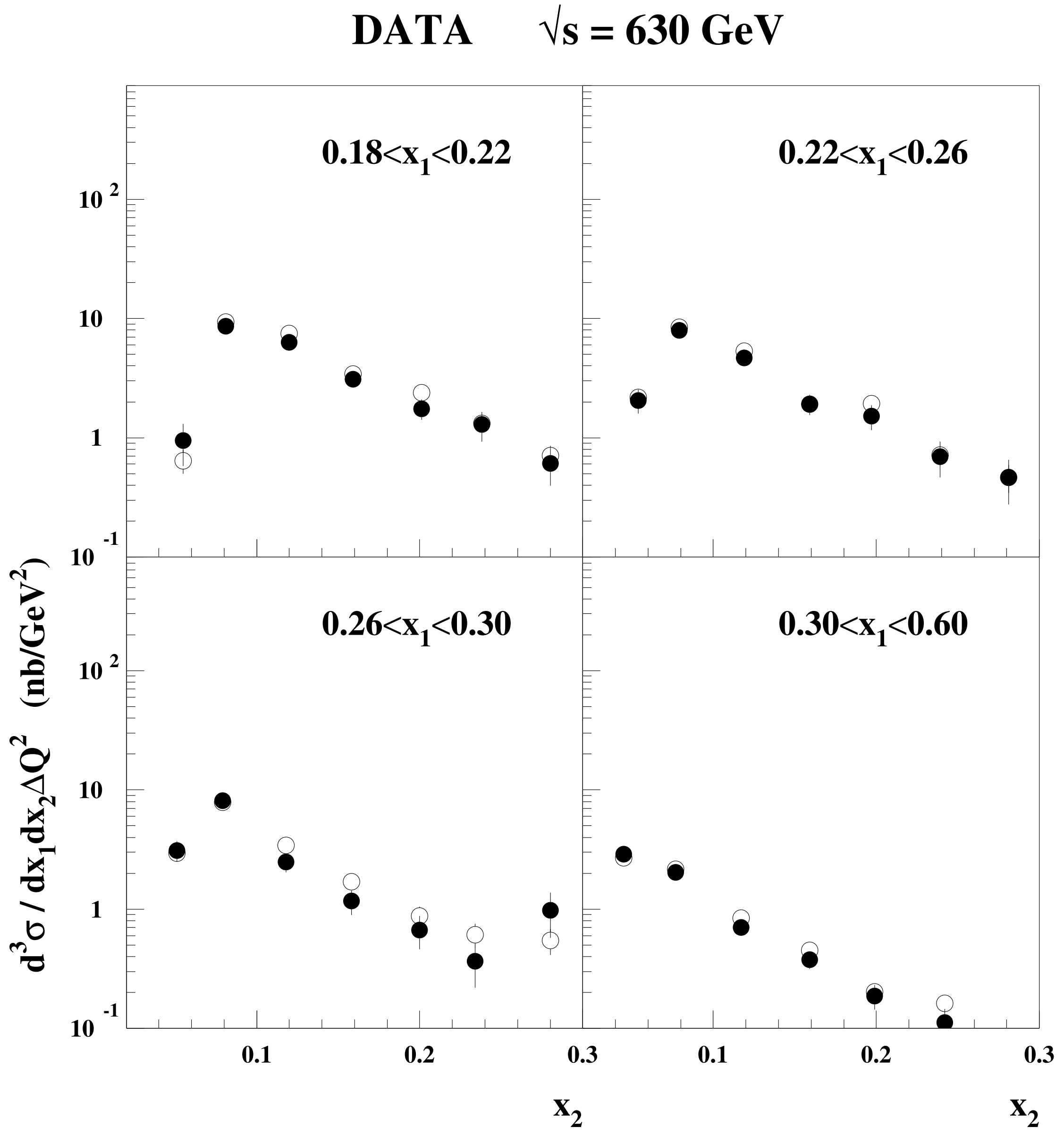

Figure 38: The dijet cross section before (open circles) and after (solid circles) unsmearing at $\sqrt{s} = 630$ GeV. The error bars represent statistical uncertainties.

7 The Ratio $\sigma_{1800}/\sigma_{630}$ and the BFKL Intercept

7.1 Selection of (x_1,x_2) Bins

The ratio of the dijet cross section at the two center-of-mass energies is taken in the (x_1,x_2,Q^2) bins that are not biased by the $E_T > 20$ GeV, $\Delta\eta > 2$ and $|\eta| < 3$ requirements.

The $E_T > 20$ GeV and $\Delta\eta > 2$ cuts can be translated into a requirement of minimum $x_1 \cdot x_2$ at each center-of-mass energy. Using equations (33) and (34) we find:

$$x_1 \cdot x_2 = \frac{4Q^2}{s} \cosh^2(\Delta\eta/2) \tag{46}$$

For $Q^2 > 400$ GeV^2 and $\Delta\eta > 2$ we find that $x_1 \cdot x_2$ must satisfy:

$$\text{at } \sqrt{s} = 1800 \text{ GeV}: \quad x_1 \cdot x_2 > 0.0012 \tag{47}$$
$$\text{at } \sqrt{s} = 630 \text{ GeV}: \quad x_1 \cdot x_2 > 0.0096 \tag{48}$$

The jet $|\eta| < 3$ requirement can be translated into a requirement of maximum $x_{1,2}$ at each center-of-mass energy. Using equations (33) and (34), for $E_{T_{1,2}} = 20$ GeV, we find that $x_{1,2}$ must satisfy:

$$\text{at } \sqrt{s} = 1800 \text{ GeV}: \quad x_{1,2} < 0.2237 \tag{49}$$
$$\text{at } \sqrt{s} = 630 \text{ GeV}: \quad x_{1,2} < 0.6392 \tag{50}$$

A total of ten bins, symmetric under the interchange of x_1 and x_2, satisfy both equations (48) and (49). The selected bins are given in Table 12.

i	x_1	j	x_2	minimum ($x_1 \cdot x_2$)
2	0.06 – 0.10	5	0.18 – 0.22	0.0108
3	0.10 – 0.14	4	0.14 – 0.18	0.0140
		5	0.18 – 0.22	0.0180
4	0.14 – 0.18	3	0.10 – 0.14	0.0140
		4	0.14 – 0.18	0.0196
		5	0.18 – 0.22	0.0252
5	0.18 – 0.22	2	0.06 – 0.10	0.0108
		3	0.10 – 0.14	0.0180
		4	0.14 – 0.18	0.0252
		5	0.18 – 0.22	0.0324

Table 12: *x_1 and x_2 bins used in the ratio of the cross section.*

7.2 Ratio of the Dijet Cross Section at $\sqrt{s} = 1800$ and 630 GeV

The mean values of N^{meas}, E_{T_1}, E_{T_2}, η_1, η_2, $\bar{\eta}$ and $\Delta\eta$ in each of the ten (x_1,x_2) bins used in the ratio are given in Tables 13 and 14, for the $\sqrt{s} = 1800$ and 630 GeV samples, respectively. The mean values of x_1, x_2 and Q^2 in each of the ten (x_1,x_2) bins are given in Tables 15 and 16, for the $\sqrt{s} = 1800$ and 630 GeV samples, respectively.

In each bin (i, j) of (x_1, x_2) the ratio

$$R_{bin} = \frac{\sigma(x_1, x_2, Q^2, s_{1800})}{\sigma(x_1, x_2, Q^2, s_{630})} \tag{51}$$

is calculated. The statistical uncertainty on the ratio in each bin is given by:

$$\Delta R_{bin} = R_{bin} \cdot \left[\frac{1}{N^{meas}_{1800}} + \frac{1}{M^{par}_{1800}} + \frac{1}{M^{smr}_{1800}} + \frac{1}{N^{meas}_{630}} + \frac{1}{M^{par}_{630}} + \frac{1}{M^{smr}_{630}} \right]^{\frac{1}{2}} . \tag{52}$$

It should be noted here that the above equation slightly overestimates the statistical error on the ratio, since M^{par} and M^{smr} are actually correlated: $M^{smr} = M^{par} - M^{out} + M^{in}$, where M^{out} is the number of events that left the particle–level (x_1,x_2,Q^2) bin due to smearing, and M^{in} is the number of events that migrated into the bin. The statistical uncertainty on the ratio in each bin is then equal to:

$$\Delta R_{bin} = R_{bin} \cdot \left[\frac{1}{N^{meas}_{1800}} + \frac{M^{in}_{1800} - M^{out}_{1800}}{M^{par}_{1800} \cdot (M^{smr}_{1800})^2} + \frac{M^{in}_{1800} + M^{out}_{1800}}{(M^{smr}_{1800})^2} + \frac{1}{N^{meas}_{630}} + \frac{M^{in}_{630} - M^{out}_{630}}{M^{par}_{630} \cdot (M^{smr}_{630})^2} + \frac{M^{in}_{630} + M^{out}_{630}}{(M^{smr}_{630})^2} \right]^{\frac{1}{2}} \tag{53}$$

In reality, however, the statistical error on the ratio is dominated by the number of data events measured in the bin at $\sqrt{s} = 1800$ GeV, N^{meas}_{1800}. Consequently, equations (52) and (53) give very similar results.

The values of the cross section at $\sqrt{s} = 1800$ and 630 GeV and the values of the ratio of the cross section at the two center-of-mass energies are given in Table 17. The uncertainties are statistical only. The ratios R_{bin}'s in the ten (x_1,x_2) bins are plotted in Fig. 39. The uncertainties shown in the plot are calculated according to Poisson statistics, for bins with less than ten events [22].

i	j	N^{meas}	E_{T_1}	E_{T_2}	η_1	η_2	$\bar{\eta}$	$\Delta\eta$
2	5	21.7	24.64	25.66	1.69	-2.63	-0.47	4.32
3	4	27.1	24.14	25.05	2.16	-2.42	-0.13	4.58
	5	2.6	22.73	25.00	2.20	-2.72	-0.26	4.92
	3	20.0	25.33	26.35	2.42	-2.08	0.17	4.49
4	4	6.2	28.91	26.34	2.27	-2.33	-0.03	4.59
	5	3.7	28.60	24.63	2.29	-2.67	-0.19	4.96
	2	19.0	25.43	26.08	2.64	-1.67	0.49	4.32
5	3	8.4	26.57	27.30	2.60	-2.08	0.26	4.68
	4	5.4	23.54	25.66	2.67	-2.38	0.15	5.05
	5	2.5	26.57	28.41	2.55	-2.50	0.03	5.04

Table 13: *Mean values of N^{meas}, E_{T_1}, E_{T_2}, η_1, η_2, $\bar{\eta}$ and $\Delta\eta$ for the $\sqrt{s}$ = 1800 GeV sample in each of the ten (x_1,x_2) bins used in the ratio.*

i	j	N^{meas}	E_{T_1}	E_{T_2}	η_1	η_2	$\bar{\eta}$	$\Delta\eta$
2	5	260.4	23.94	23.15	0.64	-1.60	-0.48	2.24
3	4	302.9	24.30	24.95	1.04	-1.31	-0.14	2.35
	5	188.1	24.97	25.69	1.04	-1.52	-0.24	2.57
	3	298.2	24.30	24.78	1.33	-1.02	0.15	2.35
4	4	187.6	26.17	25.94	1.27	-1.27	0.00	2.54
	5	123.2	26.23	25.50	1.27	-1.54	-0.13	2.81
	2	286.5	23.14	23.26	1.61	-0.69	0.46	2.29
5	3	228.2	25.91	25.33	1.51	-1.02	0.25	2.52
	4	104.7	25.29	25.11	1.55	-1.34	0.11	2.88
	5	72.7	25.94	26.37	1.54	-1.54	0.00	3.07

Table 14: *Mean values of N^{meas}, E_{T_1}, E_{T_2}, η_1, η_2, $\bar{\eta}$ and $\Delta\eta$ for the $\sqrt{s}$ = 630 GeV sample in each of the ten (x_1,x_2) bins used in the ratio.*

i	j	x_1	x_2	Q^2 (GeV^2)
2	5	0.076	0.198	629.5
3	4	0.117	0.157	603.0
	5	0.116	0.212	568.4
	3	0.158	0.117	665.2
4	4	0.156	0.151	765.8
	5	0.157	0.197	706.8
	2	0.199	0.078	660.4
5	3	0.200	0.122	721.0
	4	0.190	0.152	609.0
	5	0.190	0.193	752.5

Table 15: *Mean values of x_1, x_2 and Q^2 for the $\sqrt{s} = 1800$ GeV sample in each of the ten (x_1,x_2) bins used in the ratio.*

i	j	x_1	x_2	Q^2 (GeV^2)
2	5	0.080	0.201	553.1
3	4	0.119	0.160	603.7
	5	0.121	0.200	641.1
	3	0.159	0.119	601.7
4	4	0.157	0.157	676.7
	5	0.156	0.198	666.5
	2	0.201	0.081	537.4
5	3	0.199	0.120	656.1
	4	0.197	0.159	637.1
	5	0.198	0.201	680.8

Table 16: *Mean values of x_1, x_2 and Q^2 for the $\sqrt{s} = 630$ GeV sample in each of the ten (x_1,x_2) bins used in the ratio.*

i	j	$\sigma_{1800} \pm \Delta\sigma$	$\sigma_{630} \pm \Delta\sigma$	$R_{bin} \pm \Delta R_{bin}$
2	5	28.063 ± 6.927	8.407 ± 0.868	3.338 ± 0.893
3	4	40.087 ± 9.482	8.765 ± 0.853	4.573 ± 1.170
	5	3.591 ± 2.309	5.409 ± 0.639	0.664 ± 0.434
	3	27.949 ± 7.269	8.425 ± 0.816	3.317 ± 0.921
4	4	10.375 ± 4.585	5.034 ± 0.589	2.061 ± 0.942
	5	5.629 ± 3.180	2.916 ± 0.454	1.931 ± 1.131
	2	26.257 ± 6.630	8.632 ± 0.893	3.042 ± 0.830
5	3	12.538 ± 4.873	6.300 ± 0.680	1.990 ± 0.803
	4	6.830 ± 3.320	3.094 ± 0.448	2.208 ± 1.120
	5	2.386 ± 1.672	1.749 ± 0.340	1.364 ± 0.992

Table 17: *The unsmeared dijet cross section at* $\sqrt{s} = 1800$ *and* 630 *GeV and the ratio* R_{bin} *in each of the ten* (x_1,x_2) *bins. The uncertainties are statistical only.*

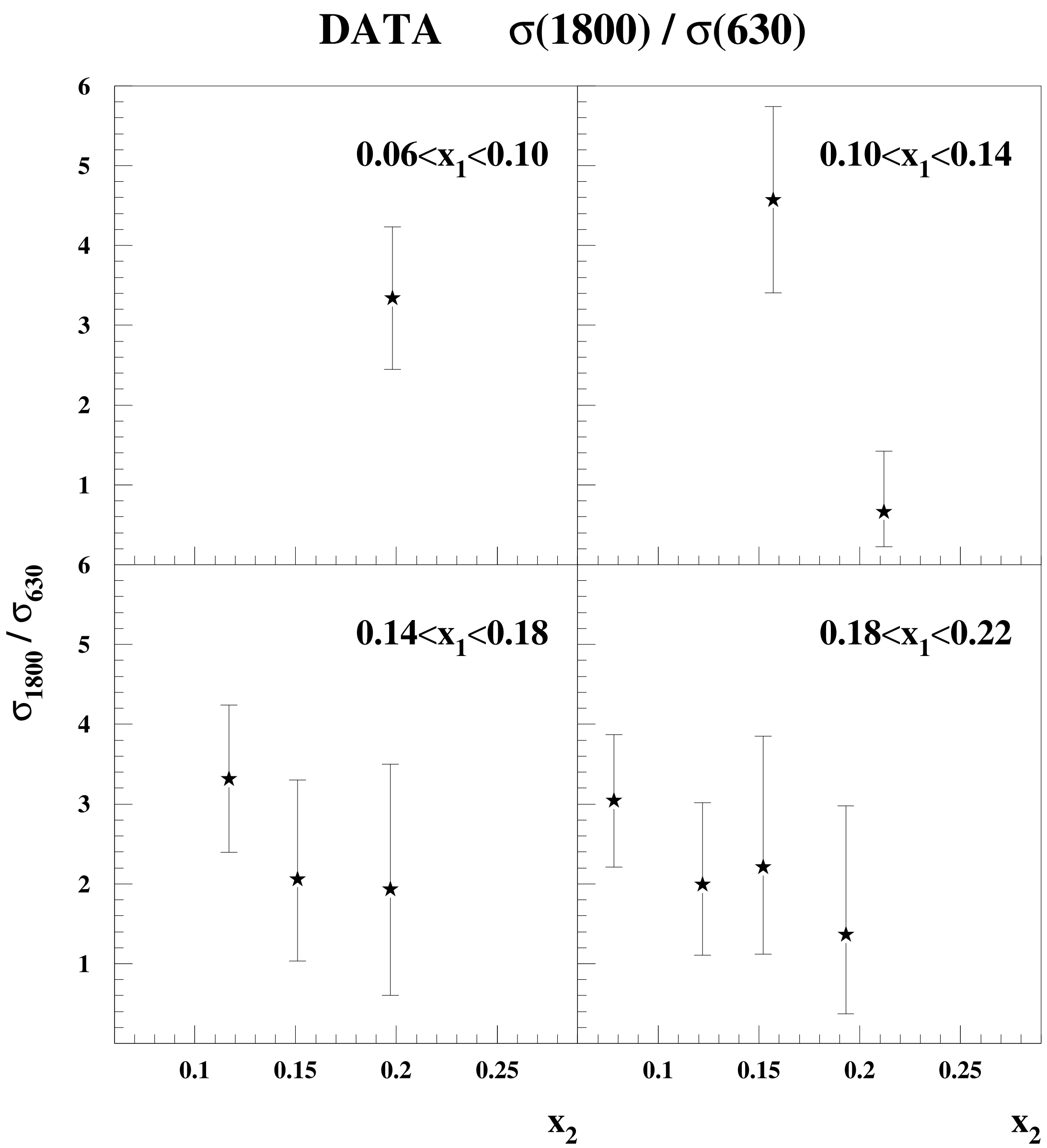

Figure 39: The ratio of the dijet cross section at $\sqrt{s} = 1800$ and 630 GeV. The error bars represent statistical uncertainties (calculated according to Poisson statistics for bins with less than ten events).

In order to find the average ratio, we fit the 1800 and 630 GeV cross sections simultaneously using a maximum likelihood fit based on Poisson statistics. In particular, we use the χ^2_λ statistic [23]. For the purposes of determining the best fit, minimizing χ^2_λ is equivalent to maximizing the Poisson likelihood. However, in addition to determining the best fit, the χ^2_λ offers information on the goodness of the fit.

Fitting the 1800 and 630 GeV cross sections simultaneously results in twenty bins fit together. The χ_λ is equal to:

$$\chi_\lambda = 2 \cdot \sum_{i=1}^{20} \left[\sigma_{exp}(i) - \sigma_{obs}(i) + \sigma_{obs}(i) \cdot \ln(\sigma_{obs}(i)/\sigma_{exp}(i))\right], \tag{54}$$

where $\sigma_{obs}(i)$ and $\sigma_{obs}(i)$ are the observed and expected cross section in the i-th bin, respectively. The expected cross section in each bin can take any value, completely independent of its value in any other (x_1,x_2) bin:

$$\sigma_{exp}(i) = par(i) \qquad i = 1, ..., 10 \qquad \text{at } 630 \text{ GeV} \tag{55}$$

$$\sigma_{exp}(i) = par(i-10) \cdot par(11) \qquad i = 11, ..., 20 \qquad \text{at } 1800 \text{ GeV} \tag{56}$$

where $par(1, ..., 11)$ is a vector of 11 free parameters in the fit. The 11-th parameter represents the ratio of the 1800 and 630 GeV cross sections. The results are:

$par(11) = 2.8$

$\chi^2_\lambda = 8.5$ for 9 degrees of freedom.

The statistical error on the average ratio is calculated with a "toy" Monte Carlo. The statistical variations of the 630 and 1800 GeV cross sections in each (x_1,x_2) bin are used as inputs in random number generators. The outputs are used as the observed cross sections, which are then fitted in the same way as the nominal cross sections are. The procedure is repeated 10,000 times and the output of the fit for the 11-th parameter is saved each time. This results in a gaussian distribution of the ratio of the cross sections around the nominal value of the ratio. The above distribution is fitted and the error of this fit is used as the statistical uncertainty on the ratio.

The results are summarized in Table 18.

$< R > \pm < \Delta R >$
2.8 ± 0.3(stat)

Table 18: *Mean value for the ratio of the dijet cross section at* $\sqrt{s} = 1800$ *and* 630 *GeV. The uncertainty is statistical only.*

7.3 Extraction of the BFKL Intercept

A value for the BFKL intercept, α_{BFKL}, is extracted from the ratio of the cross section in each (x_1,x_2,Q^2) bin, using equation (17):

$$\alpha_{\mathrm{BFKL}_{bin}} = 1 + (\Delta\eta_{1800} - \Delta\eta_{630})^{-1} \cdot \ln\left\{ R_{bin} \cdot \sqrt{\frac{\Delta\eta_{1800}}{\Delta\eta_{630}}} \right\} , \tag{57}$$

where $\Delta\eta_{1800}$ and $\Delta\eta_{630}$ are the average values for the rapidity intervals in each bin at $\sqrt{s} = 1800$ and 630 GeV, respectively.

The statistical uncertainty on the value of α_{BFKL} in each bin is given by:

$$\Delta\alpha_{\mathrm{BFKL}_{bin}} = (\Delta\eta_{1800} - \Delta\eta_{630})^{-1} \cdot \Delta(\ln R_{bin}) , \tag{58}$$

where:

$$\begin{aligned} \Delta(\ln R_{bin}) &= \frac{1}{R_{bin}} \cdot \Delta R_{bin} \\ &= \sqrt{\left(\frac{\Delta\sigma_{bin}}{\sigma_{bin}}\right)^2_{1800} + \left(\frac{\Delta\sigma_{bin}}{\sigma_{bin}}\right)^2_{630}} \\ &= \left[\frac{1}{N^{meas}_{1800}} + \frac{1}{M^{par}_{1800}} + \frac{1}{M^{smr}_{1800}} + \frac{1}{N^{meas}_{630}} + \frac{1}{M^{par}_{630}} + \frac{1}{M^{smr}_{630}}\right]^{\frac{1}{2}} . \end{aligned} \tag{59}$$

Then:

$$\Delta\alpha_{\mathrm{BFKL}_{bin}} = (\Delta\eta_{1800} - \Delta\eta_{630})^{-1} \cdot \left[\frac{1}{N^{meas}_{1800}} + \frac{1}{M^{par}_{1800}} + \frac{1}{M^{smr}_{1800}} + \frac{1}{N^{meas}_{630}} + \frac{1}{M^{par}_{630}} + \frac{1}{M^{smr}_{630}}\right]^{\frac{1}{2}} . \tag{60}$$

The values of α_{BFKL} in the ten (x_1,x_2) bins are plotted in Fig. 40 and listed in Table 19 (the values of the ratio are also listed for completeness).

The mean value of α_{BFKL} is calculated by taking the error weighted average:

$$< \alpha_{\mathrm{BFKL}} >= \frac{\sum_{bin} \frac{\alpha_{\mathrm{BFKL}_{bin}}}{(\Delta\alpha_{\mathrm{BFKL}_{bin}})^2}}{\sum_{bin} \frac{1}{(\Delta\alpha_{\mathrm{BFKL}_{bin}})^2}} . \tag{61}$$

The mean statistical uncertainty on α_{BFKL} is given by:

$$< \Delta\alpha_{\mathrm{BFKL}} >= \left[\frac{1}{\sum_{bin} \frac{1}{(\Delta\alpha_{\mathrm{BFKL}_{bin}})^2}}\right]^{\frac{1}{2}} . \tag{62}$$

The results are given in Table 20.

A $\chi^2/d.o.f.$ is calculated, in order to test the deviation of the intercept in each (x_1,x_2,Q^2) bin from the mean value. It is equal to 1.05.

i	j	$R_{bin} \pm \Delta R_{bin}$	$\alpha_{\mathrm{BFKL}_{bin}} \pm \Delta\alpha_{\mathrm{BFKL}_{bin}}$
2	5	3.338 ± 0.893	1.738 ± 0.129
3	4	4.573 ± 1.170	1.830 ± 0.114
	5	0.664 ± 0.434	0.964 ± 0.278
	3	3.317 ± 0.921	1.711 ± 0.130
4	4	2.061 ± 0.942	1.496 ± 0.222
	5	1.931 ± 1.131	1.438 ± 0.273
	2	3.042 ± 0.830	1.706 ± 0.135
5	3	1.990 ± 0.803	1.462 ± 0.187
	4	2.208 ± 1.120	1.495 ± 0.234
	5	1.364 ± 0.992	1.283 ± 0.368

Table 19: *The ratio R_{bin} and the BFKL intercept $\alpha_{\mathrm{BFKL}_{bin}}$ in each of the ten (x_1,x_2) bins. The uncertainties are statistical only.*

$< \alpha_{\mathrm{BFKL}} > \pm < \Delta\alpha_{\mathrm{BFKL}} >$
$1.65 \pm 0.05(\mathrm{stat})$

Table 20: *Mean value for the BFKL intercept. The uncertainty is statistical only.*

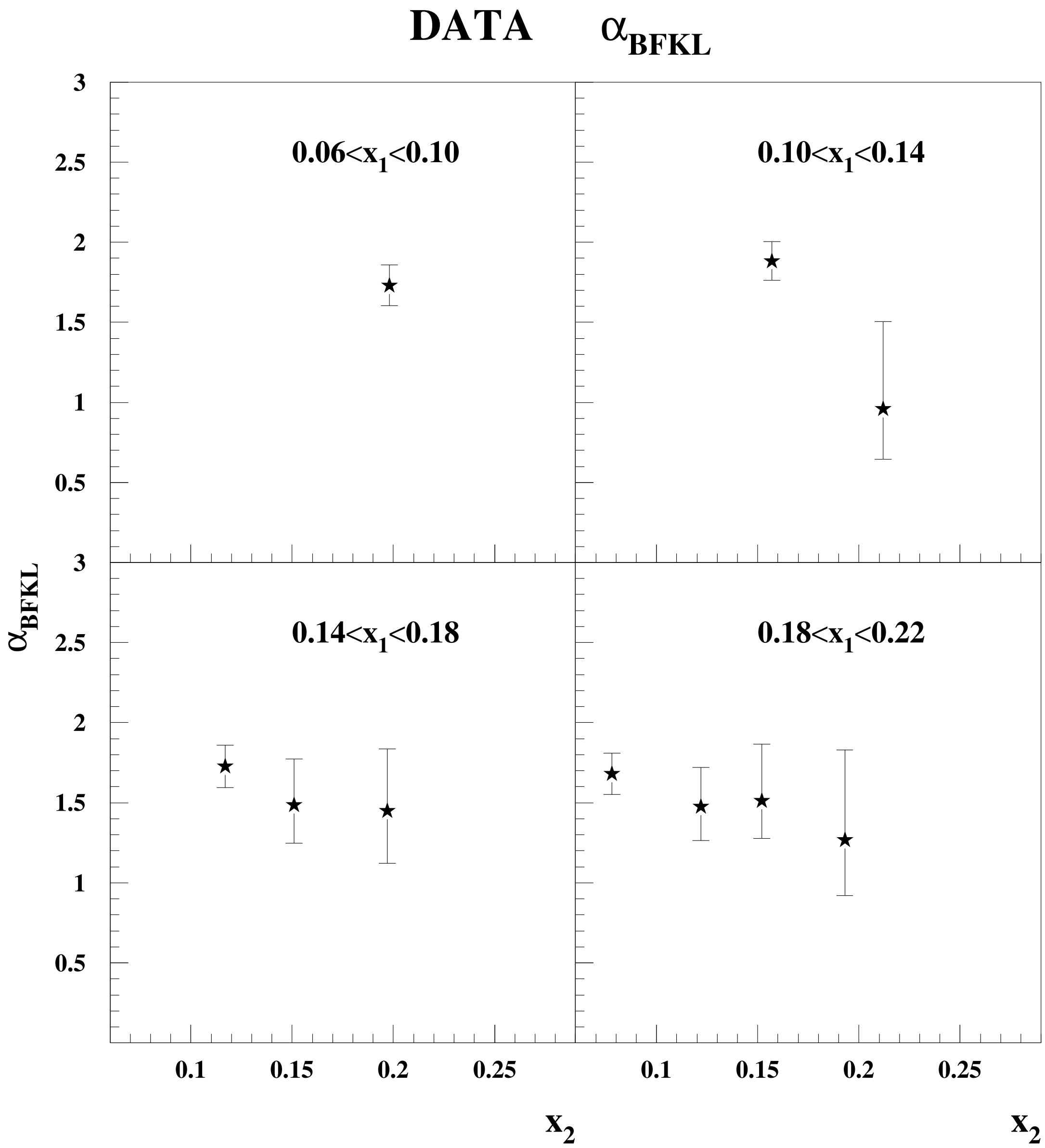

Figure 40: The value of the BFKL intercept as extracted from the ratio of the dijet cross section at $\sqrt{s}$ = 1800 and 630 GeV in the ten (x_1,x_2) bins. The error bars represent statistical uncertainties (calculated according to Poisson statistics for bins with less than ten events).

7.4 Systematic Uncertainty on the Ratio of the Cross Section and the BFKL Intercept

The main sources of systematic uncertainty on the ratio of the dijet cross section at the two center-of-mass energies and on the value of the BFKL intercept are considered in the following paragraphs. For each one of them, we decide on possible error correlations between the cross sections at the two energies. In the last paragraph, we calculate the total systematic uncertainty on the ratio and the BFKL intercept.

7.4.1 Jet Energy Scale

When considering the uncertaities of the jet energy scale determination and their effect on the cross section ratio and on α_{BFKL}, we need to decide on the correlations of the uncertainties between the two center-of-mass energies. The transverse energy of the jets at the two energies in each (x_1,x_2) bin is very similar, as can be seen in Tables 13 and 14. Therefore, the jet energy scale error correlations between the two energies are actually correlations between the different jet rapidities at which the two cross sections are measured. Thus, when taking the ratio of the cross sections at $\sqrt{s} = 1800$ and 630 GeV, we consider as uncorrelated the errors on σ_{1800} and σ_{630} due to the uncertainties on the cryostat factor, the η-dependence, the fitting error on the showering correction, and the 2% uncertainty on the showering correction due to the data–Monte Carlo comparison [10]. In addition, the energy scale errors that are of statistical nature are considered as uncorrelated. These include the statistical errors on the noise suppression and the offset. On the contrary, the systematic errors on the jet energy scale which are the same at the two center-of-mass energies and independent of the jet rapidity are considered as correlated. These include the systematic uncertainty on the noise suppression and the residual bias. The systematic uncertainty on the showering correction due to the variation of the jet limit is considered as correlated since the jets at both $\sqrt{s}$ are at the low end of the energy range in each rapidity region. The k_T uncertainty is also considered as correlated, since it dependes solely on the jet E_T, which is the same at the two energies. Finally, the uncertainty on the fit of the jet response, which corresponds to average energies not higher than 170 GeV, is *not* one of the major sources of uncertainty in the ICR and forward region, and is considered for simplicity as fully correlated.

7.4.2 Jet Energy Resolutions

The uncertainty in the measurement of the jet E_T resolutions (see Appendix A) consists of two parts: the fitting error, and the systematic error due to the assymetry method. The latter is determined from the difference between the resolutions extracted using the assymetry method and the resolutions extracted by direct comparison of the particle- to calorimeter-level jet transverse energies in Monte Carlo events. The difference is within 1% for $E_T > 30$ GeV (where we have mesurement of the resolutions at 1800 GeV) [24]. The fitting error is considered uncorrelated between the 1800 and 630 GeV cross sections (i.e., between different jet rapidities), whereas the systematic error of the method is considered as correlated.

An additional uncertainty is considered regarding the extrapolation of the resolutions in the low E_T region and the comparison of the $\sqrt{s} = 630$ GeV resolutions to the ones at 1800 GeV. At 1800 GeV, we measure the resolutions for $E_T > 30$ GeV. At 630 GeV, the measurement covers the E_T region of 20–80 GeV at $|\eta| < 0.8$, and 20–40 GeV at $0.8 < |\eta| < 2$. Since limited statistics prohibits the measurement of the 630 GeV resolutions in sufficiently small η-bins, we use the 1800 resolutions at both c.m. energies. At E_T's lower than 30 GeV at both c.m. energies, we rely on the extrapolation of the 1800 GeV resolutions.

In the region of overlap between the resolution measurements at the two c.m. energies, the 630 GeV resolutions are smaller than the 1800 ones by $\sim$1%. In the region $0.8 < |\eta| < 2$ and for $E_T = 25$ GeV (which is the average E_T of the jets in this analysis), the 630 GeV resolutions are lower than the 1800 GeV extrapolation by $\sim$3%. Combining the 630 GeV points scaled upward by 1% with the 1800 GeV points, we can constrain the fit at low E_T's. The extrapolated 1800 GeV fit is then $\sim$2% higher than the constrained fit, and the constrained fit itself is an additional $\sim$1% higher than the 630 GeV points. In other words, we are probably overestimating the resolutions at both c.m. energies by 2% due to the extrapolation of the fit in low E_T region, and an additional 1% at $\sqrt{s} = 630$ GeV due to the difference between the 1800 and 630 GeV resolutions. Thus, we consider a downward correlated systematic uncertainty, where the 1800(630) GeV cross section is unsmeared using the extrapolation of the 1800 GeV resolutions scaled down by 2(3)%.

7.4.3 Input PDF in the Monte Carlo

In order to account for the dependence of the cross section unsmearing method on the input PDF in the Monte Carlo, we repeat the unsmearing procedure using a different input PDF, as explained in paragaph 6.6. We choose MRSA$'$ (as opposed to CTEQ4M in the nominal unsmearing). The question of error correlations is irrelevant for this systematic change.

7.4.4 Luminosity Uncertainty

The overall normalization error on the luminosity determination causes a normalization shift on the dijet cross section and thus, a systematic error on the ratio and the intercept. The luminosity error is equal to 5.3% at $\sqrt{s} = 1800$ GeV and 3.2% at $\sqrt{s} = 630$ GeV. The larger sources of the above uncertainties are systematic and correlated between the two center-of-mass energies [25]. Therefore, we consider the overall normalization error as correlated.

7.4.5 Merged & Split Jets

The jet algorithm treats overlapping jet cones as following: if the energy shared between the two cones is higher than 50% of the lower of the two jet energies, the two cones are merged into one jet; otherwise, they are split into two jets. Since this analysis consists of an inclusive measurement, events with merged and split jets are included in the cross section. However, in order to exclude the possibility that non-isolated jets may cause systematic biases in the ratio of the cross section, we examine the fraction of the isolated versus merged and split jets in the two samples. In the $\sqrt{s} = 1800$ GeV sample, 62% of the jets with $E_T > 20$ GeV are isolated. In the $\sqrt{s} = 630$ GeV sample, the equivalent fraction is 68%. Since the fractions are of the same order at the two center-of-mass energies, we do not consider a systematic bias on the ratio of the cross sections.

7.4.6 Total Systematic Uncertainties

We first measure the uncorrelated systematic errors due to the jet energy scale and the jet E_T resolutions on the 1800 and 630 GeV cross sections in each (x_1,x_2) bin: $(\Delta\sigma_{bin})^{cfx,uncorr}$ and $(\Delta\sigma_{bin})^{res,uncorr}$, respectively. In doing so, we symmetrize the systematic uncertainties due to the jet energy scale and the jet E_T resolutions, i.e., we take the average between their high and low variations.

The uncorrelated systematic errors on the average ratio, due to the jet energy scale and the jet E_T resolutions, are calculated with a "toy" Monte Carlo, as described in section 7.2.

The uncorrelated systematic errors on the average intercept, due to the jet energy scale and the jet E_T resolutions, are calculated using differential error propagation. The uncorrelated systematic errors on the intercept in each bin are equal to (the BFKL subscript is omitted from α_{BFKL} for simplicity of the formulae):

$$(\Delta\alpha_{bin})^{cfx,uncorr} = (\Delta\eta_{1800} - \Delta\eta_{630})^{-1} \cdot (\Delta(\ln R_{bin}))^{cfx,uncorr}\,, \tag{63}$$

$$(\Delta\alpha_{bin})^{res,uncorr} = (\Delta\eta_{1800} - \Delta\eta_{630})^{-1} \cdot (\Delta(\ln R_{bin}))^{res,uncorr}\,, \tag{64}$$

where

$$\begin{aligned}(\Delta(\ln R_{bin}))^{cfx,uncorr} &= \frac{1}{R_{bin}} \cdot (\Delta R_{bin})^{cfx,uncorr} \\ &= \sqrt{\left(\frac{(\Delta\sigma_{bin})^{cfx,uncorr}}{\sigma_{bin}}\right)^2_{1800} + \left(\frac{(\Delta\sigma_{bin})^{cfx,uncorr}}{\sigma_{bin}}\right)^2_{630}}\end{aligned} \tag{65}$$

$$\begin{aligned}(\Delta(\ln R_{bin}))^{res,uncorr} &= \frac{1}{R_{bin}} \cdot (\Delta R_{bin})^{res,uncorr} \\ &= \sqrt{\left(\frac{(\Delta\sigma_{bin})^{res,uncorr}}{\sigma_{bin}}\right)^2_{1800} + \left(\frac{(\Delta\sigma_{bin})^{res,uncorr}}{\sigma_{bin}}\right)^2_{630}}\end{aligned} \tag{66}$$

The total uncorrelated error on the BFKL intercept in each bin is equal to:

$$(\Delta\alpha_{bin})^{tot,uncorr} = \sqrt{((\Delta\alpha_{bin})^{stat})^2 + ((\Delta\alpha_{bin})^{cfx,uncorr})^2 + ((\Delta\alpha_{bin})^{res,uncorr})^2} \tag{67}$$

where $(\Delta\alpha_{bin})^{stat}$ is given by eq. 60.

The mean BFKL intercept, $< \alpha_{\mathrm{BFKL}} >$, weighted by the total uncorrelated uncertainty on each α_{bin}, is:

$$< \alpha_{\mathrm{BFKL}} > = \frac{\sum_{bin} \frac{\alpha_{bin}}{(\Delta\alpha_{bin}^{tot,uncorr})^2}}{\sum_{bin} \frac{1}{(\Delta\alpha_{bin}^{tot,uncorr})^2}}\,. \tag{68}$$

The mean uncorrelated systematic due to energy scale, and uncorrelated systematic due to resolutions, uncertainties on $< \alpha_{\rm BFKL} >$ are:

$$< \Delta\alpha_{\rm BFKL}^{cfx,uncorr} >= \left[\frac{1}{\sum_{bin} \frac{1}{(\Delta\alpha_{bin}^{cfx,uncorr})^2}} \right]^{\frac{1}{2}} , \tag{69}$$

$$< \Delta\alpha_{\rm BFKL}^{res,uncorr} >= \left[\frac{1}{\sum_{bin} \frac{1}{(\Delta\alpha_{bin}^{res,uncorr})^2}} \right]^{\frac{1}{2}} . \tag{70}$$

Due to the correlated systematic uncertainties, the 1800 and 630 GeV cross sections will both fluctuate high (or low). Therefore, we can calculate the ratios $< R^{high,corr} >$ and $< R^{low,corr} >$ from the high and the low 1800 and 630 GeV cross sections. The high and low correlated uncertainties are then equal to the differences of $< R^{high,corr} >$ and $< R^{low,corr} >$ from the nominal $< R >$ value. A similar procedure is followed for the BFKL intercept.

The percentage deviation from the nominal values of the ratio of the cross section and the BFKL intercept for each systematic change are given in Table 21.

Systematic Change	% change on $< R >$	% change on $< \alpha_{\rm BFKL} >$
Jet Energy Scale, Uncorrelated	± 7	± 1.8
Jet Energy Scale, Correlated, High	-3	-1.8
Jet Energy Scale, Correlated, Low	$+2$	$+0.6$
Jet Energy Resolutions, Uncorrelated	± 6	± 1.8
Jet Energy Resolutions, Closure, High	0	0.0
Jet Energy Resolutions, Closure, Low	-1	0.0
Jet Energy Resolutions, Correlated Low	-4	-1.0
Input PDF in MC	-1	0.0
Luminosity, Correlated, High	$+2$	$+0.6$
Luminosity, Correlated, Low	-2	-0.6

Table 21: *Percentage deviations from the nominal $< R >$ and $< \alpha_{\rm BFKL} >$ for each systematic change.*

Adding all systematic errors in quadrature yields an $\sim$11% total systematic uncertainty on the ratio of the cross sections, and a $\sim$3% total systematic uncertainty on the BFKL intercept. The final results are shown in Tables 22 and 23.

$< R > \pm < \Delta R >$
$2.8 \pm 0.3(\text{stat}) \pm 0.3(\text{syst})$

Table 22: *Mean value for the ratio of the dijet cross section at* $\sqrt{s} = 1800$ *and* 630 *GeV. The uncertainties are statistical, and total systematic.*

$< \alpha_{\text{BFKL}} > \pm < \Delta\alpha_{\text{BFKL}} >$
$1.65 \pm 0.05(\text{stat}) \pm 0.05(\text{syst})$

Table 23: *Mean value for the BFKL intercept. The uncertainties are statistical, and total systematic.*

8 Discussion

Several theoretical predictions for the ratio of the dijet cross section have been calculated in [26]. In LO QCD, the $2 \to 2$ subprocess matrix elements (for gg, qg and qq interactions) are functions only of the rapidity interval, $\Delta\eta$. In the asymptotic limit where $\Delta\eta$ is very large, the partonic cross section becomes independent of $\Delta\eta$; hence, the ratio of the cross sections becomes equal to unity:

$$R_{LO,\,asympt} = 1.0$$

For the rapidity intervals accessible to this analysis, however, there remains a dependence on $\Delta\eta$, which causes the ratio of the cross sections to deviate from unity. For $\Delta\eta_{630} = 2.56$, the ratio of the total dijet cross sections at $\sqrt{s} = 1800$ and 630 GeV is equal to:

$$R_{LO,\,exact} = 1.2$$

The ratio is insensitive to the choice of parton distributions, and has only a very weak dependence on the choice of the scale μ.

The analytic BFKL (in LLA) predictions for the intercept and the ratio can be calculated from equations (2) and (17), respectively. For $\alpha_s(Q = 20\,\text{GeV}) = 0.17$ [26], eq. (2) yields:

$$\alpha_{BFKL,\,LLA} = 1.45$$

For $\Delta\eta_{1800} = 4.70$ and $\Delta\eta_{630} = 2.56$, eq. (17) yields:

$$R_{BFKL,\,LLA} = 1.9$$

It should be noted again, however, that the leading log approximation is too simplified, and that exact quantitative BFKL predictions are not yet possible (see also section 1).

The HERWIG sample that we used in the data cross section unsmearing procedure can also be used to derive a value for the ratio of the dijet cross section at the two center-of-mass energies. We use the same (x_1,x_2,Q^2) bins as in the data ratio (see Fig. 41). At the particle level we find:

$$R_{HERWIG} = 1.6 \pm 0.1\ (\text{stat}),$$

a result which lies between LO QCD and LLA BFKL. As a reminder, HERWIG calculates the exact $2 \to 2$ QCD subprocess, including initial– and final–state QCD radiation, color coherence effects, and azimuthal correlations both within and between jets [20].

In pure DGLAP evolution, the radiated gluons are strongly ordered in k_T (soft gluons). At intermediate and high values of Q^2, and not very small values of Bjorken x, DGLAP sums the large logarithms of the form $\alpha_s \ln Q^2$.

At small values of x but still intermediate values of Q^2, the logarithms of $1/x$ become of comparable size to the logarithms of Q^2. In this region, the DGLAP equation evolves into the Double Leading Logarithmic Approximation (DLLA), which sums terms of the form $\alpha_s^n \ln^n Q^2 \ln^n(1/x)$. Note that the leading logarithms of $1/x$ are common in DLLA and BFKL resummation. However, in DLLA they should be accompanied by the leading logarithms of Q^2. The DLLA breaks down at low values of Q^2, when the $\ln Q^2$ become small but the $\ln(1/x)$ are still large and need to be resummed. This is accomplished by the BFKL evolution.

In HERWIG, however, the gluons are ordered by their emission angle (instead of k_T, as in regular DGLAP evolution). This introduces an additional term of soft $\ln(1/x)$ corrections in the HERWIG gluon distribution. The resummation, Angular Ordering (AO) including, is now of terms $\alpha_s^n \ln^{n-1} Q^2 \ln^n(1/x)$, i.e. one term closer to the BFKL resummation.

The currently available theoretical predictions for the ratio of the dijet cross section at large $\Delta\eta$ at $\sqrt{s} = 1800$ and 630 GeV are summarized in Table 24.

Theory	$R = \sigma_{1800}/\sigma_{630}$
asymptotic LO QCD	1.0
exact LO QCD	1.2
HERWIG	1.6
LLA BFKL	1.9

Table 24: *Theoretical predictions for the ratio of the dijet cross sections, for $\Delta\eta > 2$, at $\sqrt{s} = 1800$ and 630 GeV.*

We measured the ratio of the dijet cross section for $\Delta\eta > 2$ at $\sqrt{s} = 1800$ and 630 GeV to be equal to:

$$R = 2.8 \pm 0.3\,(\text{stat}) \pm 0.3\,(\text{syst}) = 2.8 \pm 0.4\,.$$

In the framework of the BFKL equation, in the LLA approximation (i.e., fitting the data to eq. (17)), we extracted an effective value for the BFKL intercept equal to:

$$\alpha_{\text{BFKL}} = 1.65 \pm 0.05\,(\text{stat}) \pm 0.05\,(\text{syst}) = 1.65 \pm 0.07\,.$$

Our result is four standard deviations higher than the LO QCD prediction, and three standard deviations higher than the HERWIG prediction. The data show a strong rise of the dijet cross with the rapidity interval, qualitatively consistent with BFKL evolution.

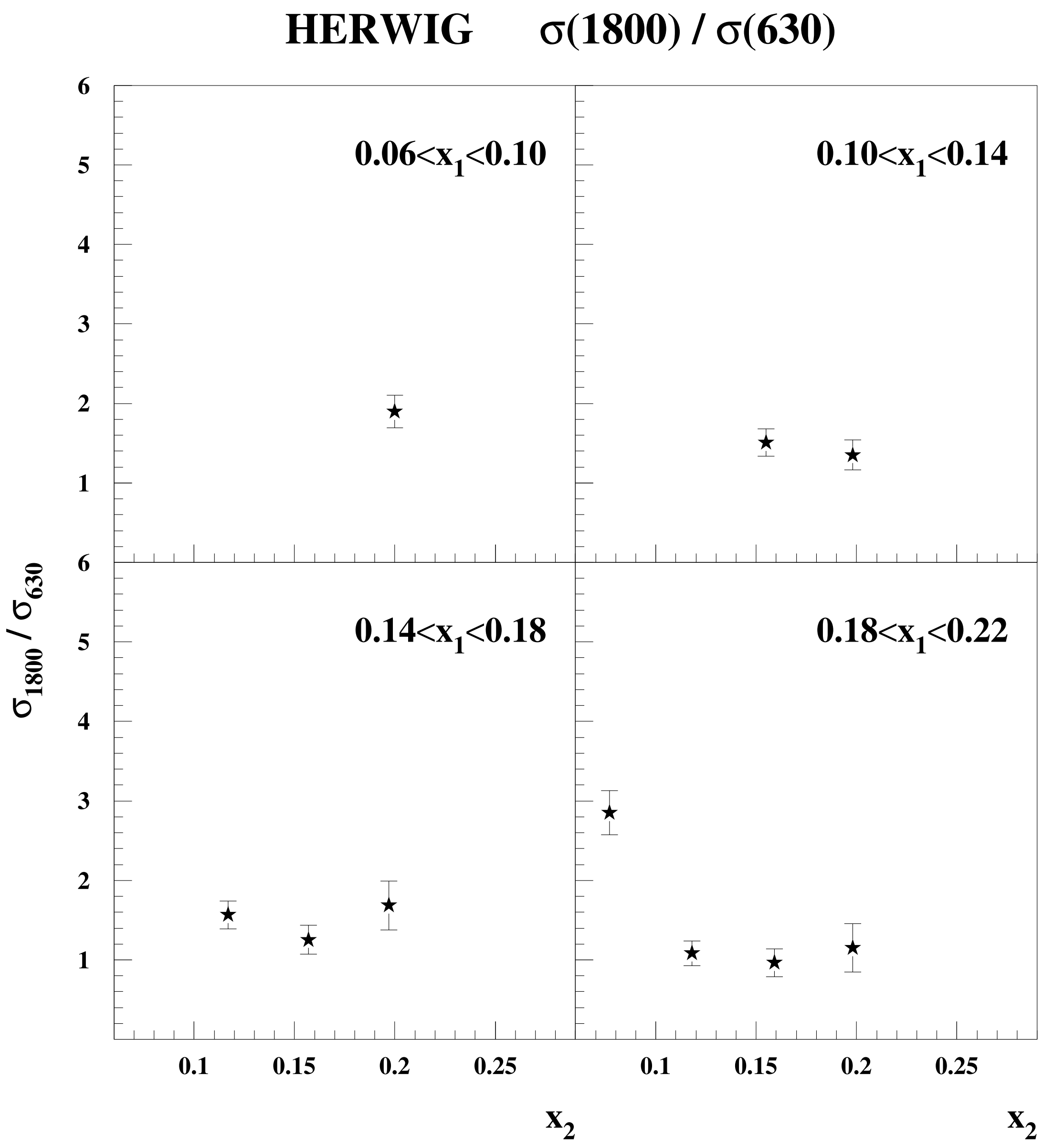

Figure 41: The ratio of the dijet cross section at $\sqrt{s} = 1800$ and 630 GeV in HERWIG. The error bars represent statistical uncertainties.

9 Conclusions

We measured the inclusive dijet cross section at large rapidity separations, $\Delta\eta$, between the jets in $p\bar{p}$ collisions at $\sqrt{s} = 1800$ and 630 GeV. The ratio of the dijet cross section at the two center-of-mass energies, for fixed jet longitudinal momentum fractions, x, and momentum transfers, Q, is in first order equal to the ratio of the partonic dijet cross section at two different rapidity intervals. The data show a strong rise of the partonic dijet cross section with $\Delta\eta$, qualitatively consistent with BFKL evolution.

A Jet Energy Resolutions

We have measured the jet E_T resolutions from the $\sqrt{s} = 1800$ GeV data corrected with CAFIX 5.2, using the dijet asymmetry method (for a detailed description of the method see ref. [27]). We bin the data in five rapidity regions, and select same–side dijets. The results are shown in Fig. 42. The dashed lines in the plots represent the fitting and systematic errors added in quadrature.

Limited statistics prohibits the extraction of the jet resolutions at $\sqrt{s} = 630$ GeV at forward rapidities. Therefore, we compare the resolutions at the two energies in extended rapidity regions, $|\eta| < 0.8$ and $0.8 < |\eta| < 2$, for same–side dijets [28]. In the η and E_T regions where the measurement of the resolutions is possible at both c.m. energies, the 630 GeV resolutions are smaller than the 1800 GeV ones by $\sim$1. We use the 1800 GeV resolutions to unsmear both the 1800 and 630 GeV cross sections. The difference between the resolutions at the two c.m. energies is accounted for in the systematic uncertainties of the ratio and the intercept (see sections 7.4.2 and 7.4.6).

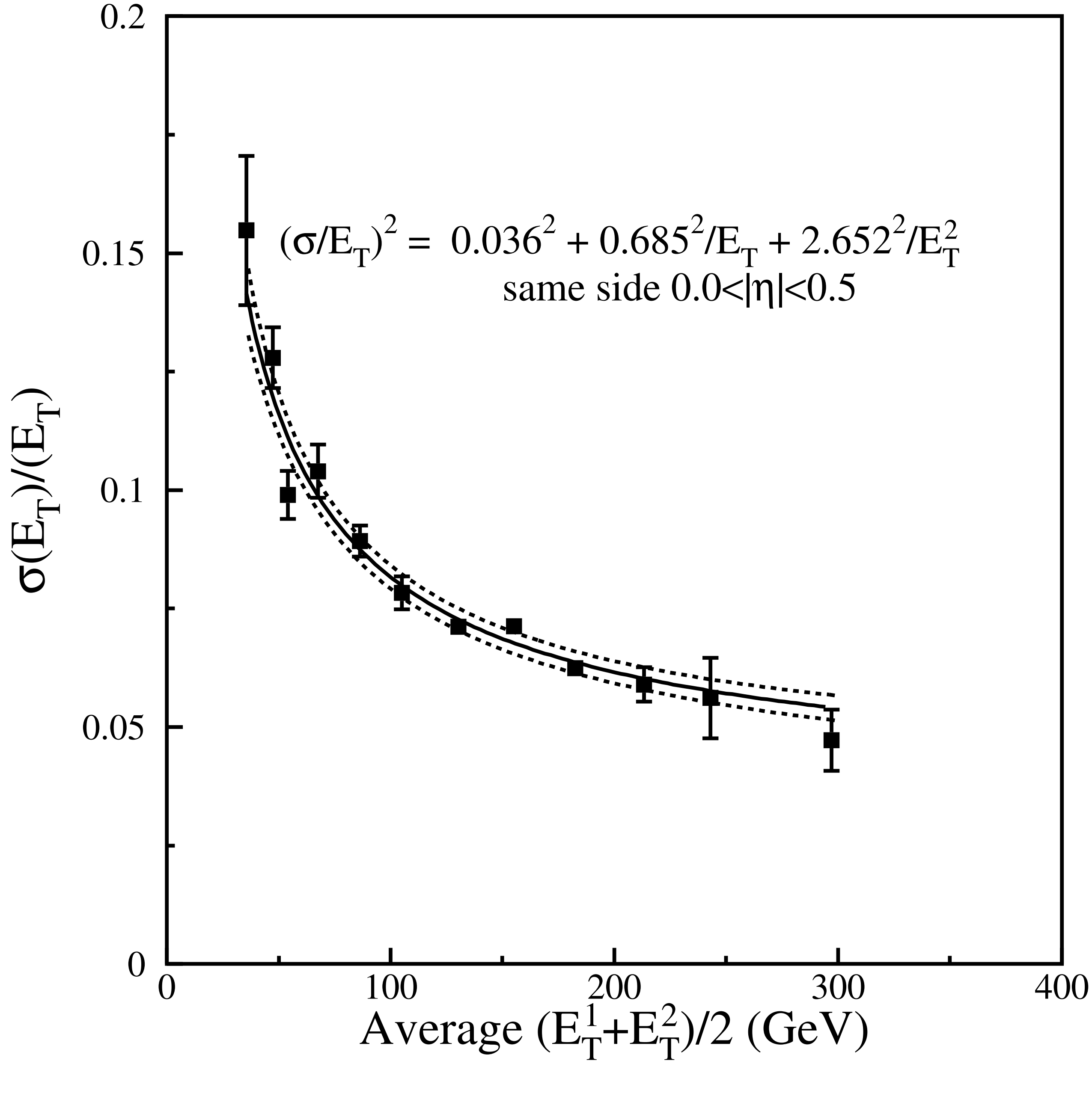

Figure 42: Jet E_T resolutions at $\sqrt{s} = 1800$ GeV (fully corrected). The dashed lines represent the fitting and systematic errors added in quadrature.

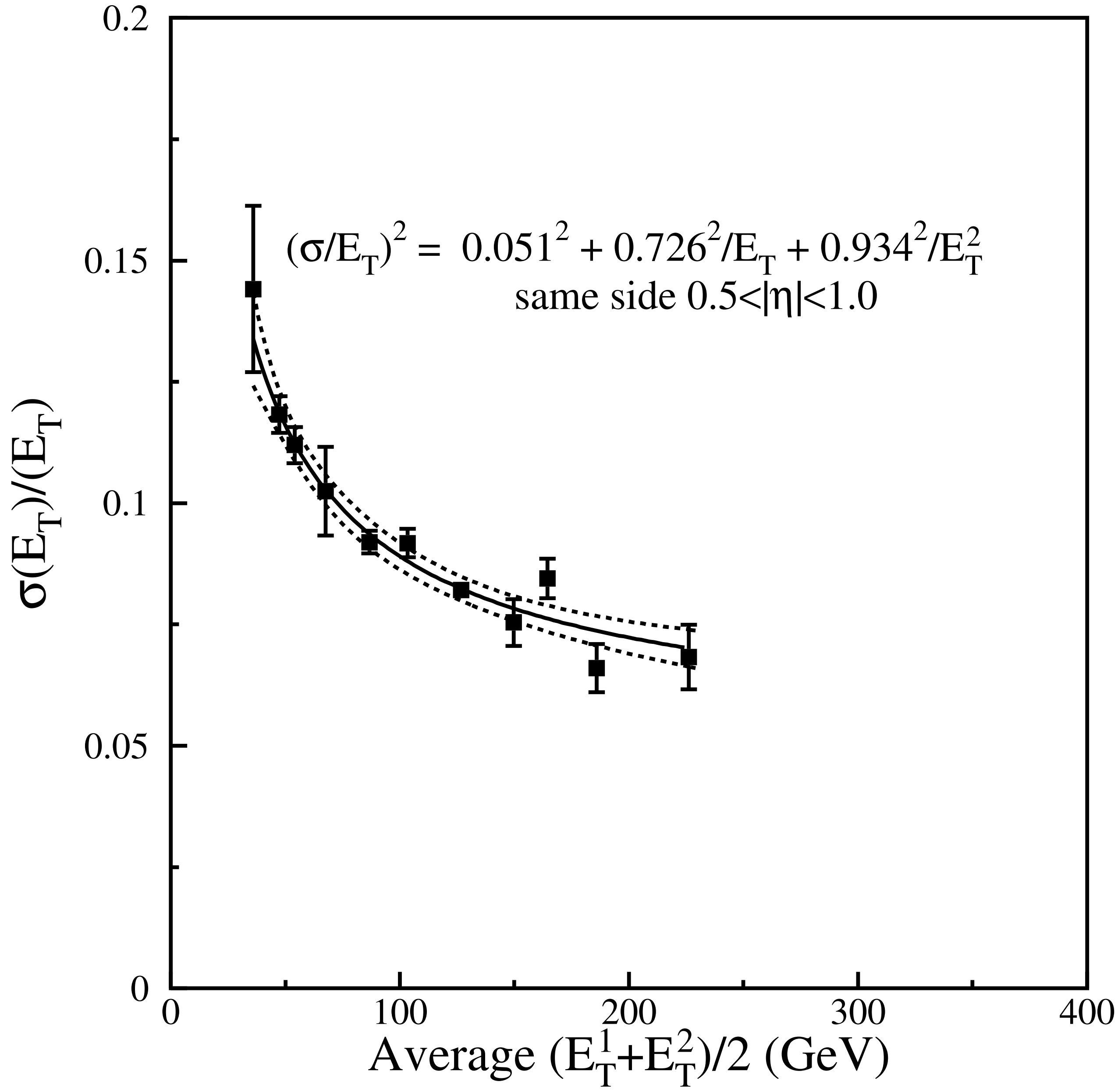

Figure 42: Jet E_T resolutions at $\sqrt{s}$ = 1800 GeV (fully corrected). The dashed lines represent the fitting and systematic errors added in quadrature.

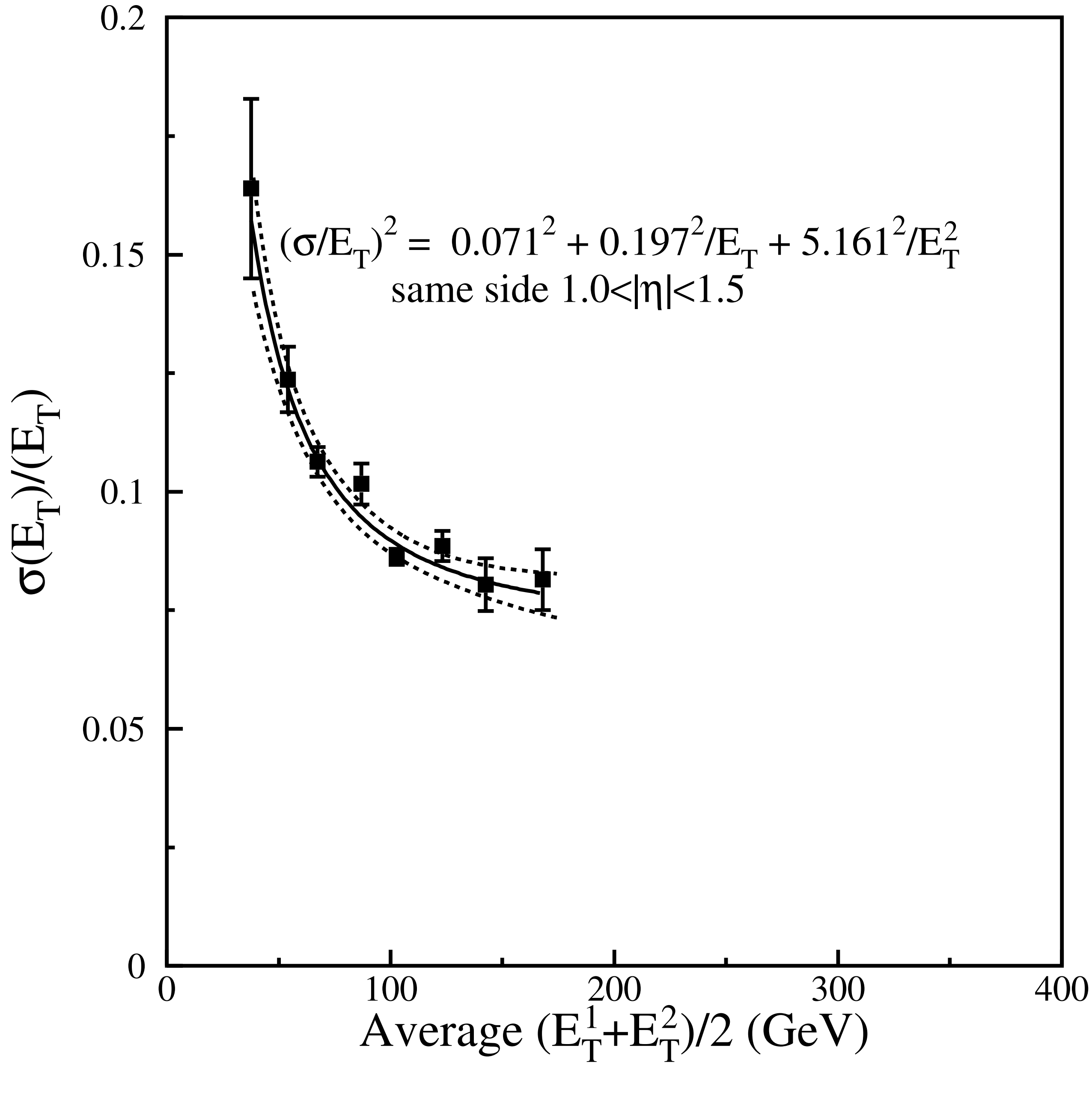

Figure 42: Jet E_T resolutions at $\sqrt{s}$ = 1800 GeV (fully corrected). The dashed lines represent the fitting and systematic errors added in quadrature.

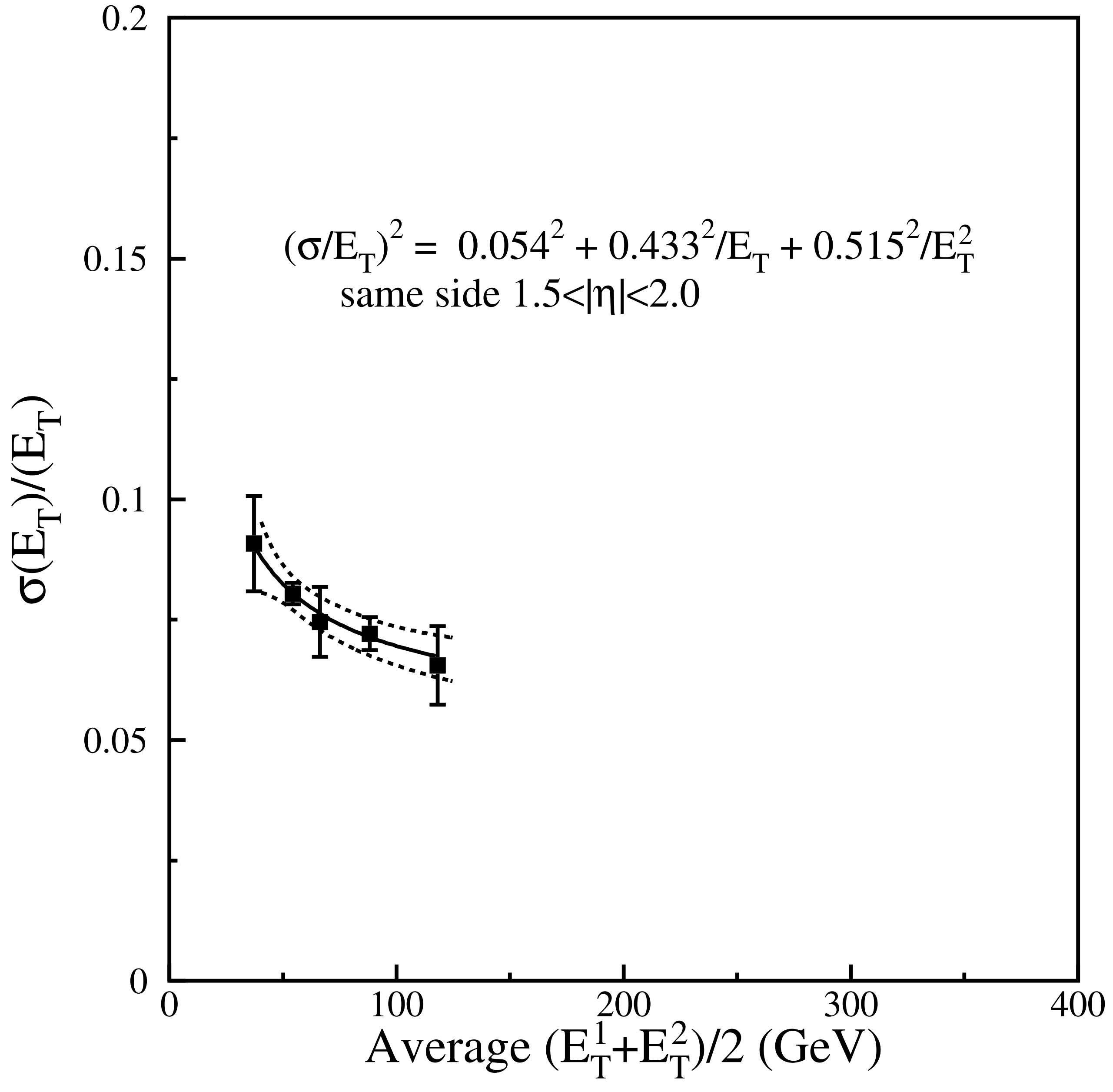

Figure 42: Jet E_T resolutions at $\sqrt{s}$ = 1800 GeV (fully corrected). The dashed lines represent the fitting and systematic errors added in quadrature.

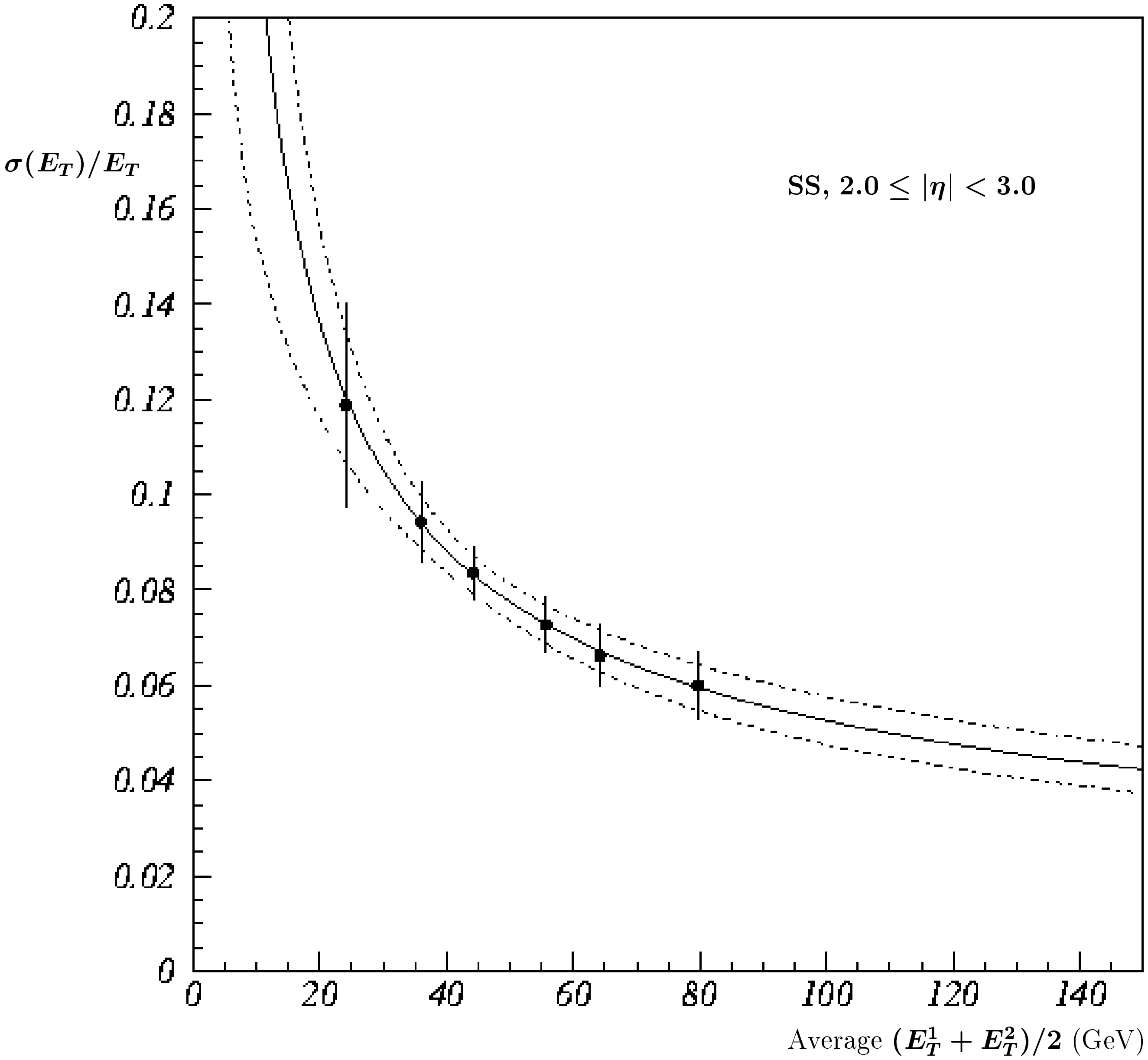

Figure 42: Jet E_T resolutions at $\sqrt{s}$ = 1800 GeV (fully corrected). The dashed lines represent the fitting and systematic errors added in quadrature.

B The Inclusive Jet Cross Section

Using the data (i.e., collected with trigger Jet 12B) and the techniques in this analysis, the inclusive jet cross section at $\sqrt{s} = 630$ GeV for $|\eta| < 0.5$ is measured. The measured cross section, before unsmearing for the effect of jet energy resolutions, is compared to the measurement in [25] (also before unsmearing). The result is shown in Fig. 43. The main difference between the two analyses is the use of the data below the trigger full–efficiency threshold (i.e., starting at 20 GeV, where the trigger efficiency is $\sim$85%) and the correction of the cross section for the trigger inefficiency (see section 5.1) in this analysis, compared to the use of the data only where the trigger is almost fully efficient in [25]. In addition, the primary vertex is selected as the vertex of the event in this analysis, compared to a minimum–H_T vertex selection in [25] (not important at low luminosities). The results of the two analyses for the central inclusive jet cross section at $\sqrt{s} = 630$ GeV are in excellent agreement. This constitutes a good systematic test for the trigger efficiencies used in this analysis (as well as in the dijet cross section measurement).

A similar test is perfomed at $\sqrt{s} = 1800$ GeV in the forward region. The inclusive jet cross section at 1800 GeV for $2 < |\eta| < 3$ is measured from the Run Ic LOWLUM data used in this analysis, and compared to the forward inclusive jet cross section from Run Ib data [29]. The two measurements are in excellent agreement (see Fig. 44). This constitutes a very good test of the Run Ic luminosity. In addition, it shows that the differences in the analyses (e.g., hot cell restoration, vertex selection, different order of applying various corrections, etc.) do not make any significant difference in the measured cross section, even in the most forward region.

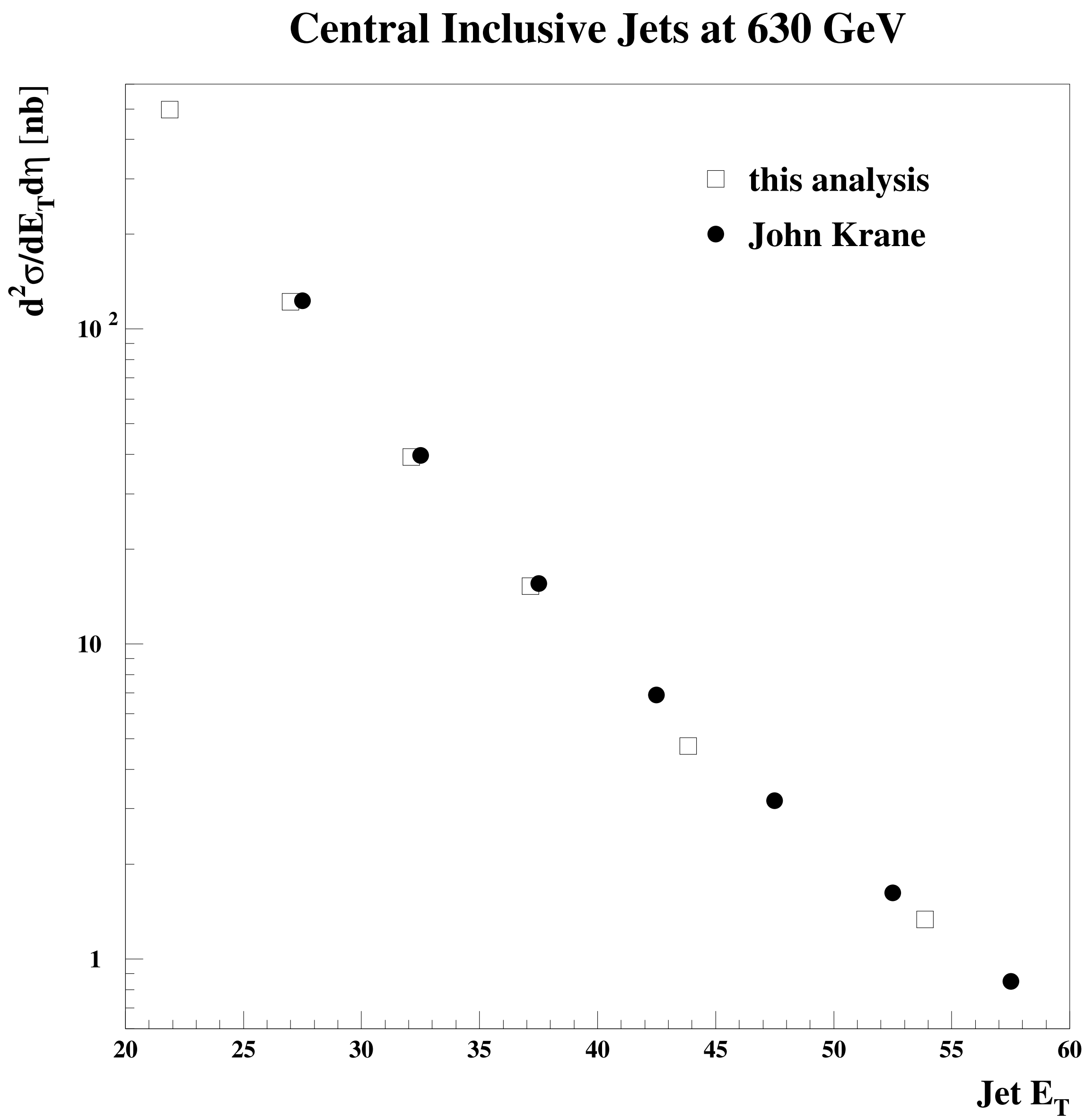

Figure 43: The inclusive jet cross section at $\sqrt{s} = 630$ GeV for $|\eta| < 0.5$.

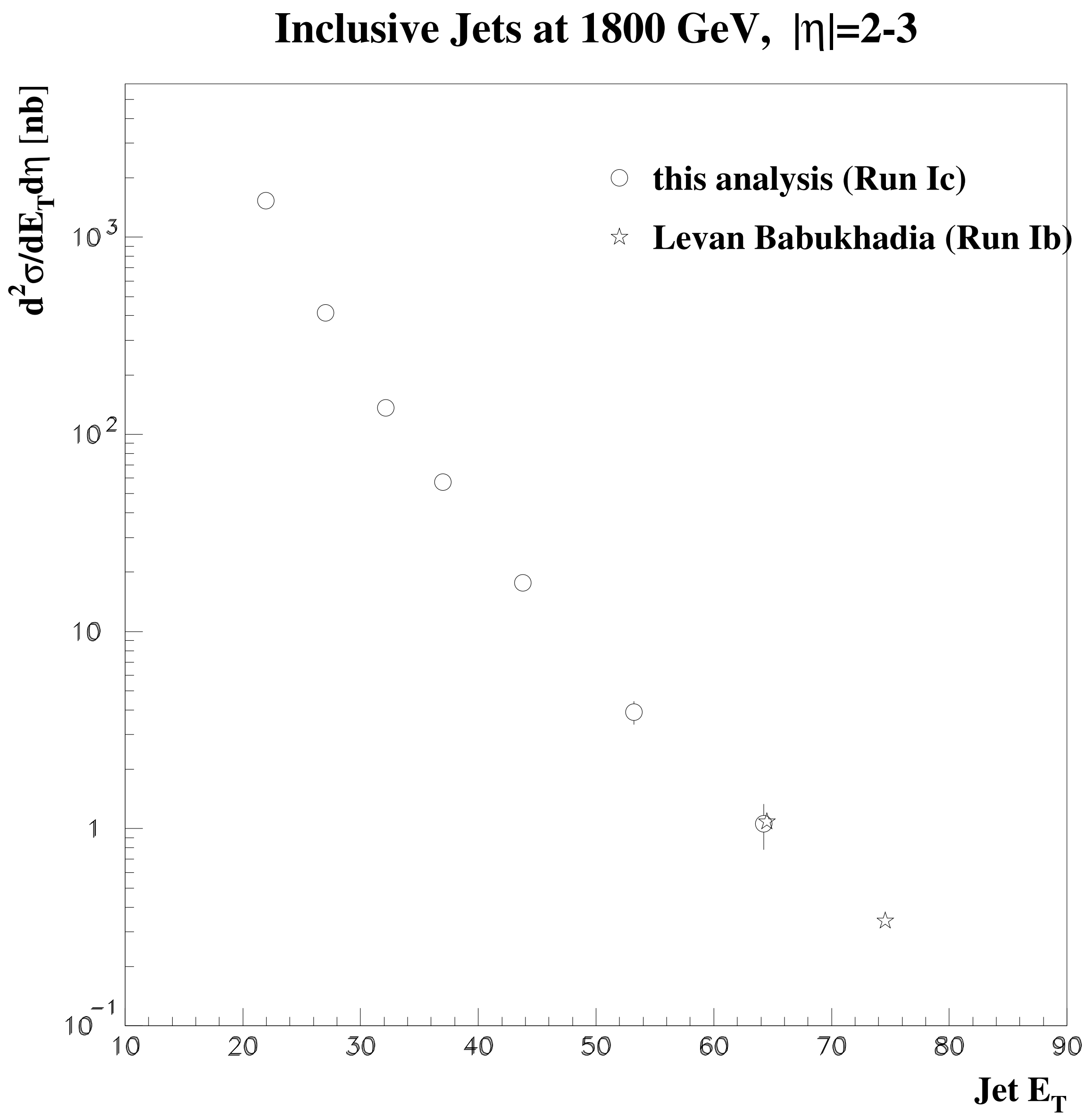

Figure 44: The inclusive jet cross section at $\sqrt{s} = 1800$ GeV for $2 < |\eta| < 3$.

References

[1] L.N. Lipatov, Sov. J. Nucl. Phys. 23 (1976) 338.
E.A. Kuraev, L.N. Lipatov, and V.S. Fadin, Sov. Phys. JETP 44 (1976) 443; Sov. Phys. JETP 45 (1977) 199.
Ya.Ya. Balitsky and L.N. Lipatov, Sov. J. Nucl. Phys. 28 (1978) 822.

[2] BFKL, NLL.

[3] V.N. Gribov and L.N. Lipatov, Sov. J. Nucl. Phys. 15 (1972) 438, 675.
L.N. Lipatov, Sov. J. Nucl. Phys. 20 (1975) 94.
G. Altarelli and G. Parisi, Nucl. Phys. B126 (1977) 298.
Yu.L. Dokshitzer, Sov. Phys. JETP 46 (1977) 641.

[4] ZEUS Collaboration, M. Derrick *et al.*, Z. f. Phys. C 72 (1996) 399.
H1 Collaboration, C. Adloff *et al.*, DESY 97-042.

[5] ZEUS Collaboration, J. Breitweg *et al.*, The European Physical Journal C6 (1999) 239.
H1 Collaboration, C. Adloff *et al.*, Nucl.Phys. B538 (1999) 3.

[6] A.H. Mueller, 'Jets at LEP and HERA', invited talk given at the 'Workshop on Jet Studies at LEP and HERA', December 10-15, 1990, Durham, England; preprint CU-TP-516.

[7] A.H. Mueller and H. Navelet, Nucl. Phys. B282 (1987) 727.

[8] A.H. Mueller, private correspondance.

[9] B. Abbott *et al.*, 'Jet Energy Scale at DØ ', DØ Note # 3287.

[10] A. Goussiou, 'New Showering Correction for the Jet Energy Scale at DØ', DØ Note # 3606.

[11] A. Goussiou and J. Krane, 'Jet Energy Scale at DØ at $\sqrt{s} = 630$ GeV', DØ Note # 3288.

[12] A. Goussiou, 'Jet Sample Selection at $\sqrt{s} = 630$ GeV', DØ Note # 3184.

[13] K. Frame, T. Geld and K. Fatyga, 'Trigger Efficiencies for Run 1B Inclusive Jet Triggers', DØ Note # 3178.

[14] N.J. Hadley, 'Cone Algorithm for Jet Finding', DØ Note # 904.

[15] R. Hirosky, 'Jet Efficiencies and Seed Tower Distributions in the DØ Cone Algorithm', DØ Note # 2405.

[16] Z.J. Casilum and R. Hirosky, 'Jet Reconstruction Efficiency', DØ # 3324.

[17] eta bias DØ notes and G. Di Loreto, thesis.

[18] DØ algo.

[19] Snowmass algo.

[20] G. Marchesini *et al.*, Comp. Phys. Comm. 67 (1992) 465.

[21] H.L. Lai *et al.*, e-print archive hep-ph/9606399.

[22] G.J. Feldman and R.D. Cousins, Physical Review D 57, (1998) 3873.

[23] S. Baker and R.D. Cousins

[24] Jet PRD.

[25] J. Krane, thesis.

[26] L.H. Orr and W.J. Stirling, Phys. Lett. B 429 (1998) 135.

[27] M. Bhattacharjee *et al.*, 'Jet Energy Resolutions', DØ Note # 2887.
I. Bertram *et al.*, 'Single Jet Resolutions at DØ for Run 1', DØ Note # 3414.

[28] A. Goussiou, 'Jet E_T Resolutions at $\sqrt{s} = 630$ GeV and Comparison to Resolutions at 1800 GeV', DØ Note # 3679.

[29] L. Babukhadia, private communication.